Quantitative Two-Layer Inversion and Customizable Sensor-Array Instrument for Electromagnetic Induction based Soil Conductivity Estimation

Achim Mester

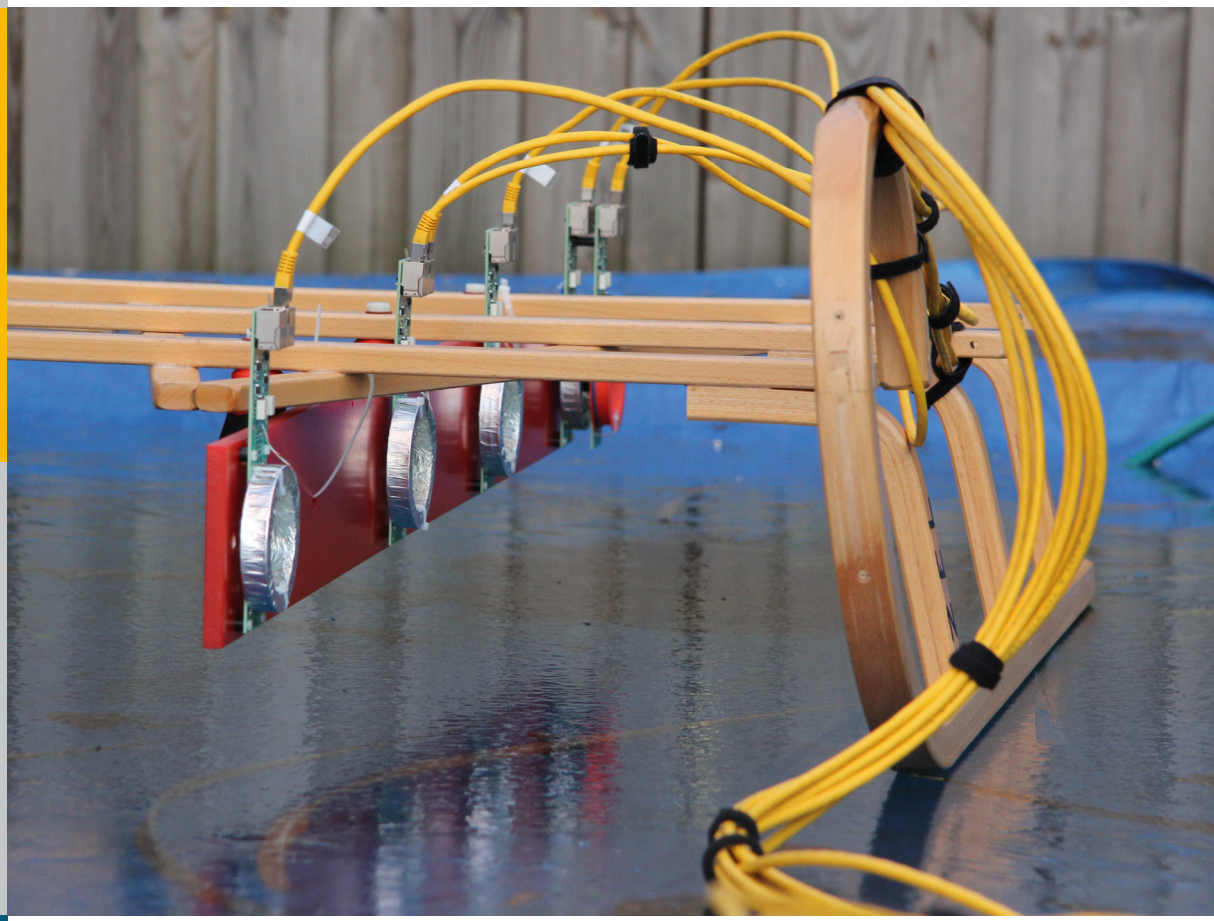

Energie & Umwelt / Energy & Environment
Band / Volume 249
ISBN 978-3-95806-035-7

JÜLICH
FORSCHUNGSZENTRUM

Schriften des Forschungszentrums Jülich
Reihe Energie & Umwelt / Energy & Environment Band / Volume 249

Forschungszentrum Jülich GmbH
Zentralinstitut für Engineering, Elektronik und Analytik (ZEA)
Systeme der Elektronik (ZEA-2)

Quantitative Two-Layer Inversion and Customizable Sensor-Array Instrument for Electromagnetic Induction based Soil Conductivity Estimation

Achim Thomas Mester

Schriften des Forschungszentrums Jülich
Reihe Energie & Umwelt / Energy & Environment Band / Volume 249

ISSN 1866-1793 ISBN 978-3-95806-035-7

Bibliographic information published by the Deutsche Nationalbibliothek.
The Deutsche Nationalbibliothek lists this publication in the Deutsche Nationalbibliografie; detailed bibliographic data are available in the Internet at http://dnb.d-nb.de.

Publisher and Distributor: Forschungszentrum Jülich GmbH
Zentralbibliothek
52425 Jülich
Tel: +49 2461 61-5368
Fax: +49 2461 61-6103
Email: zb-publikation@fz-juelich.de
www.fz-juelich.de/zb

Cover Design: Grafische Medien, Forschungszentrum Jülich GmbH

Printer: Grafische Medien, Forschungszentrum Jülich GmbH

Schriften des Forschungszentrums Jülich
Reihe Energie & Umwelt / Energy & Environment, Band / Volume 249

D 82 (Diss. RWTH Aachen University, 2014)

ISSN 1866-1793
ISBN 978-3-95806-035-7

The complete volume is freely available on the Internet on the Jülicher Open Access Server (JuSER) at www.fz-juelich.de/zb/openaccess.

Abstract

Electromagnetic (EM) measurement methods offer the great potential to non-invasively and contactlessly obtain geological and hydrological soil properties of the uppermost six meters of the subsurface with an areal resolution in the sub-meter range. The presented work is focused on small-sized frequency domain 'electromagnetic induction' (EMI) systems which combine the transmitter (Tx) and receiver (Rx) unit in one portable construction and obtain the apparent electrical conductivity (σ_a) of the sensed soil volume by inducing electrical currents and measuring the responding electromagnetic field. The sensing depth of EMI instruments depends on the sensor configuration and in particular the coil orientation and Tx–Rx separation. In principle, multi-configuration EMI data can be inverted for the electrical conductivity distribution over depth. However, there is a demand for efficient inversion algorithms and high-quality EMI data from different sensing depths to perform such an inversion.

Here, a novel one-dimensional global-local inversion approach is implemented which evaluates the misfit between EMI data and forward modeled data for a two-layer soil using a L1-norm objective function. The global approach is based on a grid search for reasonable model parameters in combination with the local-sensitivity forward model. The two soil models with the smallest misfit are refined using the (local) simplex search algorithm with the more precise full solution electromagnetic forward model. The algorithm is analyzed using synthetic EMI data. Applying the inversion on quantitative EMI transect data from two commercial devices with eight different sensor configurations results in a two-layer electrical conductivity model with lateral and vertical conductivity changes that are in good agreement with a collocated electrical resistivity tomography data set.

To improve the depth-resolution beyond available fixed configurations, a novel EMI prototype system (ElMa1) with customizable sensor-array is developed, containing multiple modular sensor units which can be flexibly arranged by the operator for each survey, ensuring optimal depth-sensitivity (i.e. coil orientations and Tx–Rx separations) for the specific investigation. The sensor units consist of coil-based transmitter and receiver circuits which allow for the measurement of the magnetic flux and the sensor impedance in a frequency range between 3 and 33 kHz, respectively. To allow for flexible sensor configurations, data processing and signal optimization, the transmitter current and the receiver voltages are separately digitized using 24-bit analog-to-digital converters (ADC's) which provide a high dynamic range and phase stability. For a measurement time of 0.5 s, the ElMa1 system achieves an instrumental σ_a-accuracy of 1 mS/m at 20 kHz for the intended Tx–Rx separation of 1.0 m and an accuracy of 10 mS/m for a less favorable configuration with smaller Tx–Rx separation of 0.3 m and smaller measurement frequency of 5 kHz, both observed under stable temperature conditions. In addition, experimental data were corrected for temperature-induced system drifts by simulating the electrical circuit of the sensor system using spectral measurements

of the coil impedances. For a temperature change of about 15 K, a drift correction accuracy of better than 30 mS/m is achieved for a Tx–Rx separation of 0.3 m.

In addition, an improved prototype system for field surveys (ElMa2) is developed which is powered by batteries, weighs about 10 kg, and fits into a backpack. Instead of the desktop personal computer (PC), which is included in ElMa1, a laptop PC is used for controlling the ElMa2 system and storing the data. The corresponding, PXI bus synchronized, ADC boards are replaced by appropriate USB units with similar digitalization characteristics. Besides the optimization for size, weight and power supply, the system provides nine sensor channels and improved sensor units. The instrumental σ_a-accuracy of ElMa2 is better than 1 mS/m for Tx–Rx separations between 0.6 and 1.6 m using a measurement time of 0.5 s. First experimental results show that the system is capable of collecting apparent conductivity data, providing a similar data quality after applying the two-layer inversion compared to a collocated EMI data set from a commercial system.

The developed EMI system with customizable sensor-array in combination with the two-layer inversion enables detailed subsurface electrical conductivity characterizations on the field-scale for a wide range of applications.

Zusammenfassung

Elektromagnetische Messmethoden haben das Potential auf nicht-invasive und kontaktlose Weise geologische und hydrogeologische Bodeneigenschaften der oberen sechs Meter des Bodens mit einer Flächenauflösung im Submeterbereich zu bestimmen. Die vorliegende Arbeit bezieht sich auf kompakte 'elektromagnetische Induktionsmesssysteme' (EMI-Systeme), die mittels zeitharmonischer Signale messen und sowohl den Sender (Tx) als auch den Empfänger (Rx) in einem einzigen tragbaren Gerät vereinen. Solche Systeme bestimmen die scheinbare elektrische Leitfähigkeit (σ_a) des Bodens, indem in diesem ein elektrischer Strom induziert wird und das davon erzeugte, sekundäre, Magnetfeld gemessen wird. Die Messtiefe von EMI-Systemen hängt von der Sensorkonfiguration und insbesondere von der Spulenausrichtung sowie dem Tx–Rx-Abstand ab. Grundsätzlich können Messdaten von mehreren Sensorkonfigurationen invertiert werden, um die Leitfähigkeitsverteilung über die Tiefe zu bestimmen, wobei effiziente Inversionsalgorithmen und quantitative EMI-Daten mit unterschiedlichen Tiefeninformation für eine solche Datenverarbeitung benötigt werden.

Im Rahmen dieser Arbeit wurde ein zweischrittiger 1D-Inversionsansatz entwickelt, der die Übereinstimmung der Messdaten mit einem Zwei-Schicht-Bodenmodell mittels L1-Norm bewertet. Dazu wird im ersten Schritt eine auf sinnvollen Bodenmodellen beruhende Rastersuche in Kombination mit der 'local sensitivity'-Vorwärtsrechnung verwendet. Die zwei Modelle mit der größten Übereinstimmung werden mit einem Simplex-Algorithmus und dem genaueren elektromagnetischen Vorwärtsmodell optimiert. Der Inversionsalgorithmus wurde mit synthetischen Daten analysiert. Die Anwendung der Inversion auf quantitative EMI-Profildaten, welche mittels zweier kommerzieller Geräte in acht verschiedenen Konfigurationen gemessen wurden, resultiert in Zwei-Schicht-Leitfähigkeitsmodellen mit lateralen und vertikalen Leitfähigkeitsänderungen, welche gut mit einem Referenzdatensatz, der mittels elektrischer Widerstandstomographie am gleichen Ort gemessen wurde, übereinstimmen.

Um die Tiefenauflösung über die erhältlichen festen Gerätekonfigurationen hinaus zu verbessen, wurde ein neuartiger mehrkanaliger EMI-Prototyp (ElMa1) mit anpassbarer Sensorkonfiguration entwickelt, der modulare Sensoreinheiten beinhaltet welche flexible vom Anwender für jede Messung und speziell für die gewünschte Tiefenauflösung einer Kampagne zusammengestellt werden können, so dass eine optimale Konfiguration verwendet werden kann. Die Sensoreinheiten bestehen aus spulenbasierten Sende- und Empfangsschaltungen, die für die Messung des magnetischen Flusses sowie der Spulenimpedanz in einem Frequenzbereich zwischen 3 und 33 kHz optimiert sind. Um die flexiblen Sensorkonfigurationen zu ermöglichen, werden der Strom durch den Sender und die Spannung am Empfänger separat mittels 24-bit Analog/Digital (A/D) Umsetzer erfasst, welche ein großer Dynamikumfang und eine hohe Phasenstabilität auszeichnet. Für eine Messzeit von 0,5 s erreicht das System eine instrumentelle σ_a-Genauigkeit von 1 mS/m bei 20 kHz für den angestrebten Tx–Rx-Abstand von

1,0 m und eine Genauigkeit von 10 mS/m für eine ungünstigere Konfiguration mit kleinerem Tx–Rx-Abstand von 0,3 m und einer kleineren Messfrequenz von 5 kHz, jeweils bei temperaturstabilen Bedingungen. Zusätzlich wurden Messdaten mittels Simulation der elektrischen Sensorschaltungen, welche hauptsächlich auf der spektralen Messungen der Spulenimpedanzen basiert, hinsichtlich temperaturbedingter Driften des Systems korrigiert. Für eine Temperaturänderung von 15 K wurde eine Genauigkeit der Korrektur von besser als 30 mS/m für einen Tx–Rx-Abstand von 0,3 m erreicht.

Desweiteren wurde ein verbesserter Prototyp für Feldmessungen (ElMa2) entwickelt, welcher batteriebetrieben ist, etwa 10 kg wiegt und in einen Rucksack passt. Anstatt des Desktop-Computers im ElMa1-System wird bei ElMa2 ein Laptop zur Steuerung und Datenspeicherung verwendet. Die dazugehörigen, PXI-bus synchronisierten, A/D-Steckkarten wurden durch vergleichbare USB-Geräte ersetzt. Neben der Optimierung der Größe, des Gewichts und der Stromzufuhr beinhaltet das System neun Sensorkanäle und verbesserte Sensoreinheiten. Die instrumentelle σ_{a}-Genaugikeit von ElMa2 ist besser als 1 mS/m für Tx–Rx-Abstände von 0,6 bis 1,6 m und eine Messzeit von 0,5 s. Erste Ergebnisse von einem Messprofil, welches mit neun Sensoren, die an einer Schlittenkonstruktion befestigt wurden und mittels individueller Kabel an das Messsystem angeschlossen wurden, zeigen, dass das System σ_{a}-Daten messen kann und eine vergleichbare Genauigkeit der invertierten Zwei-Schicht-Modelle erreicht, wie solche, die mittels eines kommerziellen EMI-Gerätes auf dem gleichen Profil gemessen wurden.

Das entwickelte Mehrkanal-EMI-System mit anpassbarer Sensoranordnung ermöglicht in Kombination mit der Zwei-Schicht-Inversion die detaillierte Charakterisierung des Untergrundes auf der Feldskala für eine Vielzahl von Anwendungsgebieten.

Publications

Parts of this doctoral thesis have been published or will be extracted and extended for future publications. The following list gives an overview of the written publications during my doctoral studies.

Mester, A., J. van der Kruk, E. Zimmermann and H. Vereecken. 2011. Quantitative two-layer conductivity inversion of multi-configuration electromagnetic induction measurements. *Vadose Zone Journal* **10**(4). 1319–1330. doi:10.2136/vzj2011.0035.

Mester, A., E. Zimmermann, J. van der Kruk, W. Glaas, J. Berwix and B. Wolters. 2012. Elektromagnetisches Leitfähigkeitsmesssystem mit verbesserter Driftkorrektur. *German patent application*. 102012008194.4. PT 1.25632012.

Mester, A., E. Zimmermann, J. van der Kruk, H. Vereecken and S. van Waasen. 2014. Development and drift-analysis of a modular electromagnetic induction system for shallow ground conductivity measurement. *Measurement Science and Technology* **25**. 055801 (13pp). doi:10.1088/0957-0233/25/5/055801.

von Hebel, C., S. Rudolph, A. Mester, J. A. Huisman, P. Kumbhar, H. Vereecken and J. van der Kruk. 2014. Three-dimensional imaging of subsurface structural patterns using quantitative large-scale multi-configuration electromagnetic induction data. *Water Resources Research* **50**. 2732–2748. doi:10.1002/2013WR014864.

Mester, A., E. Zimmermann, C. von Hebel, J. van der Kruk, H. Vereecken and S. van Waasen. Field-optimization and validation of a novel multi-channel electromagnetic induction system. *In preparation.*

Contents

1. Introduction[1]

1.1. Background and Motivation

Water is one of the most important resources for life on earth. Its sustainable use is necessary for ensuring the quality of living as well as the agricultural and industrial production. As a consequence of the increasing world population and the associated extensive land use for urbanization, food production, industry, infrastructure, waste sites etc. it is important to understand the transport processes of the hydrological cycle in the earth and, in particular, to ensure that pollutants do not contaminate reservoirs and no more water is taken out from reservoirs than is restored on a regular basis (Tezkan 1999; Rubin and Hubbard 2005; Triantafilis and Monteiro Santos 2011). The soil layer that controls much of the water flow and the agronomic processes, is the vadose zone, which is also most vulnerable for contamination (Rubin and Hubbard 2005). The transport processes vary depending on the thickness of the vadose zone, its hydraulic permeability, porosity and other soil properties that need to be mapped continuously on different spatial and temporal scales to study its relevance for the hydrological cycle. For example, it is necessary to optimize the agricultural production while minimizing the environmental damage, e.g. due to fertilizers, which get into the food chain, or salinization of the drainage water (Rhoades 1993).

In earlier times of geophysical prospection, elaborate monitoring setups, which needed to be calibrated by soil samples, were installed at multiple locations to characterize the subsurface, e.g. on a field site (Nielsen et al. 1973). Obviously, such a survey is laborious and it is critical to choose representative locations for the measurement points in order to transfer the observation data from the point-scale to the larger scales (e.g. Lesch et al. 1995). In addition, it is generally favored to minimize the soil invasion for environmental and economic reasons.

[1] partly adapted from Mester et al. (2011) and Mester et al. (2014).

Recent advances in geophysical and georeferencing (e.g. GPS) techniques enable the efficient investigation of the soil electrical conductivity (σ) on various spatial and temporal scales. The electrical conductivity is related to soil properties like water content, salinity, clay or mineral content, porosity and temperature (Archie 1942; Revil et al. 1998). For example, the electrical conductivity can be measured using electrical resistivity tomography (ERT) in the lower frequency range ($\lesssim$ 50 Hz), electromagnetic (EM) methods in the intermediate range (100 Hz – 200 kHz) and ground penetrating radar (GPR) for frequencies higher than 10 MHz.

Through utilizing the principle of inductive coupling, EM methods are rather versatile and robust in its application compared to other established geophysical methods such as GPR and ERT, since typical soil conductivities do not influence the investigation depth and no galvanic contact to the soil needs to be established, respectively. Furthermore, the contactless nature of the inductive coupling enables a fast measurement progress. During the last decades, EM methods have proven their value in near-surface applications by enabling point and transect measurements of the apparent electrical conductivity (σ_a) as well as its mapping on small plots ($\sim$100 m^2), fields (100–50000 m^2) and whole basins (2500–25000 km^2) (Robinson et al. 2008).

Electromagnetic methods include frequency domain electromagnetic (FEM) and time domain or transient electromagnetic (TEM) methods. Depending on the used device and the specific application, the common name of the method varies. For example, large-scale subsurface structures can be efficiently mapped using airborne electromagnetic (AEM) systems such as fixed-wing time domain electromagnetics (FTEM), helicopter-borne frequency domain electromagnetics (HEM), or helicopter-borne time domain electromagnetics (HTEM), where the instrument is flown several meters above the ground (Auken and Christiansen 2004; Robinson et al. 2008; Siemon et al. 2009). For smaller spatial scales the instruments are towed by or mounted on all-terrain vehicles (ATV's), or carried by hand. One of the most promising methods for mapping the shallow subsurface on the field-scale is electromagnetic induction (EMI).

Electromagnetic induction has proven to be a powerful tool to map the apparent conductivity of the vadose zone for a wide range of applications including engineering, environmental, and agricultural sciences (Pellerin and Wannamaker 2005; Robinson et al. 2008). These apparent conductivity maps can indicate changes in salinity (Rhoades 1993; Urdanoz et al. 2008), clay

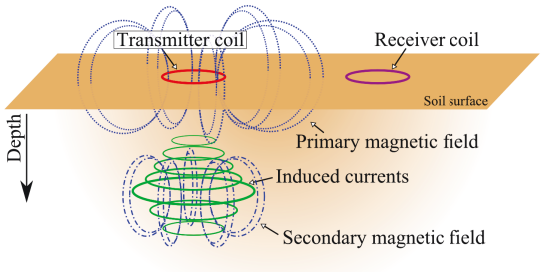

Figure 1.1.: Basic EMI setup, where the transmitter current generates a primary magnetic field which causes induced currents in the conductive soil such that a secondary magnetic field is created. The superposition of both field components is measured by a receiver coil.

content (Triantafilis and Lesch 2005) or soil water content (Kachanoski et al. 1988; Reedy and Scanlon 2003; Sherlock and McDonnell 2003; Abdu et al. 2008; Lück et al. 2009). Thereby, EMI allows to resolve in-field heterogeneities, providing information that can be used for ideal soil and crop treatment (Corwin and Lesch 2003; Corwin and Lesch 2005).

1.2. Concept of Electromagnetic Induction

When an EM field penetrates a lossy medium, it is influenced by the electrical conductivity (σ), the electrical permittivity (ε), and the magnetic permeability (μ) of the latter, which can be described by the complex (*) value $\gamma^* = \sqrt{i\mu\sigma\omega - \varepsilon\mu\omega^2}$, using the angular frequency (ω) and the imaginary unit (i) (Keller 1988). Depending on the frequency of the transmitted magnetic field, either the electrical conductivity or the electrical permittivity dominates the response behavior. For the geophysical methods that are referred to as EMI methods, the measurement frequencies (f) are sufficient low ($< 10^5$ Hz) and the electrical conductivities of the materials of investigation are large enough such that approximations for the quasi-static field domain are valid, where the electrical permittivity can be neglected ($\sigma \gg \omega\varepsilon$) (e.g. Ward and Hohmann 1988, p. 136). The principle of a frequency domain EMI measurement is shown in figure 1.1: A time-varying current flows through a transmitter (Tx) coil (red loop) and, according to Ampere's law, generates a time-varying primary magnetic field which diffuses into the earth (blue dotted curves). Due to the phenomenon of electromagnetic induction, which is described by Faraday's law, the changing magnetic field induces electrical voltages in the subsurface such that electrical currents (green loops) are created, where the

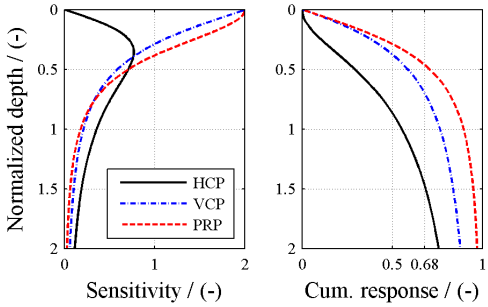

Figure 1.2.: The left plot shows the local-sensitivity curves as described by McNeill (1980) for three coil orientations: Horizontal coplanar loops (HCP), vertical coplanar loops (VCP) and perpendicular loops (PRP). The right plot shows the corresponding cumulative response curve, which is the integrated sensitivity down to the indicated depth. Note that the given depth is normalized on the Tx–Rx separation (s).

magnitudes depend on the electrical conductivity of the soil. These currents generate a secondary magnetic field (blue dash-dotted curves), which is several orders of magnitude smaller than the primary magnetic field. Both field components superimpose and are measured by a receiver (Rx) coil at the surface (purple loop).

For frequency domain EMI data, the processing is based on the linear relationship between the imaginary part of the quotient of the secondary and the primary magnetic field, and the electrical conductivity of a half-space directly below the EMI system as described by McNeill (1980). The resulting apparent conductivity value equals the true soil electrical conductivity if it is measured above a homogeneously conductive soil. Otherwise, it provides qualitative information about lateral conductivity changes and, when measuring with multiple (different) coil configurations, can give information about its variation over the depth. The sensing depth of EMI depends on the coil orientation (o), the Tx–Rx separation (s), and the measurement frequency. For example, approximately 68 % of the soil response is depending on the electrical conductivity of the uppermost $1.50 \times s$ meter of the soil for horizontal coplanar (HCP) loop configurations, $0.75 \times s$ meter for vertical coplanar loops (VCP), and $0.50 \times s$ for perpendicular (PRP) loop setups (McNeill 1980). The corresponding local sensitivity and cumulative response curves are shown in figure 1.2. In addition, the investigation depth can be altered by changing the instrument height above the ground (Triantafilis and Monteiro Santos 2010).

From a technical point of view, measuring the soil response which is superimposed by the transmitter signal is a challenge for the data acquisition (DAQ), either in terms of dynamic range or regarding signal compensation approaches. Time domain or transient electromagnetic methods circumvent this problem by switching off the transmitter signal before measuring the soil response. However, switching the transmitter off accurately and fast is also a technical challenge such that common time domain methods are usually not suitable for environmental investigations of the uppermost five meters of the subsurface (Hoekstra et al. 1992).

1.3. Measurement Systems

The EMI instruments which are investigated within this thesis belong to the group of small-sized frequency domain EMI devices that combine the Tx and Rx units in one portable construction and are optimized for mapping the shallow near-surface (0 - 6 m) on the field-scale. Several instruments of this category are commercially available, offering coil orientations with HCP, VCP and PRP, Tx–Rx separations between 0.3 m and 4.0 m, and time-harmonic excitation signals in the frequency range between 5 and 30 kHz.

The increasing interest in measuring the soil electrical conductivity variation over depth has resulted in the development of new multi-configuration EMI instruments which measure multiple apparent conductivities simultaneously. For example, the widespread EM38 (Geonics Limited; Mississauga, ON; Canada) with 1-m Tx–Rx separation is now available with an additional receiver at $s = 0.5$ m, and most new EMI systems contain multiple sensors like the CMD-MiniExplorer (GF Instruments, s.r.o.; Brno; Czech Republic) with three receivers, or the DUALEM-421S (Dualem Inc.; Milton, ON, Canada) with six receiver configurations. Using an increased number of different Tx–Rx configurations results in a higher information density about the conductivity changes over depth. However, a field campaign is often focused on a specific depth region which should be resolved as good as possible. At the moment, all available EMI devices of the considered category provide fixed configurations, and are therefore optimized for certain depth ranges such that they are not flexible for different applications. However, there is a demand for more flexible instruments which enable adjusting the instrument configurations for specific investigations (Bonsall et al. 2013).

1.4. Inversion

Multi-configuration EMI data enable a joint inversion which results in quantitative electrical conductivity values over depth (Monteiro Santos 2004; Mester et al. 2011; Monteiro Santos et al. 2011; Triantafilis and Monteiro Santos 2011; von Hebel et al. 2014) with its vertical resolution depending on the number and diversity of the used coil configurations (Guérin et al. 1996).

Monteiro Santos (2004) introduced a smooth and laterally constrained inversion algorithm based on the local-sensitivity forward model (LS model) from McNeill (1980) and observed smooth conductivity-over-depth profiles for the uppermost 40 meters of the soil using Tx–Rx separations of 10, 20 and 40 m, each measured in HCP and VCP orientation. Saey et al. (2009) detected the depth-to-clay interface using data from HCP, VCP and PRP orientations in combination with Tx–Rx separations of 1 and 2 m. Recently, Monteiro Santos et al. (2010b) jointly inverted synthetic and experimental EMI data from different Tx–Rx separations and coil orientations based on a one-dimensional (1D) laterally constrained inversion algorithm using the LS model. In this inversion, a Tikhonov regularization was included and a regularization factor was determined using the L-curve. The general shape of the synthetic models was reasonably well reconstructed, but due to the smoothed inversion the boundaries between the layers were smeared out.

Most inversion approaches are based on the approximate LS model, whereas Hendrickx et al. (2002) showed that full solution electromagnetic forward models (EM models), which are based on the exact calculation of the electromagnetic diffusion in a horizontally layered medium, are more accurate for high-conductivity regions, where the induction number (β) is larger (compare Monteiro Santos et al. 2010a). Considering the recent increase in computational power, it becomes feasible to apply those EM models. Besides the computational expense and the available EMI configurations, the inversion of multi-configuration data requires quantitative EMI data (Lavoue et al. 2010; Mester et al. 2011).

1.5. Instrumental Challenges

In general, the calibration of measured data and devices, the correction of drift effects and other disturbing sources of errors, the sensor design, and the data acquisition are important

challenges for improving EMI systems. The following sections give insights into these topics and, in particular the latter three topics, are discussed in more detail in the main chapters of this thesis.

1.5.1. Calibration Approaches

In order to calculate the apparent conductivity, the secondary magnetic field strength (H_s^*) needs to be separated from the primary magnetic field strength (H_p^*) using a precise calibration method. In general, there are four ways of calibrating a modular EMI system with variable coil configuration. First, the system can be held up in the air (zero conductivity) at the survey site. Bosnar (2010) described a method to perform such a calibration by using multiple coil configurations. The disadvantage of this approach is that it is prone to operational errors, leading to varying results that have been observed between different surveys and for different operators (Nüsch et al. 2010). The second method is based on independent reference data from one or more locations in a survey area, to which the EMI data is fitted in the post-processing. Such a reference can be based on geophysical methods like ERT (Lavoue et al. 2010; Minsley et al. 2012; von Hebel et al. 2014). In particular, Lavoue et al. (2010) introduced a calibration method that uses ERT inverted data as input for EMI forward models to which the measured apparent conductivity values are fitted using a linear regression. Alternative sources of reference data are for example electrical conductivity probes (Saey et al. 2012) or soil samples (Moghadas et al. 2012). In general, this calibration method is reproducible and robust as long as no drift effects or disturbances occur in the EMI data and the reference data are reliable. Nevertheless, it requires additional field work and equipment. Third, a calibration can be based purely on measured electrical and geometrical properties of the measurement system by using a circuit and electromagnetic field simulation to calculate the primary field (zero conductivity data). However, it is difficult to include all environmental influences like cables and electronics in such a theoretical approach.

In contrast to those three methods, common fixed-configuration EMI systems can be calibrated using analog circuits and a calibration chart which consists of temperature dependent reference data, measured under controlled conditions and for each EMI instrument (usually by the manufacturer) (Bosnar 2006).

1.5.2. Drift Effects and other Sources of Errors

Regardless of the chosen calibration method, deviations in the measured apparent conductivity values from reference data have been observed due to temporal drifts during measurements (Sudduth et al. 2001; Simpson et al. 2009) or, more specific, due to internal warm-up effects in the EMI device (Robinson et al. 2004). Furthermore, Robinson et al. (2004) recognized apparent conductivity drifts due to a heterogeneous temperature distribution in the EMI instrument during field experiments. To sum up, the experience indicates that the influence of surrounding conditions (temperature, solar radiation, condition of power supply, system up-time, etc.) on the output of the device can be significant. Drift effects are complicated to correct since the sources are versatile and the effects are superimposed. In general, all electrical components in the system, and in particular the sensors, are subject to thermal drifts and additional components, which are included e.g. for calibration or resonant transmission (Bosnar et al. 1978; Bosnar 2006; Bosnar 2010), make the drift response more complex. One approach to account for temperature related drifts is to include analog compensation circuits. Another approach is to account for those issues using temperature-dependent calibration data, which need to be measured for each specific system. However, such a reference measurement under controlled condition is error-prone as it may not represent the conditions of every measurement environment. Note that it is common practice to check the measurements for drift effects by including reference points or survey crossings that are passed at multiple times during a survey.

Besides instrument-related issues, errors may occur due to the ambient magnetic noise level which is often frequency dependent and may change depending on the survey location and the measurement frequencies (Minsley et al. 2012).

Furthermore, a common source of errors in the measurement data is the influence of an operator or metallic objects in the vicinity of the EMI system. Therefore, EMI systems are often mounted on a sledge and pulled from further away, either by hand or with an ATV, to avoid the influence of the operator (Sudduth et al. 2001; Simpson et al. 2009; Nüsch et al. 2010; Saey et al. 2011; Minsley et al. 2012; von Hebel et al. 2014). However, if a sledge and optional equipment is attached to the system, it needs to be considered by the calibration or corrected by performing a post-calibration of the measurement data (e.g. using reference data).

1.5.3. Sensor Design

For transmitting the time-varying magnetic field, which induces the currents in the soil, an electrical coil is connected to a frequency generator. The electrical properties of the coil determine its transmission characteristics and are depending on the coil geometry, the included wire material and dimensions, and, in particular, the coil resistance (R), inductance (L) and capacitance (C). These properties also depend on the system temperature which may change during a measurement depending on the ambient temperature, the measurement duration, the transmitter power and the exposure of the system to solar radiation, and therefore may result in signal drifts. Depending on the application, the transmitter system can be optimized for narrow-band (resonant) or broad-band transmission characteristics. In general, the transmitter coil needs to be optimized for emitting power in order to provide a sufficient signal-to-noise ratio at the location of receiver system under realistic measurement conditions.

For receiving a magnetic field, several types of sensors with different sensitivity characteristics are available (Boll and Overshott 1989). Among those, anisotropic magnetoresistance (AMR) devices are not sensitive enough for the magnetic flux magnitude that needs to be measured and flux-gate sensors are too slow for the given measurement frequencies. Superconducting quantum interference devices (SQUIDs) are extremely sensitive but also to slow for EMI applications and, in addition, require cooling which is complicated during field surveys. Only electrical wire-coils can be adjusted for the required large sensitivity and are therefore typically used for the receivers. These receiver coils need to be optimized in terms of sensitivity by adjusting the coil geometry and the number of coil windings or by including ferromagnetic cores.

1.5.4. Data Acquisition

The required dynamic range (RDR) of an EMI system, which is needed to measure the secondary magnetic field strength within the primary magnetic field strength, depends on the Tx–Rx separation. It can be estimated for a specific apparent conductivity and Tx–Rx separation using the low-induction number (LIN) approximation described by McNeill (1980), resulting in RDR $= H_{\mathrm{p}}^{*}/H_{\mathrm{s}}^{*} \propto {\sigma_{\mathrm{a}}}^{-1} \cdot s^{-2}$. As a consequence, smaller Tx–Rx separations are more challenging in terms of the RDR of the used DAQ system, reaching values in the order

of 10^6 and more.

In some fixed-configuration EMI systems, the RDR is reduced by compensating the secondary magnetic field strength in the measured signal using analog circuits (e.g. Bosnar et al. 1978). However, such an approach requires a precise adjustment of these analog compensation circuits and a corresponding calibration for each coil configuration, which is sensitive for external influences like thermal drifts. Furthermore, such an approach is not applicable for flexible-configuration system which can be adjusted by the operator.

1.6. Objectives

Within the framework of this thesis, quantitative multi-configuration EMI data are analyzed for their information content with respect to a soil electrical conductivity inversion over depth and an appropriate 1D depth-inversion algorithm is implemented, optimized and applied on measured EMI transect data. Based on the results, a novel EMI prototype system is designed and set up for experimental studies. In particular, the instrument provides multiple sensor channels and flexible sensor configurations such that the vertical resolution can be optimized for the specific depth region of interest. The aim of the novel EMI system is to reach an instrumental σ_a-accuracy[2] of 1 mS/m for a Tx–Rx separation of 1 m, a measurement frequency range from 5 to 30 kHz and a measurement rate of 2 Hz. Furthermore, the calibration of the instrument and its temperature compensation is performed by digital post-processing. From the experience with this first EMI system, a second prototype is developed which is suitable for remote field applications and provides multiple modular sensor units.

1.7. Outline

In chapter 2 of this thesis, the depth information from quantitative multi-orientation, multi-offset and multi-frequency EMI data, measured with commercial EMI systems, is analyzed, and a novel 1D inversion algorithm is introduced which processes the multi-configuration data into the electrical conductivity of an upper and lower horizontal layer (σ_1, σ_2) and the corresponding thickness of the upper layer (h_1). The algorithm is based on a combined

[2] assuming that the device is used under conditions as described by McNeill (1980), where $|\mu_r| = 1$ and the instrument elevation is zero, and that the ambient magnetic noise level (B_{noise}) is 10^{-13} T/$\sqrt{\text{Hz}}$ or the equivalent of the measured induced voltage noise (U_{n}) of ≤ 30 nV.

global and local optimization scheme, resulting in optimal accuracy and computational speed: within the global optimization the misfit is estimated for a parameter grid using the fast and approximate LS model, followed by the optimization of the best results using a more flexible local optimization algorithm in combination with the accurate EM model. The inversion is tested using synthetic models, ERT inverted data, and quantitative EMI data as input.

In chapter 3, the development of the novel EMI system ElMa1 is described, which is designed for flexible sensor configurations and provides multiple channels for connecting modular sensor units. Although these units can be flexibly rearranged by the operator for each survey, the instrument is optimized for a Tx–Rx separation of 1.0 m. Besides the consideration of general system requirements for measuring geophysical EMI signals, such as sensitivity and signal-to-noise ratio, a major challenge for realizing a modular EMI device is the RDR of the used analog-to-digital converters (ADC's), which measure the secondary magnetic flux without analog compensation of the about six orders of magnitude stronger primary magnetic flux. Since the temperature-induced drift effects in such an uncompensated system are approximately linear, a model-based drift correction, based on measured electrical system parameters, is implemented and evaluated. Moreover, the error sources due to environmental and instrumental effects are analyzed and a method to select optimal measurement frequencies based on an ambient noise level analysis is presented. Note that multiple sensor channels are synchronized to the transmitter signal in the same way as the one that is exemplary analyzed in this chapter.

Chapter 4 deals with the optimization and extension of the laboratory system presented in chapter 3, regarding (1) a modular multi-sensor field setup, (2) a transmitter design with maximized magnetic moment and high-precision current measurement, and (3) a suitable size, weight and power supply for mobile surveys. First, the novel ElMa2 system is compared to ElMa1 and the improvements are explained. Then, test-setups, the field surveys and the post-processing steps are described. The prototype system is tested on a well known field-site by comparing the data to those obtained with a commercial EMI system on the same day and transect, and to previously collected ERT data.

Chapter 5 contains a final conclusion of the presented achievements and an outlook on future steps for further development of the novel measurement system.

2. Quantitative Two-Layer Conductivity Inversion of Multi-Configuration Electromagnetic Induction Measurements[1]

In this chapter, an inversion scheme is introduced which uses quantitative electromagnetic induction (EMI) data and inverts for a two-layer earth. The inversion minimizes the misfit between measured and modeled magnetic fields by a combined global and local search without the use of any smoothing parameter. Application of this new scheme to synthetic data demonstrates its efficacy in providing the required physical property information. Inverted calibrated EMI data, measured using horizontal coplanar loop and vertical coplanar loop orientations, Tx–Rx separations of 1.00 and 1.22 m, and measurement frequencies of 8 and 15 kHz, provide lateral and vertical conductivity variations very similar as observed in an elaborate electrical resistivity tomography (ERT) experiment. The inversion is verified using synthetic EMI data calculated from ERT data. Inverting quantitative EMI data using this two-layer inversion enables the quantitative mapping of lateral and vertical electrical conductivity (σ) variations over large areas.

2.1. Theory

2.1.1. Forward Models

The most commonly used forward model for inversion of EMI data is the cumulative response model or local-sensitivity forward model (LS model) described by (McNeill 1980). Due to the increased computing power, improved full solution electromagnetic forward models (EM

[1] adapted from Mester et al. (2011).

models) based on the full solution of Maxwell's equation can be used (Lavoue et al. 2010; Monteiro Santos et al. 2010a), too. Both models are used in our inversion algorithm and are briefly described in the following.

Local-Sensitivity Model

At low-induction numbers (LINs), the secondary magnetic field strength (H_s^*) measured at the receiver (Rx) can be considered as the sum of the independent magnetic fields from each individual induced current loop in the soil (McNeill 1980). Note that this approach is only valid for fairly resistive environments, which is the case for most soils, having typical conductivities between 0.1 and 100 mS/m (Rubin and Hubbard 2005, chapter 6). Here, the depth of investigation depends on the coil orientation (o) and the Tx–Rx separation (s) (Kaufman and Keller 1983, p. 163), and the contribution to the secondary magnetic field from all material up to a depth h below the sensor can be expressed by the cumulative response functions $\mathrm{CR}^{\{\mathrm{HCP,VCP}\}}$ (McNeill 1980):

$$\mathrm{CR}^{\mathrm{HCP}}(h,s) = \frac{1}{\sqrt{4\left(\frac{h}{s}\right)^2+1}}, \tag{2.1}$$

$$\mathrm{CR}^{\mathrm{VCP}}(h,s) = \sqrt{4\left(\frac{h}{s}\right)^2+1}-2\left(\frac{h}{s}\right). \tag{2.2}$$

The magnetic field response resulting from layers with electrical conductivity σ_n is then

$$\tilde{H} = \frac{|H_s^*|}{|H_p^*|} = \frac{\omega\mu_0 s^2}{4}\left(\sigma_1[\mathrm{CR}(h_0)-\mathrm{CR}(h_1)]+\cdots+\sigma_n[\mathrm{CR}(h_{n-1})-\mathrm{CR}(h_n)]\right), \tag{2.3}$$

where the quotient of the magnitudes of the secondary (H_s^*) and primary magnetic field strength's (H_p^*) is the normalized magnetic field response ($\tilde{H}$), ω is the angular frequency, and μ_0 is the magnetic vacuum permeability. Most commercial EMI systems use the LIN approximation and return an apparent electrical conductivity (σ_a) given by

$$\sigma_a = \frac{4}{\omega\mu_0 s^2}\tilde{H}. \tag{2.4}$$

Electromagnetic Full Solution Model of a Multi-layered Earth

The Maxwell-based full-solution for the magnetic field measured over a horizontally layered medium is given by (Anderson 1979; Wait 1982, pp. 122–123)

$$\tilde{H}^*_{\text{HCP, ml}} = 1 - s^3 \int_0^\infty \text{RC}^*_0 J_0(s\lambda)\lambda^2 \mathbf{d}\lambda, \tag{2.5}$$

$$\tilde{H}^*_{\text{VCP, ml}} = 1 - s^2 \int_0^\infty \text{RC}^*_0 J_1(s\lambda)\lambda \mathbf{d}\lambda, \tag{2.6}$$

where J_0, J_1 are the Bessel functions of zeroth and first order, respectively. The reflection coefficient RC^*_0 is obtained recursively beginning with $\text{RC}^*_{\text{n+1}} = 0$ and (Ward and Hohmann 1988; Slob and Fokkema 2002; Lavoue et al. 2010):

$$\text{RC}^*_{\text{n}} = \frac{\frac{\Gamma^*_{\text{n}} - \Gamma^*_{\text{n+1}}}{\Gamma^*_{\text{n}} + \Gamma^*_{\text{n+1}}} + \text{RC}^*_{\text{n+1}} \cdot \exp(-2\Gamma^*_{\text{n+1}} h_{\text{n+1}})}{1 + \frac{\Gamma^*_{\text{n}} - \Gamma^*_{\text{n+1}}}{\Gamma^*_{\text{n}} + \Gamma^*_{\text{n+1}}} \cdot \text{RC}^*_{\text{n+1}} \cdot \exp(-2\Gamma^*_{\text{n+1}} h_{\text{n+1}})}, \tag{2.7}$$

using $\Gamma^*_{\text{n}} = \sqrt{\lambda^2 + \gamma^{*2}_{\text{n}}}$, the propagation constant for the n-th layer $\gamma^*_{\text{n}} = \sqrt{\omega\mu_0(i\sigma_{\text{n}} - \omega\varepsilon_0)}$ with the corresponding electrical conductivity of the n-th layer (σ_{n}). Evaluating these numerical integrals is complicated due to the oscillating nature of the Bessel functions and the corresponding slow convergence.

Analytical Expression for a Homogeneous Halfspace

The integral in (2.5) and (2.6) converges faster when the oscillating nature of the integrand is reduced by including the analytical expression for the homogeneous half-space. For a multi-layer model with a relatively large upper layer the expression for a homogeneous half-space is subtracted from the integrand in equation 2.5 and 2.6, and the analytical expression given by (Wait 1982),

$$\tilde{H}^*_{\text{HCP}}(s, \gamma^*) = \frac{2}{\gamma^{*2} s^2}\left[9 - e^{-\gamma^* s}(9 + 9\gamma^* s + 4\gamma^{*2} s^2 + \gamma^{*3} s^3)\right], \tag{2.8}$$

$$\tilde{H}^*_{\text{VCP}}(s, \gamma^*) = -\frac{2}{\gamma^{*2} s^2}\left[3 - \gamma^{*2} s^2 - e^{-\gamma^* s}(3 + 3\gamma^* s + \gamma^{*2} s^2)\right], \tag{2.9}$$

is added to compensate. This approach is valid for all induction numbers and includes imaginary and real parts of the magnetic field. However, it is not effective for thin upper layers (< 0.2 m) since the oscillating nature of the integrand is not significantly reduced, resulting in a wider integration interval and thus a longer integration time. A Gauss-Kronrod

quadrature approach, which adaptively adjusts the number of integration points (Piessens et al. 1983), is used for numerical integration of equation 2.5 - 2.7. Note that the LS model returns the imaginary part (equation 2.1 - 2.3), whereas the EM model calculates the full complex value of the normalized magnetic field response.

2.1.2. Inversion

Since EMI measurements with different coil orientations, different Tx–Rx separations and different measurement frequencies (f) contain different information about the subsurface, here, a novel inversion algorithm is introduced which combines EMI measurements in a joint inversion to reconstruct a two-layer earth. The medium parameters ($\vec{p}$), which are the electrical conductivity of the first and the second layer (σ_1, σ_2) and the thickness of the first layer (h_1) are obtained by minimizing the L1-norm data misfit ($\Delta\tilde{H}$) between the normalized measured ($\tilde{H}^{\text{mea.}}$) and modeled magnetic field ($\tilde{H}^{\text{mod.}}$):

$$\Delta\tilde{H}(\vec{p}) = \frac{1}{D}\sum_{m=1}^{D}\left(\frac{|\tilde{H}_m^{\text{mea.}} - \tilde{H}_m^{\text{mod.}}(\vec{p})|}{|\tilde{H}_m^{\text{mea.}}|}\right), \tag{2.10}$$

where D is the number of device configurations including different coil orientations, Tx–Rx separations and measurement frequencies. Note that (2.10) assumes a constant relative standard deviation (STD) in the data.

Because the EM model is computationally expensive, the minimization of the objective function is optimized by using a two-step inversion approach consisting of a global search technique which is followed by a local search (see figure 2.1). The global search (figure 2.1c) evaluates the misfit functions using the fast LS model (equation 2.1 - 2.3) over a regular grid. When all EMI configurations return a similar apparent conductivity, the medium is more or less homogeneous, whereas if the obtained apparent conductivities differ, electrical conductivity changes with depth can be expected. Therefore, the search range is optimized using the mean apparent electrical conductivity ($\overline{\sigma_\text{a}}$) and its STD to calculate the grid limits $\sigma_{\{\text{min,max}\}} = \overline{\sigma_\text{a}} \mp 3 \cdot \text{STD}(\sigma_\text{a})$, where seven linear distributed grid values are used for σ_1 and σ_2. The grid limits for the thickness of the first layer are $h_{1,\,\text{min}} = 0.2 \cdot \min(s)$ and $h_{1,\,\text{max}} = 0.8 \cdot \max(s)$ and, because of the smaller sensitivity which is discussed later in more detail, 30 linear distributed grid values are used for h_1 (see figure 2.2b). The parameters with the two smallest misfits are then used as starting models for the local search (figure

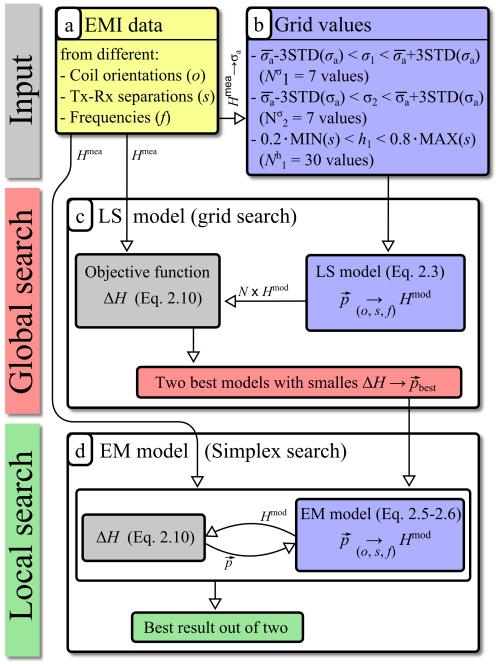

Figure 2.1.: Flow chart of the novel EMI inversion which is based on a combined global and local search algorithm using multiple measurements for each position (with different combinations of coil orientations, Tx–Rx separations and measurement frequencies). $N = N^{\sigma_1} \cdot N^{\sigma_2} \cdot N^{h_1}$ is the number of start models for the grid search and $\vec{p}$ is the parameter vector containing the conductivity of the first and second layer (σ_1, σ_2) and the thickness of the first layer (h_1).

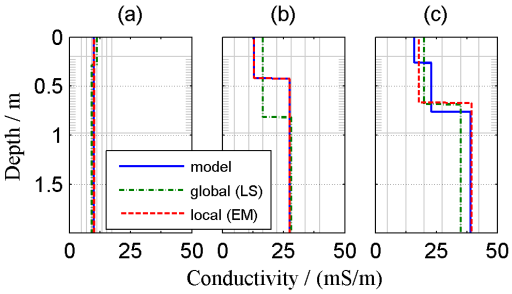

Figure 2.2.: Synthetic inversion results for a (a) homogeneous, (b) two-layer and (c) three-layer soil model (solid blue line). The dashed green line is the result of the global search (figure 2.1c) and the dashed red line is the result after local minimization (figure 2.1d). Grey lines and ticks show the discrete parameter values used for the grid search.

2.1d) which is based on the simplex algorithm (Lagarias et al. 1998) and uses the highly accurate EM model (equation 2.5 and 2.6). The simplex algorithm belongs to the class of direct search methods and is an unconstrained nonlinear optimization that does not use numerical or analytical gradients. The smallest misfit obtained with the two starting models is considered as being the global minimum. Note that a combined global and local optimization is very efficient for the minimization of misfit functions that depend on a limited number of parameters. Another important benefit is that no damping parameter is used which smears out the boundaries between layers to obtain smooth minimum structure models. In the case of agricultural soils, layered models are often capable of representing the actual geology more accurately than smooth minimum structure models.

2.2. Materials and Methods

2.2.1. Synthetic Data

The novel two-layer inversion algorithm is applied on three synthetic models: a homogeneous model with a conductivity of $\sigma = 10$ mS/m, a two-layer earth with $\sigma_1 = 13$, $\sigma_2 = 28$ mS/m, and $h_1 = 0.42$ m, and a three-layer soil model with $\sigma_1 = 16$, $\sigma_2 = 23$, $\sigma_3 = 39$ mS/m, $h_1 = 0.26$ and $h_2 = 0.50$ m (see solid blue lines in figure 2.2). Synthetic data are calculated for six EMI configurations using three 'Tx–Rx separation'-'measurement frequency' pairs: 1.00 m and 15 kHz, 1.22 m and 8 kHz, and 1.22 m and 15 kHz, each for HCP and VCP orientations. These setups are equal to the experimental data discussed later. Figure 2.2

Table 2.1.: Data and model misfit after global (figure 2.1c) and local search (figure 2.1d) for the three examples shown in figure 2.2. Small misfits are found for the (a) homogeneous and (b) two-layer soil model, whereas the misfit is increased for (c) a three-layer model.

soil model	global search		local search	
	data misfit	model misfit	data misfit	model misfit
homogeneous	22×10^{-3}	95×10^{-3}	2×10^{-9}	8×10^{-9}
two-layer	18×10^{-3}	190×10^{-3}	1×10^{-9}	2×10^{-9}
three-layer	18×10^{-3}	140×10^{-3}	1×10^{-3}	100×10^{-3}

indicates the global search grid values with horizontal and vertical grey lines for the heights and conductivities, respectively. Note that the true medium parameters are present between the global search grid values. As expected, the global search returns a model (dashed green line) with conductivity and thickness values lying on the global search grid that is close to the true model (solid blue line). For the two-layer case, the thickness of the first layer value is relatively far from the true thickness of the first layer. The local search results, which are based on the more accurate EM model and the unconstrained simplex search, are shown in figure 2.2 with dashed red lines. For the homogeneous and two-layer case, the model is well reconstructed and overlies the curve of the true model (solid blue line). For the three-layer model, the inverted layer boundary is close to the lowest interface between layers two and three of the soil model. The inverted electrical conductivity of the first layer approximates a mean value of the upper two layers of the soil model and indicates that the inversion finds the layer boundary at the most significant conductivity change in the soil. In addition to the data misfit, which is used as objective function during the inversion process, the normalized absolute conductivity deviation between the modeled ($\sigma^{\text{mod.}}$) and the inverted soil conductivity ($\sigma^{\text{inv.}}$) is integrated over the depth (z) and the average model misfit ($\Delta\sigma$) is introduced which is given by

$$\Delta\sigma = \frac{1}{N}\left(\sum_{i=1}^{N}\frac{|\sigma^{\text{mod.}}(z_i) - \sigma^{\text{inv.}}(z_i)|}{|\sigma^{\text{mod.}}(z_i)|}\right). \tag{2.11}$$

Table 2.1 shows the relative data and model misfits obtained from the global and local search for the homogeneous, two-layer, and three-layer model. Due to the coarse grid in the global search, relatively large data misfits and model misfits are obtained for all soil models (table 2.1). After the local search, the data and model misfits are strongly reduced for the

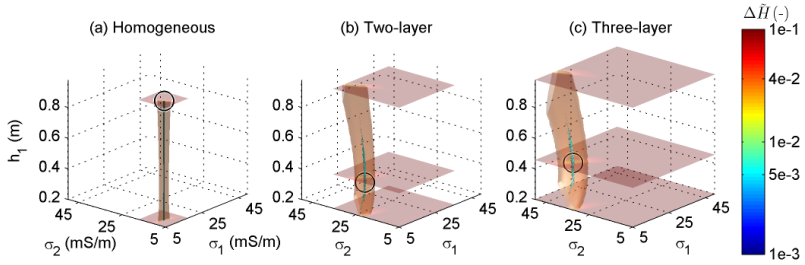

Figure 2.3.: Isosurfaces of the data misfit $\tilde{H} = 4 \times 10^{-2}$ (orange) and 5×10^{-3} (cyan) using the EM model as function of σ_1, σ_2, and h_1 for synthetic (a) homogeneous, (b) two-layer, and (c) three-layer models. For a better orientation, slices in the σ_1–σ_2-plane are inserted at the upper and lower limits. The global minimum is indicated by a circle.

homogeneous and two-layer model indicating a well constrained inversion that returns the model properties correctly as indicated in figure 2.2. Larger data and model misfits for the three-layer example show that it is significantly more difficult to describe a soil with more than two layers using the two-layer inversion. To investigate the minimization procedure in more detail, figure 2.3 shows isosurfaces of the misfit functions in a three-dimensional space for the inversion results shown in figure 2.2. Note that a denser grid with 100 values for each parameter is used compared to the previously shown inversions (figure 2.2). As expected for the homogeneous earth, the minimum is spread along the h_1-axis, since the inverted height is arbitrary (figure 2.3a). Note that the minimum is well constrained in the σ_1-σ_2-plane and the conductivity values are the same for all values of h_1 and close to the true conductivity value of the homogeneous half-space model (10 mS/m). For the two-layer earth (figure 2.3b) the isosurfaces indicate a high sensitivity for the layer conductivities and a smaller sensitivity for the thickness of the first layer. The use of more grid values (30) for the layer thickness in the global search, compared to the seven grid values for each of the layer conductivities, compensates for the smaller sensitivity. In combination with the local search (see figure 2.1), the global minimum could be accurately localized and the medium parameters were correctly reconstructed (figure 2.2b). For the three-layer model (figure 2.3c), similar relative sensitivities can be observed, although the isosurface $\tilde{H} = 4 \times 10^{-2}$ is wider and more bend through the conductivity-plane of the plot. Again, the global minimum could be determined, but the final misfit (see table 2.1) is increased compared to two-layer and homogeneous models, and may therefore be useful as indicator for data with more than two

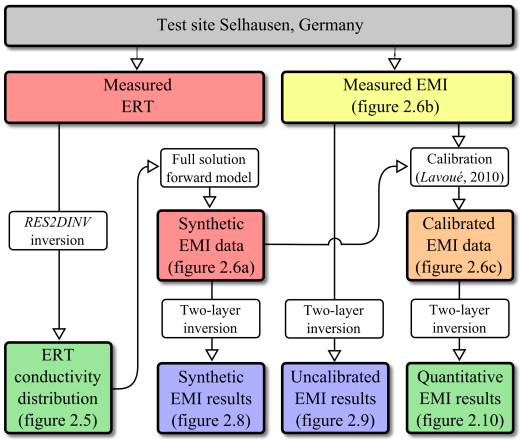

Figure 2.4.: Flow chart of the main processing steps performed on the measured ERT and EMI data. The ERT conductivity distribution was used to calculate synthetic EMI data which are used to calibrate the measured EMI data. The synthetic, uncalibrated and calibrated data were inverted using the novel two-layer multi-configuration inversion algorithm.

layers.

2.2.2. Experimental Data

Electromagnetic induction data were measured over a 120 meter long transect on the Selhausen test site of the Forschungszentrum Jülich GmbH, Germany. The profile was taken along a grid where soil samples were taken in intervals of 10 m with a depth of 0.3 m. Additional samples with 0.9 m sampling depth were taken every 30 m. Each 0.3 m long part of the sample was analyzed using sieve and pipette analyses. The uppermost 0.3 m of the first part of the profile is dominated by silt (70%), whereas the second part contains less silt (52%) and more sand (35%) instead (Weihermüller et al. 2007; Bornemann et al. 2010; Jadoon et al. 2010). The field is inclined up to 4° with the lower part at the beginning of the transect. In addition to the EMI data, an ERT measurement was performed on the same transect and day (Lavoue et al. 2010). The ERT inversion results are processed into synthetic EMI data, which are used to calibrate the measured EMI data. The synthetic EMI data and the uncalibrated and calibrated experimental EMI data are inverted using the novel two-layer inversion. An overview of all measured and calculated datasets, which are involved in the following processing steps, is given in figure 2.4.

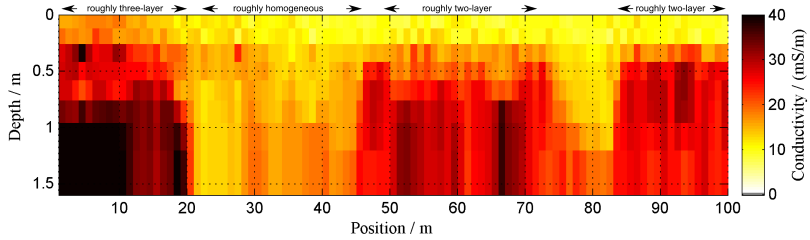

Figure 2.5.: Electrical resistivity tomography (ERT) inversion results along the reference profile showing lateral and vertical conductivity variations. The profile can be roughly divided into homogeneous, two-layer and three-layer soil regions.

Electrical Resistivity Tomography Data

Electrical resistivity tomography data were measured using a SYSCAL Pro system (IRIS Instruments, Orleans, France) with 120 electrodes and an electrode separation of 0.25 m. Seven profiles, each 30 m long, were measured in dipole-dipole configuration with an overlap of 15 m. The overall profile was 120 m long, although the inverted data were cropped at both ends to obtain equal depth-resolution (Lavoue et al. 2010). For the inversion, the RES2DINV program[2] was used. The inversion returns conductivity values for every meter at nine depth levels down to a depth of 1.4 m (figure 2.5). The ERT data show an upper layer of approximately 0.3-m thickness with conductivities of 20 mS/m for the first 20 m of the profile and 10 mS/m for the remaining 100 m. Roughly, the dataset can be classified into three soil types with different layering: Homogeneous regions with conductivities of approximately 13 mS/m can be found between position 20 and 45 m and between 75 and 85 m; two-layer regions with $\sigma_1 \approx 10$, $\sigma_2 \approx 25$ mS/m and $h_1 \approx 0.3$ m are present from 50 to 70 m and 90 to 100 m; a three-layer region with $\sigma_1 \approx 15$, $\sigma_2 \approx 25$ and $\sigma_3 \approx 40$ mS/m, and $h_1 \approx 0.25$ and $h_2 \approx 0.8$ m is present along the first 20 m.

Electromagnetic Induction Data

Six different EMI datasets were measured along the reference profile. The EM38 system with 1.00 m Tx–Rx separation and 15 kHz, and the Profiler system with 1.22-m Tx–Rx separation and 8 and 15 kHz were used to measure in HCP and VCP orientations. Each setup was placed on the ground every meter along the profile to measure. The data were smoothed using a

[2]Geotomo Software Sdn. Bhd., Gelugor, Penang, Malaysia.

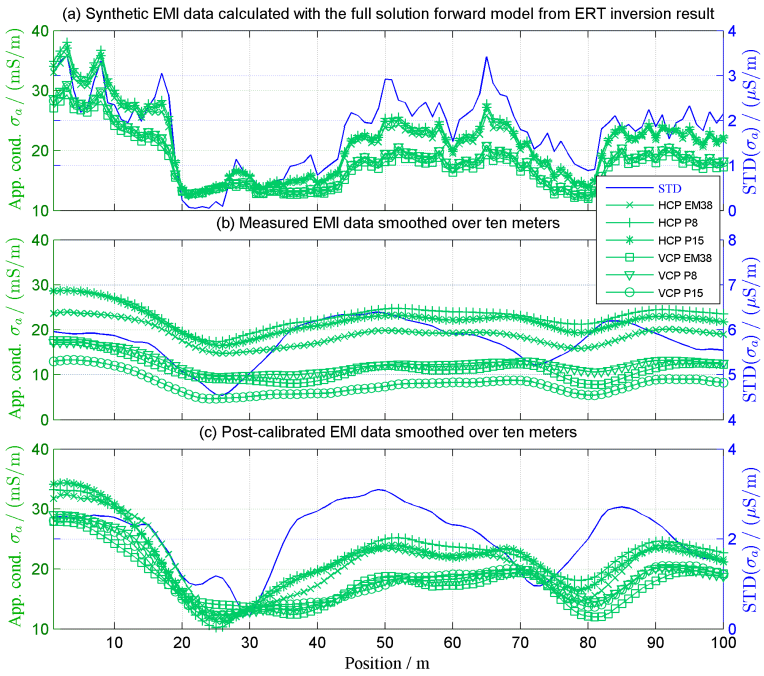

Figure 2.6.: (a) Synthetic, (b) measured and (c) post-calibrated EMI data for the same profile as in figure 2.5. The measured data is smoothed by a simple moving average over 10 positions. Green lines show the apparent conductivity for all HCP and VCP measurements of EM38, Profiler at 8 kHz (P8), and Profiler at 15 kHz (P15); blue lines are the STD at each position. A small STD indicates a more homogeneous area.

moving average over ten meters to reduce the influence of statistical errors. The multi-layer ERT conductivity distribution shown in figure 2.5 is used as input for the EM model (equation 2.5-2.7) and figure 2.6a shows the obtained synthetic apparent conductivity values for the same EMI configurations as used for the experimental measurements which are discussed later. Note that a locally horizontal layered earth is assumed and therefore the influence of adjacent variations on a single measurement point are neglected. Comparing these synthetic results with the measured apparent conductivity values shown in figure 2.6b shows that the latter contain data shifts which depend on the specific instrument and configuration. The measured EMI data in figure 2.6b are calibrated with the synthetic EMI data shown in figure 2.6a using a linear regression and following the procedure described by Lavoue et al. (2010). Although only one offset and scale factor has been used to calibrate each EMI configuration for the whole transect, the calibrated data are similar to the synthetic data (2.6c). For the

homogeneous regions around 25 and 75 m in the ERT data similar apparent conductivity values are obtained for different configurations, which correctly indicate the presence of a homogeneous soil. The synthetic and calibrated EMI data show a similar trend: The HCP configuration contains larger conductivity values than the VCP and since the latter is more sensitive to the upper layer this indicates that the conductivity is increasing with depth. From the uncalibrated data, those observations are not possible due to erroneous instrumental shifts (compare figure 2.6b-c). The STD of the apparent conductivity responses calculated for the six configurations along the transect (solid blue lines in figure 2.6) clearly shows the presence of relatively homogeneous regions indicated by small STD-values; two-layer and three-layer regions are indicated by larger STD-values. These results show that the new method, which bases the global search range on the STD of the apparent conductivity values, is valid.

Information Content of Electromagnetic Induction Data

To investigate the information content in the apparent conductivity values for different coil orientations, Tx–Rx separations and measurement frequencies in more detail, the VCP data is subtracted from the HCP data, the 1.00-m Tx–Rx separation data from the 1.22-m data and the 15-kHz from the 8-kHz data, and the results are shown in figure 2.7a, c and e, respectively, for the synthetic data. For different coil orientations the largest amplitudes are obtained, whereas the data for different Tx–Rx separations show intermediate amplitudes and different measurement frequencies show small differences. Note that all results show the same shape, only with smaller amplitudes and all data indicate that the medium has an increasing conductivity with depth (HCP setups, larger Tx–Rx separations and lower measurement frequencies have a larger sensing depth than VCP, smaller Tx–Rx separations and higher measurement frequencies). Figure 2.7a shows two regions with small differences, which are around position 25 and 75 m and correspond to the homogeneous regions observed in the ERT data (figure 2.5). Due to the different instrumental sensing depths, larger differences are present for the two-layer and three-layer regions, similar to the STD results shown in figure 2.6. Furthermore, figure 2.7b, d and f show the corresponding apparent conductivity differences in the experimental data. The information content in figure 2.7a and b is similar, showing two regions with small differences which correspond to the homogeneous regions observed in the ERT data. In contrast, the experimental data differ from the synthetic data for the Tx–Rx separation and measurement frequency differences in figure 2.7c-f. Synthetic

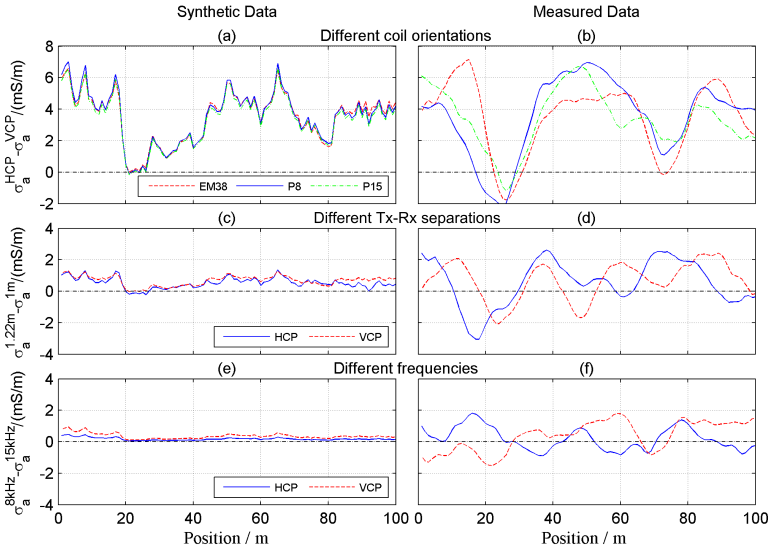

Figure 2.7.: Apparent conductivity differences for synthetic EMI data shown in figure 2.6a are calculated by subtraction of (a) VCP from HCP data, (c) 1.00-m Tx–Rx separation data from 1.22-m data, and (e) 15-kHz measurement frequency data from 8-kHz data. The large, intermediate, and small positive values for the different coil orientations, Tx–Rx separations and measurement frequencies, respectively, indicate the information content present in the data whereas all results correctly indicate an increasing conductivity with depth (see figure 2.5). Figures (b), (d), and (f) show the differences for the measured EMI data shown in figure 2.6c. The measured signals shows the same behavior like the synthetic data for the (b) coil orientations, but is probably superimposed with statistical system errors for the (d) Tx–Rx separations and (f) measurement frequency data.

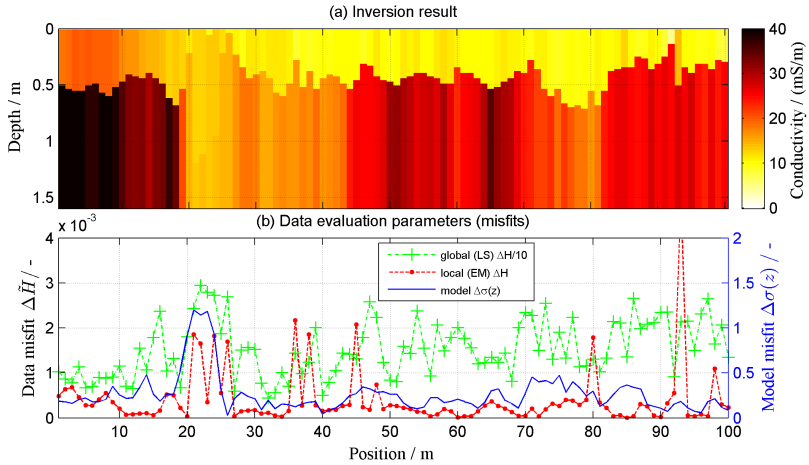

Figure 2.8.: (a) Two-layer inversion result using synthetic data calculated from the ERT-conductivities (figure 2.5) as input where for each position an inversion is performed. (b) Corresponding global (dashed green line, $\Delta\tilde{H}/10$) and local (dashed red line, $\Delta\tilde{H}$) data misfit as well as the model misfit (blue line, $\Delta\sigma$).

modeling showed that including Gaussian distributed white noise cannot reproduce the errors present in figure 2.7d and f. A possible explanation for these observations is the presence of local statistical system errors.

2.3. Results and Discussion

2.3.1. Synthetic Data

The synthetic EMI data (see figure 2.6a), calculated using the ERT inversion results shown in figure 2.5, are inverted for a horizontally layered two-layer medium using equation 2.11 and the combined global and local search minimization. Figure 2.8a shows the two-layer inversion results which reveal similar structures and electrical conductivity values compared to the ERT inversion results shown in figure 2.5. The roughly homogeneous and two-layer regions indicated in figure 2.5 can be clearly observed in figure 2.8. The two-layer inversion of the three-layer earth present in the first 20 m of the profile (see figure 2.5) returned similar results as the synthetic model shown in figure 2.2c: roughly the mean depth of the layer interfaces is obtained as thickness of the first layer ($h_1 \approx 0.5$ m), the electrical conductivity of the upper layer is a mean value of the electrical conductivity of the upper two layers of

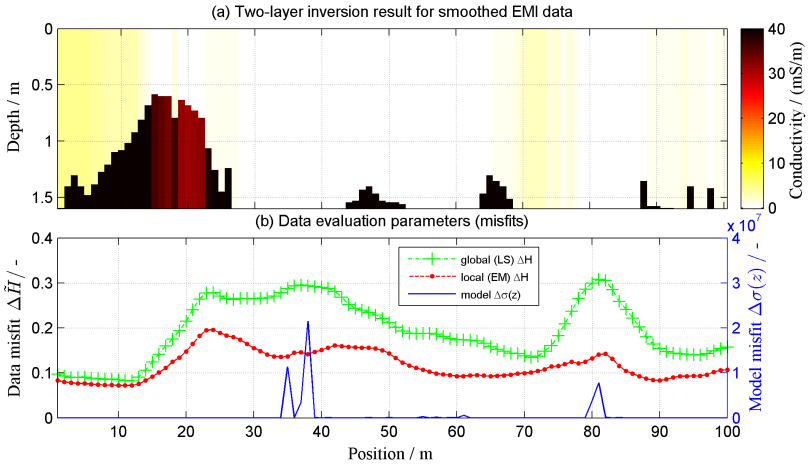

Figure 2.9.: (a) Two-layer inversion results for the uncalibrated EMI measurements shown in figure 2.6b. Due to the remaining instrumental shift the inversion is not able to find a reliable quantitative inversion result for the conductivity distribution. (b) Data and model misfits show relatively large misfits in comparison with figure 2.8.

the ERT data, and the lower half-space conductivity is well reconstructed. Only for the deep interface at around 80 m the interface is reconstructed too shallowly, which is due to a smaller sensitivity at that depth for the used Tx–Rx separation. Additional larger Tx–Rx separations would result in a better localization of deeper layer interfaces. Figure 2.8b shows the data misfit obtained from the global search (green dashed line) and the local search (red dashed line) including the model misfit (solid blue line). Similar to the synthetic model inversions shown in figure 2.2 and table 2.1, the data misfit obtained by the global search is significantly reduced by the local simplex search. Small values in the local (EM) data misfit indicate that the measurements can be well fitted with a two-layer model, which is confirmed by comparison of the obtained inversion results with the input model shown in figure 2.5. Note that in general a larger data misfit indicates the presence of a three-layer earth, or a more complicated multi-layer earth. These results are similar as obtained in figure 2.2 and table 2.1.

2.3.2. Experimental Data

Inversion of the uncalibrated EMI data shown in figure 2.6b did not converge to reliable quantitative results (see figure 2.9). The inversion results of the post-calibrated measured

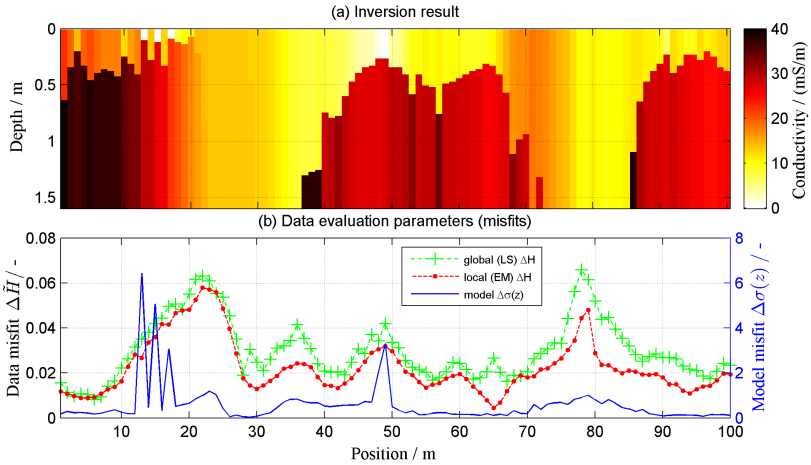

Figure 2.10.: (a) Two-layer inversion results using calibrated measured data (figure 2.6c) as input where for each position an inversion is performed. (b) Corresponding global (dashed green line, $\Delta\tilde{H}$) and local (dashed red line, $\Delta\tilde{H}$) data misfits as well as the model misfit (blue line, $\Delta\sigma$). Comparing those results with the ERT results shown in figure 2.5 reveals that most of the lateral and vertical conductivity values are well reconstructed.

EMI data shown in figure 2.6c are presented in figure 2.10. Similar structures and quantitative conductivity values are obtained as from the ERT inversion results shown in figure 2.5 and the synthetic inversion results shown in figure 2.8a. The inversion results for the roughly homogeneous regions again return relatively homogeneous models and especially the two-layer regions show a good agreement with the ERT and synthetic EMI inversion results. The inversion of the three-layer region returns similar results as the inverted synthetic EMI data. Note that using only one frequency of the Profiler measurements resulted in less good inversion results. Due to the use of multiple measurement frequencies, the influence of the local statistical system errors, as observed in figure 2.7d and f, is probably reduced. Some anomalous inversion results can be observed around positions 18 and 48 m, where non-physical low conductivities and shallow thicknesses for the first layer are obtained. These anomalies are also indicated by the model misfit and are probably due to inconsistent measurement data. Other differences between the inverted synthetic and experimental data can probably be explained by the assumption of a horizontally layered earth in the calibration and inversion procedure. These inversions of multi-configuration EMI data show that the main structures and quantitative conductivity values can be obtained and are in good agreement to those

obtained by ERT measurements. An important benefit of the EMI measurements compared to the ERT measurements is the inductive coupling, which enables fast measurements, whereas ERT needs a galvanic coupling, which limits the measurement speed.

2.4. Conclusions

A novel two-layer EMI inversion algorithm is introduced which uses the different sensing depths of multi-'coil orientation', multi-'Tx–Rx separation', and multi-'frequency' EMI data. The medium properties are reconstructed using a combined global and local optimization algorithm which jointly minimizes the difference between measured and modeled magnetic fields. Analyzing the information content contained in the different configurations shows for different coil orientations the largest differences, for different Tx–Rx separations intermediate differences and for different measurement frequencies the smallest variation. For a homogeneous half-space, all configurations return similar apparent conductivity values whereas for layered models varying apparent conductivities are obtained. The global search is initiated by using the mean apparent electrical conductivity and its STD to define optimum search limits for the layer conductivities. The optimal search limits for the thickness of the first layer are a function of the minimum and maximum Tx–Rx separations. Analysis of the global search which uses the fast LS model shows a better sensitivity for the electrical conductivities of the layers than for the thickness of the first layer. Therefore, more grid points are used for the layer thickness than for the electrical conductivities in the global search to obtain good start values. The model values with the smallest data misfits obtained by the global search are used as input in a local search algorithm, which is based on the simplex search and uses the EM model for the forward calculation. The parameter set with the smallest data misfit is assumed to be the global minimum which best describes the medium properties. Synthetic data shows a good reconstruction of homogeneous and two-layer models. For a three-layer model the lower layer interface was obtained reasonably well, and the conductivity of the lower half-space was well reconstructed. The inverted upper layer conductivity was the mean of the conductivity values of the upper two layers.

Coincident EMI and ERT data were collected at the Selhausen test site. The ERT inversion results show clear lateral and vertical changes in the soil conductivity. Synthetic EMI data obtained by applying an EM forward model on ERT inversion results indicate a clear shift in

the measured EMI data. This instrumental shift was eliminated by a linear regression calibration to obtain quantitative EMI measurement values (Lavoue et al. 2010). The synthetic EMI data were inverted using the two-layer inversion and show similar lateral and vertical conductivity properties as observed in the ERT inversion results. Moreover, inverted uncalibrated data resulted in unreliable inversion results, whereas the inversion of the calibrated experimental data returns lateral and vertical conductivity variations which are similar to inverted collocated ERT data and the inverted synthetic EMI data. Reliable quantitative EMI values are essential for this two-layer inversion. Any instrumental shift prevents the outcome of quantitative inversion results. The current quantitative calibration and inversion approach uses EMI data with HCP and VCP configurations, Tx–Rx separations of 1.00 and 1.22 m, and measurement frequencies of 8 and 15 kHz and is based on a horizontally layered medium, where the effects of lateral varying soil conductivities are neglected. It is expected that the use of more Tx–Rx separations and measurement frequencies will enable the inversion of models with three or more layers. Note that these EMI measurements are much faster carried out than the ERT measurements and that the presented novel two-layer EMI inversion returns similar information about the horizontal and vertical conductivity changes as inverted ERT data. Acquiring and inverting quantitative EMI data on large scales for a two-layer earth offer great potential for a wide range of applications.

3. Development and Drift-Analysis of a Modular Electromagnetic Induction System for Shallow Ground Conductivity Measurements[1]

As has been shown in the former chapter, multi-configuration electromagnetic induction (EMI) data enables the inversion for electrical conductivity over depth. The achievable depth-resolution depends on the quantity of used setups and their variance in the sensed soil volume, which is in general limited by the available EMI configurations and, if these are not included within a single instrument, the number of passes that is feasible for a survey in terms of measurement effort and time. In contrast, a multi-channel EMI system that provides flexible sensor configurations and multiple sensor channels will improve the resolution of the resulting electrical conductivity data and the efficiency of the survey, respectively. The focus of this chapter is on the design of a novel EMI system which enables to use modular transmitter (Tx) and receiver (Rx) units, which are connected to a central measurement system and are optimized for flexible setups with Tx–Rx separations of up to 1.0 m. Each Tx/Rx unit contains a coil, which is specifically adjusted for transmitting or receiving magnetic fields. All units enable for impedance measurements at the coils, which are used to simulate the electrical circuit and thereby analyze temperature-induced drift effects. A laboratory drift analysis at 8 kHz showed that 88 % of the drift in the measured data is due to the change in the electrical transmitter coil resistance. A measurement under field conditions proved that the novel EMI system is able to detect a test object with an electrical conductivity of 50 mS/m using a Tx–Rx separation of 0.3 m. In addition, the system allows in-field ambient noise spectra measurements in order to select optimal low-noise measurement frequencies.

[1] adapted from Mester et al. (2014).

3.1. Theory

3.1.1. Soil Conductivity Measurements

Frequency domain EMI measurements are based on the phenomenon that the magnetic field response (H_s^*) at the location of a receiver from a conductive soil is shifted in phase with respect to the transmitter signal (H_p^*) at the same location. The superposition (H^*) of both signals is measured with an EMI instrument. Note, that the asterisk indicates complex variables. In most cases, the exact solution of the problem for a homogeneous half-space (Wait 1982; van der Kruk et al. 2000) can be simplified by using the low-induction number (LIN) approximation which is valid for small angular frequencies (ω), small Tx–Rx separations (s) and small electrical soil conductivities (σ):

$$\beta = \sqrt{\frac{\omega\mu_0\sigma}{2}}s \ll 1. \tag{3.1}$$

Note that μ_0 is the magnetic vacuum permeability. For a Tx–Rx separation of 1.0 m, a measurement frequency (f) of 30 kHz and an electrical soil conductivity of less than 50 mS/m, the induction number (β) in (3.1) is always smaller than 0.08. The resulting response function for a homogeneous half-space yields the apparent electrical conductivity (σ_a) as given in (2.4):

$$\sigma_\mathrm{a} = \frac{4}{\omega\mu_0 s^2}\left|\frac{H_\mathrm{s}^*}{H_\mathrm{p}^*}\right|.$$

In particular, during an EMI measurement, the receiver voltage (U_Rx^*) is divided by the transmitter current (I_Tx^*), which results in the transfer impedance (Z^*)

$$Z^* = \frac{U_\mathrm{Rx}^*}{I_\mathrm{Tx}^*}. \tag{3.2}$$

The transfer impedance and the magnetic field strength are complex numbers with equivalent phase (φ) and amplitude information and, due to the normalization on the transmitter current in (3.2), the phase information in Z^* from multiple measurements and configurations has a common phase base.

Assuming that (I) the secondary magnetic field strength is shifted in phase by 90° with respect to the primary magnetic field strength, and approximating (II) for small phase angles $\Delta\varphi = \varphi - \varphi_0$ between the measured and the reference (calibration) signal, the ratio of the

secondary and the primary field in (2.4) can be rewritten as

$$\left|\frac{H_\mathrm{s}^*}{H_\mathrm{p}^*}\right| = \frac{|H_\mathrm{s}^*|}{|H_\mathrm{p}^*|} \overset{\text{(I)}}{=} \sin(\varphi - \varphi_0) \overset{\text{(II)}}{=} \Delta\varphi = \arg\left(\frac{Z^*}{Z_0^*}\right). \tag{3.3}$$

Thus, the apparent conductivity in (2.4) depends on the measurement configuration (Tx–Rx separation and measurement frequency) and the phase between the measured transfer impedance and the reference transfer impedance (Z_0^*). To describe the system requirement to measure the small secondary magnetic field strength in the presence of the large primary magnetic field strength at the receiver position, the required dynamic range (RDR) is introduced as

$$\mathrm{RDR} = \frac{|H_\mathrm{p}^*|}{|H_\mathrm{s}^*|}. \tag{3.4}$$

Using the magnetic dipole approximation for the primary magnetic flux of a coplanar configuration,

$$B = \mu_0 H = \frac{\mu_0}{2\pi}\frac{m}{s^3}, \tag{3.5}$$

and (2.4), (3.3) and (3.4), the dependency of H_p^*, H_s^* and RDR on the Tx–Rx separation is calculated and shown in figure 3.1 for a measurement frequency of 30 kHz, a soil electrical conductivity of 1 mS/m, a measurement rate of 2 Hz and a transmitter coil with a magnetic moment (m) of 15 mA·m^2. The RDR of the measurement system to resolve 1 mS/m with a Tx–Rx separation of $s = 1$ m is 10^5 at 5 kHz and $1.7 \cdot 10^4$ at 30 kHz. The RDR decreases with $1/s^2$. Note, that the data shown in figure 3.1 are based on the LIN approximation (2.4) by McNeill (1980). Measuring the small phase angles $\Delta\varphi$ and hence the large RDR is a major challenge. A common approach is to compensate the dominant primary magnetic field strength using analog circuits, thereby reduce the real part of the measured signal, and thus increase the phase angle between the real and imaginary part. However, the additional electrical components of such a compensation circuit are potential sources of drift effects. Furthermore, this compensation circuit needs to be adjusted for a fixed receiver location and the method is very sensitive to relative movements between Tx and Rx units. An alternative approach to overcome these limitations is to measure the small phase angles without analog compensation by using current high-resolution analog-to-digital converters (ADC's), instead.

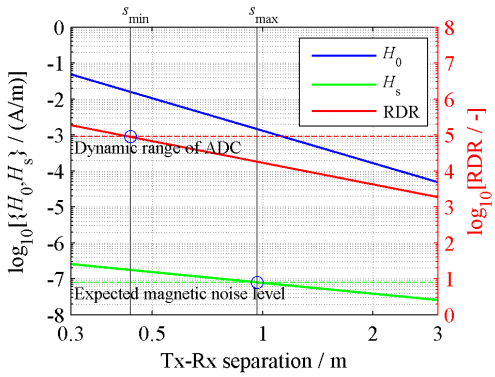

Figure 3.1.: Dependency of the secondary magnetic field strength ($|H_s^*|$, green line), the primary magnetic field strength ($|H_p^*|$, blue line) and the RDR (red line) on the Tx–Rx separation for a measurement frequency of 30 kHz, a soil conductivity of 1 mS/m and a transmitter coil with a magnetic dipole moment of 15 mA·m^2. The magnetic fields are plotted with respect to the axis on the left. The required dynamic range is labeled on the right. The dashed horizontal lines indicate the expected limits of the measurement system for an accuracy of 1 mS/m when using a measurement rate of 2 Hz. The marked interceptions are the corresponding expected Tx–Rx separation limits of the system, which are between 0.4 and 1.0 m. Note that these relationships are based on the LIN approximation (2.4) by McNeill (1980).

3.1.2. Primary Field Strength

The required primary magnetic field strength at the receiver position depends on the ambient noise level and the measurement rate. From the literature, the ambient magnetic noise level (B_{noise}) at field sites is expected to be about 10^{-13} T/$\sqrt{\text{Hz}}$ for frequencies between 1 kHz and 10 kHz (Fuellekrug and Fraser-Smith 2011). The measurement rate should allow to measure at a comfortable walking speed on a field, thus the sensitivity of the system is optimized for a measurement rate of 2 Hz, resulting in an integration time of $t_0 = 0.5$ s. In order to measure weak signals with a fixed frequency the lock-in technique is used. Therefore, the magnetic flux noise can be estimated based on the equivalent noise bandwidth of $1/(2t_0)$ (Zimmermann et al. 2005) and the expected ambient noise level, resulting in an magnetic flux noise level of 10^{-13} T. The signal response from the soil (secondary magnetic flux) needs to be larger than the ambient magnetic noise level and hence, to achieve the instrumental apparent conductivity-accuracy of 1 mS/m for a Tx–Rx separation of 1 m at 5 kHz ($RDR \approx 10^5$), the primary magnetic flux needs to be larger than $B_0 = B_{\text{noise}} \cdot \text{RDR} = 10$ nT at the location of the receiver. Using the dipole approximation (3.5) for large Tx–Rx separations with respect

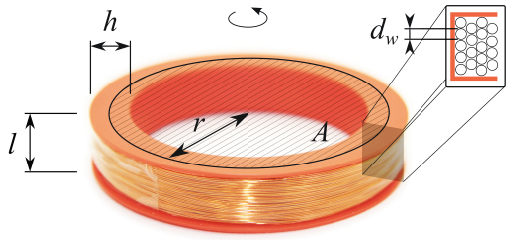

Figure 3.2.: Geometric properties of a coil are its length (l) along the symmetry axis, the radial coil height (h) of the wire layers, the coil radius (r), which is the mean radius here, and the effective coil area (A), which is based on the mean radius. In addition, the coil resistance (R) depends on the wire diameter (d_w).

to the coil radius (r), the required magnetic moment of the transmitter equals

$$m = \frac{2\pi}{\mu_0} B_0 s^3, \tag{3.6}$$

which results in $m_{\min} = 17$ mA·m^2 at 30 kHz, and 101 mA·m^2 at 5 kHz, for the transmitter system considering a reference Tx–Rx separation of 1 m.

3.1.3. Transmitter Optimization

Near-surface EMI instruments need to be portable in terms of size and weight, and need to be optimized in terms of bandwidth of the coils for all measurement frequencies of interest. Based on those criteria, different coil dimensions are investigated for maximal magnetic moment. In general, there are different ways to optimize a coil (figure 3.2) with N windings and its coil radius (r) for maximal magnetic moment

$$m = N\pi r^2 I^*_{\mathrm{Tx}} = N\pi r^2 \frac{U^*_{\mathrm{Tx}}}{R_{\mathrm{Tx}} + iL_{\mathrm{Tx}}}, \tag{3.7}$$

using a fixed transmitter supply voltage (U^*_{Tx}), and the transmitter resistance (R_{Tx}) and inductance (L_{Tx}) of the coil (Boll and Overshott 1989, pp. 212–216):

$$R_{\mathrm{Tx}} = \frac{8\rho r N}{{d_w}^2}, \quad L_{\mathrm{Tx}} \approx \frac{314.8 \cdot 10^{-7} r^2 N^2}{6r + 9l + 10h}. \tag{3.8}$$

The coil resistance (R) and inductance (L) depends on the number of coil windings (N) and the coil radius (r), and, in addition, the resistance depends on the specific electrical resistance (ρ) of the wire material and the wire diameter (d_w), whereas the inductance depends on the

height of the radial wire layering and the coil length (l) along its symmetry axis (figure 3.2). Note that (3.8) is also valid for the receiver resistance (R_{Rx}) and inductance (L_{Rx}). Since the mass of the copper wire is proportional to $(Nr\pi^2{d_w}^2)/2$, it is implicitly included in (3.7) and (3.8). Boundary conditions, like constant mass, constant length or constant radius, are important parameters for the coil optimization based on (3.7) and (3.8). In the following, some transmitter coil optimization approaches are discussed. First, the coil radius is kept constant and a long coil ($l \gg r, h$) is enlarged to x-times its length with x-times the number of windings (increasing the mass), which results in a constant magnetic moment $m(r{=}\text{const.}){=}\text{const.}$ Next, increasing the coil radius for a flat coil ($r \gg l, h$) results in $m \propto r$. Increasing the number of coil windings (N) while maintaining the mass by decreasing the wire diameter leads to $m(\text{mass}{=}\text{const.}) \propto 1/N$. Increasing the coil radius for constant mass and number of coil windings results in $m(\text{mass}{=}\text{const.}, N{=}\text{const.}, R \ll \omega L) \propto r$ and $m(\text{mass}{=}\text{const.}, N{=}\text{const.}, R \gg \omega L) \propto \text{const.}$

Furthermore, in order to measure the current in the transmitter circuit, a shunt resistor (R_{s}) is included which influences the optimal number of windings and therefore needs to be considered as an additional resistance in series to R_{Tx} in (3.7), when calculating the magnetic moment

$$m = \pi r^2 N \frac{U_0}{R_{\mathrm{s}} + R_{\mathrm{Tx}} + i\omega L_{\mathrm{Tx}}}, \tag{3.9}$$

based on the generator voltage (U_0). In addition, the coil impedance in combination with the shunt resistor determines the transmitter current (I^*_{Tx}), which needs to fit to the power specification of all included components and also influences the power consumption and thus the measurement time for a chosen battery, when measuring remotely.

Considering these relationships, a favorable transmitter coil design is flat (short) and has a radius as large as possible while being small compared to the smallest Tx–Rx separation (s) of interest. In addition, the wire diameter and the number of coil windings are optimized for maximal magnetic moment (smallest impedance $Z_0 = R_{\mathrm{s}} = R_{\mathrm{Tx}} + i\omega L_{\mathrm{Tx}}$) by varying the number of coil windings while maintaining the chosen coil dimensions. Finally, the power specifications of all electrical components need to be considered.

3.1.4. Receiver Coil Design

Similar to the transmitter coil, the best sensitivity of the receiver coil is achieved for the flat shape with the coil radius being as large as possible, but small compared to the Tx–Rx separation. Therefore, the shape of the transmitter coil is also ideal for the receiver. The number of windings is optimized for maximal sensitivity, and a thermal noise voltage (U_{nt}) which fits to a suitable low-noise amplifier.

First, the coil sensitivity (S) is calculated in the frequency domain using Faraday's law for the induced voltage ($U_{\mathrm{ind.}}$) in a coil and approximating for a spatially constant magnetic flux (B) through the Rx-coil area (A_{Rx}):

$$S = \frac{U_{\mathrm{ind.}}}{B} = -i\omega N_{\mathrm{Rx}} A_{\mathrm{Rx}}. \tag{3.10}$$

The sensitivity increases linearly with the number of Rx-coil windings (N_{Rx}). Furthermore, the number of windings and the wire diameter needs to be optimized with respect to noise performance in combination with a suitable amplifier. Three sources of voltage noise are considered in the receiver (Rx) system: First, the thermal noise voltage from the coil resistance, which is $\sqrt{4k_{\mathrm{B}}TR_{\mathrm{Rx}}}$ with the Boltzmann constant (k_{B}) and the coil temperature (T) in Kelvin, second, the specified input voltage noise of the amplifier (U_{na}), and third, the voltage $U_{I,\,\mathrm{na}} = I_{\mathrm{na}} Z_{\mathrm{Rx}}$, which is caused by the input current noise of the amplifier (I_{na}) in combination with the receiver coil impedance (Z_{Rx}), which is $Z_{\mathrm{Rx}} = R_{\mathrm{Rx}} + i\omega L_{\mathrm{Rx}}$. The overall voltage noise (U_{n}) is the quadratic sum of the three described noise sources:

$${U_{\mathrm{n}}}^2 = {U_{\mathrm{nt}}}^2 + {U_{\mathrm{na}}}^2 + {U_{I,\,\mathrm{na}}}^2. \tag{3.11}$$

3.1.5. Numerical Model

Thermal drifts are caused by a changing coil impedance according to the specific temperature coefficient of the wire material or temperature related physical deformation, e.g. inside the coils, leading to a variation in its inductance and the parasitic capacitance. The latter has its origin in the vicinity of the coil windings, which causes that two narrow wires with their lacquer layer in between act as a capacitor. In general, all electrical components experience thermal drifts, including the amplifier system, shunt resistor, load resistor, etc. Such a thermal drift can be caused by a change of the ambient temperature or the system power

itself, the latter resulting in a more time varying drift during system heat-up. Note that drift effects due to small displacements of the sensor coils, e.g. due to thermal deformation of the setup, are negligible for an uncompensated system, which is not the case for systems with a fixed analog cancellation of the primary field. In order to correct for drift effects, the entire electronic system is modeled in a "Simulation Program with Integrated Circuit Emphasis" (SPICE)[2], where each coil is represented by a resistor $R_{\{\mathrm{Tx,\ Rx}\}}$ and an inductor $L_{\{\mathrm{Tx,\ Rx}\}}$ in series and a parallel capacitor $C_{\{\mathrm{Tx,\ Rx}\}}$. All electrical coil parameters can be calculated from the mechanical coil properties or can be derived from the measured impedances

$$Z_{\mathrm{Tx}} = \frac{1}{\frac{1}{R_{\mathrm{Tx}}+i\omega L_{\mathrm{Tx}}} + i\omega C_{\mathrm{Tx}}}, \tag{3.12}$$

when connecting all coils as transmitters, measuring with multiple angular frequencies (ω) and solving the arising equation system. The electrical properties of additional standard circuit components are taken from the corresponding data sheets.

Next, the mutual inductance (M) and in particular the coupling coefficient (k) between the coils needs to be derived. A first approximation can be based on the dipole approximation for the transmitter coil and a homogeneous magnetic flux distribution over the Rx-coil area. The mutual inductance is then given by the transfer impedance (Z^*):

$$M = \frac{U_{\mathrm{ind.}}}{i\omega I^*_{\mathrm{Tx}}} = \frac{Z^*}{i\omega} = \frac{\mu_0}{2\pi}\frac{N_{\mathrm{Tx}}N_{\mathrm{Rx}}A_{\mathrm{Tx}}A_{\mathrm{Rx}}}{s^3}, \tag{3.13}$$

which is based on the transmitter current in the transmitter coil, and the induced voltage in the receiver coil. The former can be derived by comparing (3.6) and (3.7). The latter is approximated for a sinusoidal signal and for $\vec{B}_0 \parallel \vec{A}_{\mathrm{Rx}}$ by

$$U_{\mathrm{ind.}} \approxeq \left| N_{\mathrm{Rx}} \cdot i\omega B_0 A_{\mathrm{Rx}} \right|. \tag{3.14}$$

In order to describe short-offset measurements where the dimensions of the transmitter and receiver coils need to be considered for the field calculation, the transmitter dipole in (3.13) is replaced by a finite number of line segments and the magnetic flux is calculated using Biot-Savart's law (Strassacker and Strassacker 1993):

$$B = \frac{I^*_{\mathrm{Tx}}\mu_0}{2\pi b}\left(\frac{s_1}{\sqrt{s_1^2+b^2}} - \frac{s_2}{\sqrt{s_2^2+b^2}}\right). \tag{3.15}$$

[2] Winspice v1.06, OuseTech Ltd., Cambridge, England.

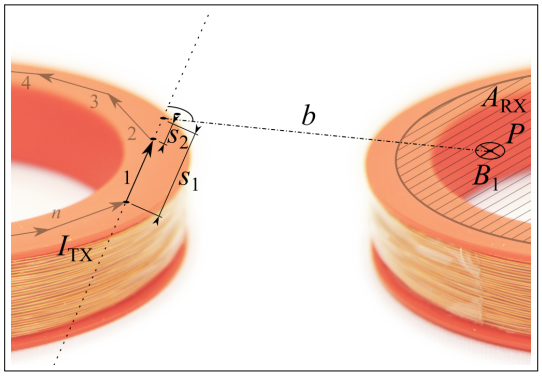

Figure 3.3.: This figure exemplary illustrates a transmitter coil with a numerical representation of line segments (left). The magnetic flux B_1 from segment 1 is calculated for the observation point P in the Rx-coil area (A_{Rx}) (right) using 3.15.

The distances s_1, s_2, and b are shown in figure 3.3.

This approximation is valid for quasi-static electromagnetic fields. In addition, the induction term (3.14) in (3.13) is replaced by its integral representation:

$$U_{\mathrm{ind.}} \approxeq \left| N_{\mathrm{Rx}} i\omega \int_{A_{\mathrm{Rx}}} B_0 \cdot \mathrm{d}A \right|, \tag{3.16}$$

which accounts for an inhomogeneous primary magnetic flux distribution through the effective coil area of the receiver coil. The integration itself is performed with MATLAB[3].

In circuit simulations, the mutual inductance is often normalized by the inductances (L) of the involved coils and called coupling coefficient (k):

$$k = \frac{M}{\sqrt{L_{\mathrm{Tx}} L_{\mathrm{Rx}}}}. \tag{3.17}$$

3.2. Materials and Methods

Development and optimization of the new electromagnetic induction (EMI) instrument was supported by laboratory experiments, field measurements and numerical simulations. First, the measurement system and the corresponding sensors with their properties are described. Afterwards, the experiments are explained, which are used to study the temperature dependency of the electrical coil parameters, to evaluate the sensitivity and accuracy of the

[3] using the `quad2d`-function.

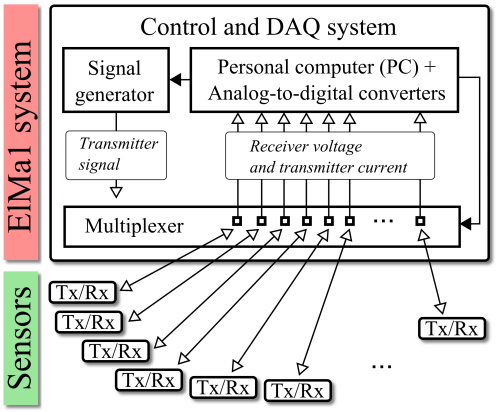

Figure 3.4.: The EMI system consists of a combined control- and DAQ system, which controls the multiplexer and the signal generator and acquires the data from multiple ADC's. All sensor units contain the transmitter and the receiver circuit shown in figure 3.5, between which can be switched remotely by the PC. Depending on its primary purpose, the sensors only differ in its coil properties. The number of Tx/Rx-units is limited by the number of multiplexer- and ADC-channels.

sensors and the system, respectively, and to validate the theoretical considerations by some worst-case scenarios.

3.2.1. Measurement System

The measurement system is based on the electrical impedance tomography (EIT) system described by Zimmermann et al. (2008), where electrodes are used to measure the electrical impedance of a probe. Figure 3.4 shows the EMI system, that consists of a signal generator and a multiplexer unit, which are both connected to an integrated personal computer (PC) with PXI bus and analog-to-digital converter (ADC) boards. In contrast to the electrodes of the mentioned EIT system, here, the newly developed EMI receiver (Rx) and transmitter (Tx) units are connected to the multiplexer. The control and data acquisition (DAQ) system shown in figure 3.4 is the same as in Zimmermann et al. (2008).

The generator has a maximum output peak voltage of 10 Vp and is controlled by a PC using LabView[4]. This software also controls the multiplexer unit that switches the generator signal to a user-defined sensor channel. All sensor units are directly connected to the multiplexer from where a relay is switched to connect its coil either to the generator, when used in Tx

[4]NI LabView, National Instruments Corporation, Austin, TX, USA.

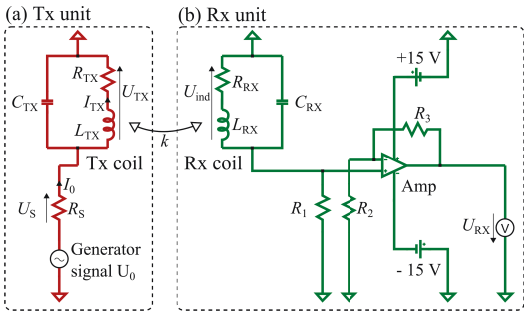

Figure 3.5.: Simplified circuit diagram of the sensor units. The transmitter (Tx) unit (a) is connected through the multiplexer to the generator voltage (U_0)generator output (see figure 3.1). The unit itself consists of an electrical coil and a shunt resistor (R_s) for the current measurement. The receiver (Rx) unit (b) is also based on an electrical coil which is connected to an amplification circuit (Amp) and a load resistance R_1. The amplified receiver voltage (U^*_{Rx}) is passed through the multiplexer into the analog-to-digital converters (ADC's) (figure 3.4).

mode (figure 3.5a), or to an amplification circuit (figure 3.5b), when it is used in Rx mode. Thereby, all units can be switched to Tx mode successively to measure its electrical coil properties.

The same software which controls the generator and the multiplexer also acquires the data from the ADC's and saves them for further post-processing steps. Note that the full time series of all sensor channels is stored. The used 24-bit sigma-delta ADC (NI4472 from National Instruments) has a fixed input voltage range of ±10 V and an amplitude resolution of 0.1 $\mu V/\sqrt{Hz}$, which is much greater than the amplitude resolution needed to resolve the soil response. In order to match the ADC data range, the induced receiver signal is amplified, accordingly. Note that the specified dynamic range of this ADC is $8.9 \cdot 10^4$ for a sampling rate of 100 kS/s. More details about the measurement system, the used ADC units and the sensors are given in chapters A.1 and A.4.

3.2.2. Sensors

Copper wire coils are used in the transmitter and receiver units. In order to match the far-field criterion for Tx–Rx separations (s) greater than 0.3 m, both coil formers have the same size and shape with an inner coil radius (r) of 30 mm, which is one tenth of the minimal Tx–Rx separation. The outer coil radius is 40 mm, the coil length (l) is 12 mm and the radial height of the coil windings (h) is 8 mm. All coil variables are declared in figure 3.2.

Depending on its purpose, the number of windings and the wire diameter is optimized for transmitter and receiver coils, respectively. An overview of the used coils and their properties is given in table 3.1.

Table 3.1.: Summary of the coil properties used in the transmitter (Tx) and receiver (Rx) units, respectively.

Coil property	Tx	Rx
Outer radius / mm	30	
Radial coil height (h) / mm	8	
Coil length (l) / mm	12	
Number of coil windings (N)	105	720
Wire diameter (d_w) (excl. lacquer) / mm	0.67	0.32
Resistance (R) / Ω	1.2	36
Inductance (L) / mH	1.2	51
Capacitance (C) / pF	80	70
Coil sensitivity (S) (5 - 30 kHz) / (mV/µT)	>12	>87

The transmitter coils are optimized for a measurement frequency (f) range between 5 and 30 kHz and a shunt resistor (R_s) with 100 Ω by using (3.7) and (3.8) (figure 3.6, solid lines). The accuracy of the current measurement, which is related to the amplitude of the voltage drop along the shunt resistor, increases with the value of the shunt resistor, while the magnetic moment (m) of the transmitter system decreases. Values between 10 and 100 Ω are a reasonable compromise for the ElMa1-system, resulting in a magnetic moment and voltage drop over the shunt resistor as can be seen in figure 3.6 and table 3.2, respectively. The optimum number of coil windings was selected for the reference frequency of 15 kHz, which is $N = 105$ for a wire diameter of 0.67 mm. Using the maximum generator voltage of 10 Vp and a shunt resistance of 100 Ω, the magnetic moment is between 16 mA·m^2 and 37 mA·m^2 for 30 kHz and 5 kHz, respectively. Although the coils are not optimized for a shunt resistor with 10 Ω, the resulting magnetic moment is larger throughout the investigated frequency range (figure 3.6, dashed lines), being between 18 mA·m^2 and 103 mA·m^2 for 30 kHz and 5 kHz, respectively, and thereby always larger than our aimed magnetic moment for a Tx–Rx separation (s) of 1 m, which is between 17 and 101 mA·m^2, respectively. Note that a more detailed overview of those and the following receiver and transmitter specifications can be found in table 3.2. Converting the magnetic moment of the coil at 30 kHz and for a shunt resistance of 10 Ω in a maximum Tx–Rx separation yields $s_\mathrm{max} = 1.1$ m for

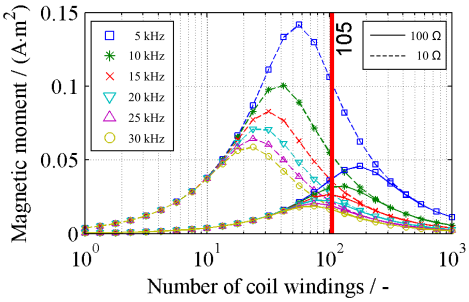

Figure 3.6.: The figure shows the magnetic moment of transmitter coils, which is calculated from (3.9) for shunt resistors of 10 Ω and 100 Ω, six measurement frequencies in the range of 5 kHz (blue curve) to 30 kHz (yellow curve), and a broad range of number of coil windings. By optimizing the magnetic moment for a shunt resistor of 100 Ω and a reference frequency of 15 kHz, an optimal number of 105 coil windings is obtained (red vertical line).

the expected ambient noise level of 10^{-13} T/$\sqrt{\text{Hz}}$. The measured electrical coil parameters at room temperature are about 1.2 Ω, 1.2 mH and 80 pF for the resistance, inductance and capacitance, respectively. Note that the coil is not driven in resonance to increase the spectral bandwidth and phase stability, and to reduce drift effects.

Table 3.2.: System specifications for an aimed instrumental accuracy of 1 mS/m at a Tx–Rx separation of 1.0 m and a measurement/integration time of 0.5 s. The given values are derived for the circuits shown in figure 3.5 combined with the coils described in table 3.1. The transmitter circuit is analyzed for shunt resistors (R_s) with 10 Ω and 100 Ω and for the frequency range between 5 and 30 kHz.

Transmitter property		Required	Achieved for R_s=10 Ω	Achieved for R_s=100 Ω
Magnetic moment / (A · m^2)	5 kHz	101	103	37
	30 kHz	17	18	16
Maximum Tx–Rx separation[a] / m		1.00	1.06	0.97
Power dissipation at shunt resistor / W		< 0.6	< 0.4	< 0.5
Voltage along shunt resistor / V	5 kHz	-	2.5	9.3
	30 kHz	-	0.4	4.0
Receiver property		**Required**	**Achieved**	
Dynamic range / -		$\geq 1.1{\cdot}10^6$	$\geq 8.9{\cdot}10^4$	
Noise performance / nV		< 9.0	< 5.7	

[a] considering $B_\text{noise} = 0.1$ pT/$\sqrt{\text{Hz}}$ and $f = 30$ kHz.

The receiver coils are optimized for an amplifier with an input voltage noise (U_na) of 3.5 nV/$\sqrt{\text{Hz}}$

and an input current noise (I_{na}) of 0.4 pA/$\sqrt{\mathrm{Hz}}$. Using (3.8) and (3.11), a coil with 720 windings and a wire diameter of 0.32 mm was found which, according to (3.10), has a worst-case sensitivity of $S = 87$ mV/µT at 5 kHz. Considering the targeted measurement of a magnetic flux density of 10^{-13} T, the resulting induced voltage is 9 nV at 5 kHz. The measured electrical coil properties at room temperature are about 36 Ω, 51 mH, and 70 pF, causing a thermal noise level of $U_{\mathrm{nt}} = 0.8$ nV/$\sqrt{\mathrm{Hz}}$ at 25°C for the coil resistance and an equivalent noise voltage between 0.6 nV/$\sqrt{\mathrm{Hz}}$ and 4.4 nV/$\sqrt{\mathrm{Hz}}$ at 5 kHz and 30 kHz, respectively, which is caused by the input current noise of the amplifier in combination with the coil. This results in an overall noise voltage between 3.6 nV/$\sqrt{\mathrm{Hz}}$ at 5 kHz and 5.7 nV/$\sqrt{\mathrm{Hz}}$ at 30 kHz, which is equivalent to 3.6 nV and 5.7 nV, respectively, using the equivalent noise bandwidth of $1/(2t)$ and a measurement time of $t = 0.5$ s. This estimated noise level is smaller than the smallest expected signal voltage of 9 nV, which is at 5 kHz.

Depending on the Tx–Rx separation, the resistors R_2 and R_3 (figure 3.5) are used to adjust the signal amplification to the dynamic range of the analog-to-digital converter (ADC). In addition, the load resistance R_1 is needed to suppress a resonant behavior in the receiver circuit. For a Tx–Rx separation of one meter, the amplification factor is adjusted to 511, resulting in an input signal due to the ambient magnetic noise of 4.5 µV at the ADC which is much larger than the specified voltage noise level of the used ADC, which is 0.1 µV for the assumed measurement time.

Based on (2.4), (3.3), and (3.4) the worst-case scenario in terms of dynamic range occurs for the smallest considered Tx–Rx separation of 0.3 m, resulting in a required dynamic range (RDR) of $1.1 \cdot 10^6$ at 5 kHz and for 1 mS/m, which is outside the specified dynamic range of the ADC ($8.9{\cdot}10^4$). Therefore, the expected instrumental accuracy for a Tx–Rx separation of 0.3 m drops to 13 mS/m and reaches 1.1 mS/m for $s = 1.0$ m, which roughly satisfies the initial aim of 1 mS/m at 1.0 m. Nevertheless, the following first experimental tests are all performed with $s = 0.3$ m to decrease the volume that influences the measurements and thereby the volume that needs to be controlled in order to evaluate the results.

3.2.3. Coil Shielding

Electromagnetic induction soil conductivity measurements are based on the analysis of the phase angle between the measured and the primary magnetic field, which is often represented

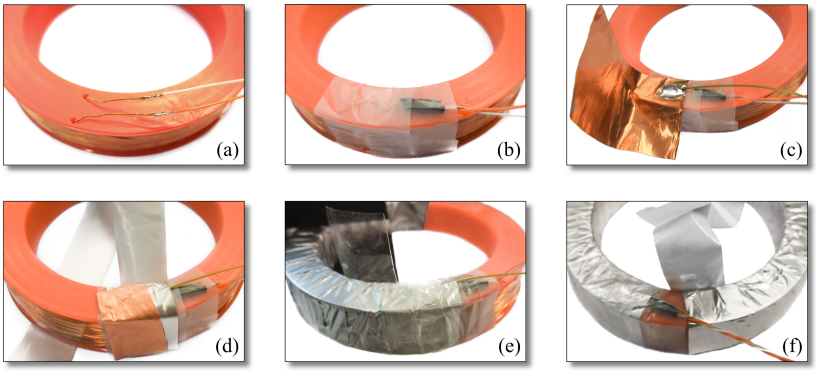

Figure 3.7.: The manufacturing process of the coil shielding is shown from an unshielded coil in the upper left corner to the completely shielded coil in the lower right corner in six steps.

by the imaginary part of the signal after its normalization on the primary field. The obtained apparent electrical conductivity (σ_a) is not only influenced by the secondary magnetic field from induced currents in the soil as described in (2.4), but may similarly be affected by capacitive effects which do not yield usable information about the soil electrical conductivity (σ), and, therefore, are treated as parasitic effects. In order to minimize errors due to capacitive effects, the used coils are toroidally shielded with aluminum tape. Starting with an unshielded coil (figure 3.7a), the connections are fixed and taped to the coil former (figure 3.7b). Next, a copper foil is used to connect the shielding with the ground-wire which is sold onto the foil (figure 3.7c). Afterwards, the actual shielding tape, which is made of aluminum, is wound toroidal around the coil. After the first winding, the copper foil is folded around the aluminum tape to ensure the electrical contact between both of them (figure 3.7d). It is important to avoid induced loop currents in the shielding. Therefore, the beginning of the toroidal shielding is electrically isolated by a non-conductive tape (figure 3.7e), before the last windings of the tape close the coil shielding completely (figure 3.7f). Finally, the ground-wire is connected to the ground-potential of the sensor board.

The influence of the shielding was tested under realistic measurement conditions on the campus of the research center. A setup with a shielded transmitter and receiver, and an unshielded transmitter and receiver, all mounted on the edges of a quadratic grid with Tx–Rx separations of 0.8 m, was used. In order to measure all combinations of effects, the transmitters and receivers were located on the diagonal edges, respectively. The measurement was performed

with a sinusoidal excitation signal with 1.5 Vp and measurement frequencies of 5, 10, 15, 20 and 30 kHz. In order to measure the differences in the data for the given frequencies under realistic conditions, the setup with the four sensors was first held up into the air at a height of about 2 m and then put directly on the ground. A single measurement had an integration time of 0.5 s per frequency. In order to evaluate the measurement noise, each of the five frequencies was measured 19 times. The complete test-sequence consists of a single measurement with each frequency in increasing order, followed by 19 repetitions. Afterwards, the transmitter channel was switched from the shielded to the unshielded transmitter and the sequence was repeated. Finally, the system was moved from the air-position to the ground and the whole sequence with both transmitters was measured again. The whole experiment lasted about four minutes.

3.2.4. Current Measurement

In order to obtain the transfer impedance using (3.2), the excitation current of the transmitter coil needs to be measured with equal or better accuracy than the receiver signal. Considering the electrical parameters of the transmitter coil (1.2 Ω, 1.2 mH) and the shunt resistor (10 Ω) the voltage level at the ADC for the current measurement is between 2.5 V and 0.4 V at 5 kHz and 30 kHz, respectively. As assumed before, the RDR is 10^5 at 5 kHz and $1.7{\cdot}10^4$ at 30 kHz, resulting in a voltage amplitude of 25 µV, which is much larger than the noise level of the ADC (0.1 µV). Most of the previous estimations of the system accuracy were performed for a Tx–Rx separation of 1 m. However, the worst-case in terms of RDR for the ADC is an instrumental accuracy of 1 mS/m with a Tx–Rx separation of 0.3 m at 5 kHz, resulting in RDR $= 1.1 \cdot 10^6$, which corresponds to the later used experimental setups. For this scenario, the ADC needs to resolve a voltage amplitude at the shunt resistor of 2.3 µV, which is still measurable with the specified voltage resolution of the ADC. In order to validate its dynamic range, a shunt resistor with 100 Ω was used to compare with the 10-Ohm-resistor measurements. By this approach, the accuracy of the current measurement is increased, because a higher voltage drop of 9.3 V at 5 kHz is now measurable at the shunt resistor. Considering the RDR of $1.1 \cdot 10^6$, the smallest voltage amplitude that needs to be resolved is 8.3 µV, which is about three times larger compared to the expected voltage drop at the 10-Ohm-resistor. Note that using a 100-Ohm-resistor reduces the magnetic moment of the transmitter and therefore results in a smaller estimated maximum Tx–Rx separation

of $s_{\max} = 0.97$ m. In addition, the power dissipation at the shunt resistor must be small enough to ensure a stable operation. The maximum current at a shunt resistor of 10 Ω is 0.25 A at 5 kHz, resulting in a power dissipation of 0.32 W. This is inside the manufacturer's specification of the used high-precision resistor. Considering noise and power dissipation, this is an optimal shunt resistance for the aimed configuration. Using the 100-Ohm-resistor results in a power dissipation of 0.43 W, which is also inside the specification. To validate the estimated dynamic range of the ADC, 17 repetitive measurements were performed at room temperature for both shunt resistors, each with a measurement time of 0.5 seconds. In order to measure the receiver coil properties, each sensor can be switched to transmitter (TX) mode (figure 3.5a) by the control software to obtain its electrical coil properties from separate measurements.

3.2.5. Simulation

All electrical components of the sensors (figure 3.5), and in particular their influence on the phase signal at the receiver, are analyzed using a "Simulation Program with Integrated Circuit Emphasis" (SPICE), where the measured electrical coil parameters (R, L, and C) are inserted. In order to simulate the amplifier, the SPICE model from the manufacturer is used. The temperature coefficients for R_1, R_2, and R_3 (figure 3.5) are taken from the corresponding datasheets. Next, the coupling coefficients (k) are calculated using (3.13), and (3.17) and a numerical representation of the transmitter (Strassacker and Strassacker 1993, p. 161) as well as a numerical integration over the effective Rx-coil area (A_{Rx}). The influence of the measured temperature drifts in the electrical coil properties on the apparent conductivity value is analyzed for each considered coil property by comparing the simulated apparent conductivity for a temperature stable property to the apparent conductivity simulated with the corresponding measured (drifting) property.

3.2.6. System Noise and Receiver Sensitivity Test System

In order to measure the ambient electromagnetic (EM) noise level, the Rx sensitivity and also the EM noise from the novel ElMa1 system, an additional measurement system was realized. It includes a single Rx unit, a 24-bit ADC with 192 kHz sampling frequency, and a laptop computer (see chapter A.5). The whole system is powered by batteries to avoid noise

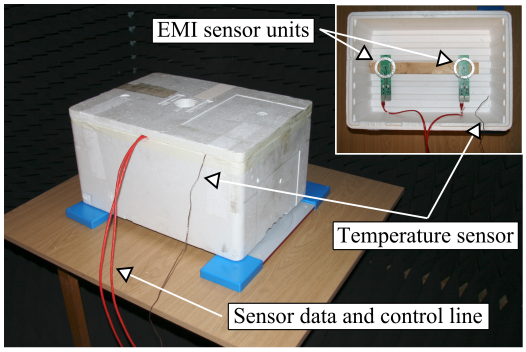

Figure 3.8.: Temperature induced drift effects are analyzed using an isolating box. Two sensor units are placed inside of it with a Tx–Rx separation of 0.3 m. To reduce artificial noise effects, all measurements were performed in our electromagnetic shielded room.

from power lines or transformers. With this setup, the sensor sensitivity was tested under controlled conditions and the ambient magnetic noise level as well as the system noise was evaluated at the different test sites.

3.2.7. Laboratory Setup

In order to validate the theoretical estimation of the receiver noise level, the electromagnetic noise sources of the measurement system itself and temperature-related drift effects in a laboratory, an electromagnetically shielded environment is necessary. Typically, the electromagnetic noise in a building is much larger than the estimated sensor noise level and the expected ambient magnetic noise level (B_{noise}) that limits the sensitivity of the system in the field. Therefore, the following measurements are performed in an electromagnetic shielded room, which is also suitable for studying temperature drifts of the system under controlled conditions. The room has metallic boundaries and is 2.2 m wide, 2.0 m high and 4.3 m long. The temperature in the room is conditioned at about 22°C. To avoid disturbances caused by induction effects related to the metallic walls, a transmitter-receiver pair with a small Tx–Rx separation of 0.3 m is placed as far as possible away from the walls. The sensors are mounted on a wooden bar, which is placed inside an isolating Styrofoam box about 0.8 m above the ground (figure 3.8). The measurement system (personal computer (PC), generator, multiplexer, ADC's, etc.) is placed in one corner of the room. The power supply inside this room is filtered to avoid noise from the power line.

In order to measure temperature effects, the sensor units are heated up indirectly using a low-temperature heat-gun, which is put into a centered hole in the cover of the box. When the temperature inside the box exceeds 50°C (which is roughly after 5 minutes) the heat-gun is removed and the box is closed to ensure a uniform cooling down of the sensors during the measurement. Both coils are alternatingly switched to Tx mode, measuring the impedance of the dedicated Tx coil at a 10-Ohm-resistor and that of the more resistive Rx coils at a 100-Ohm-resistor successively with eight measurement frequencies at each turn. This data set from frequencies between 3.3 kHz and 33 kHz enables to build up an equation system from (3.12) and thereby derive the electrical coil properties in a post-processing. In the simulation, a resistance of 1.8 Ω was added in series to (3.12) to consider the 5-m-long cable between signal generator and transmitter unit. Based on this data, the influence of each coil parameter on the measured apparent conductivity value is derived using SPICE simulations. The measurement was stopped, when the temperature inside the box reached 23°C. The apparent conductivity drift is measured in relation to the apparent conductivity value measured in the beginning of the experiment. Note that the system must not be moved during the measurement due to the influence of the metallic walls.

3.2.8. Field Setup

A first experimental test of the novel electromagnetic induction (EMI) system was performed on the campus of the research center. Two sensors were mounted on a PVC bar which was placed on a calibration rack, and on top of a test object with known conductivity, respectively (figure 3.9). The calibration rack is designed to measure one meter above the soil surface. As a test object with known homogeneous conductivity, a swimming pool with a diameter of 3.8 m and a water depth of 1.0 m was used. The sensors were placed on top of the pool with a separation of about 5 cm to the surface of the water.

A small Tx–Rx separation of 0.3 m was chosen to ensure that, according to McNeill (1980), about 85 % of the sensed volume is inside the pool, which was filled with approximately 11 m^3 of tap water, having a conductivity of (50 ± 1) mS/m. The conductivity of the water was measured using a Greisinger GLF 100 conductivity meter at different depths and positions in the pool. The soil beneath the pool had an conductivity of less than 10 mS/m (measured with a CMD-MiniExplorer from GF instruments). The measurement started with the sensors on the calibration rack, was continued above the water and ended back on the same calibration

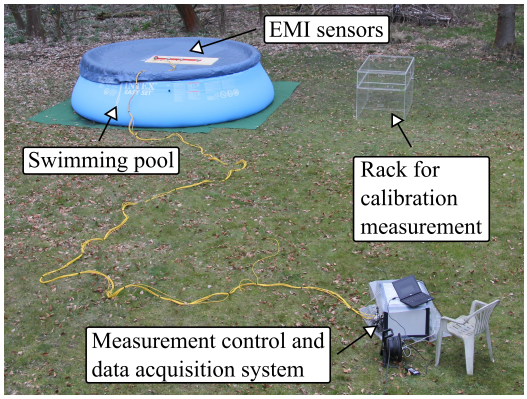

Figure 3.9.: The new EMI device is tested above a swimming pool, which is filled with tab water (50 mS/m). A panel with sensor units is placed approximately 5 cm above the water surface or on a 1 m high rack besides the swimming pool.

rack. Both sensors were connected to the measurement system by 20-m long RJ45 cables and were placed at least ten meters away from the main system (see figure 3.9). The system itself was powered by the power supply of a nearby building. Multiple frequencies were measured sequentially, each for 0.5 s, and both sensors were alternatingly switched to Tx and Rx mode for 12 times. The measurements during the movement of the sensor between the two locations were removed from the results. The amplitude of the frequency signal was 10 Vp and, in order to measure the Tx current, a shunt resistor with 100 Ω was used.

3.3. Results and Discussion

3.3.1. Noise and Sensitivity Test

The electromagnetic noise spectrum inside the shielded room (figure 3.10 strip a) exhibits a noise level of less than 30 nV/$\sqrt{\text{Hz}}$ in the region of interest between 5 kHz and 30 kHz, which is more than the expected noise level of the sensor ($<$ 5.7 nV/$\sqrt{\text{Hz}}$) and the expected noise level in the field (9 nV/$\sqrt{\text{Hz}}$ at 5 kHz). This noise spectrum does not change significantly when switching on the EMI measurement system (figure 3.10 strip b). The same measurement procedure was repeated on a test site far away from buildings (figure 3.10 strip c). For measurement frequencies up to 15 kHz the noise level is between 10 and 20 nV/$\sqrt{\text{Hz}}$, which is even lower than in the shielded room for the frequencies smaller than 10 kHz. The noise

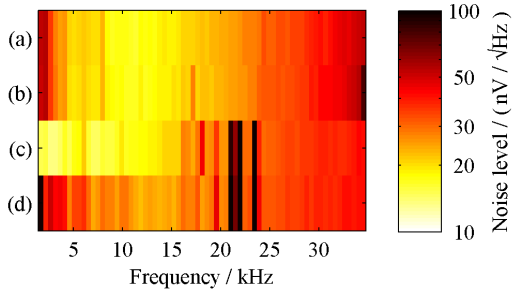

Figure 3.10.: Measurements with a sole receiver unit (see figure 3.5b) show the ambient noise spectrum in our electromagnetic shielded room when the EMI system is powered (a) off, and (b) on and at a test site when the system is switched (c) off , and (d) on.

level above 10 kHz is similar to that in the shielded room, except for some strong noise sources between 20 and 25 kHz. When the ElMa1 system is powered on (figure 3.10 strip d) some peaks occur in the region below 2 kHz and a rise of the general noise level between 2 and 15 kHz to about 25 nV/$\sqrt{\text{Hz}}$ is visible. Note that the EMI system was connected to a power generator for the measurement shown in figure 3.10 strip d and not to a filtered power line as shown in figure 3.10 strip b.

Because the measured noise level at the field site (figure 3.10 strip c) is lower compared to that in the shielded room (figure 3.10 strip a and b), it is clear that the resolution of the sensors is equal or better than the observed 15 to 40 nV/$\sqrt{\text{Hz}}$ in the frequency range between 5 and 30 kHz. This induced voltage is equivalent to a magnetic flux noise level of up to $2 \cdot 10^{-13}$ T/$\sqrt{\text{Hz}}$ between 10 and 30 kHz, which includes the EMI system noise. This noise is similar to the expected field noise from the literature, which is 10^{-13} T/$\sqrt{\text{Hz}}$. Based on these observations and estimations, the actual sensitivity of the sensors is expected to be better than the noise level at a field side, but not verified by measurements in a very low noise environment.

Furthermore, the experiment where the EMI system was powered by a generator (figure 3.10 strip d) exhibits a higher noise level of 30 nV/$\sqrt{\text{Hz}}$, which is more or less equal in the whole frequency range of interest. Considering that the experiment in the shielded room with a filtered power line shows a lower noise level, the power supply in the field was a significant source of noise. In addition, a few narrow-banded noise sources between 20 and 25 kHz were visible throughout the field experiments (e.g. figure 3.10 strip c and d). Those lines are

probably due to local external noise sources and the corresponding frequencies should not be used as measurement frequencies, here.

3.3.2. System Accuracy

Two experiments with different shunt resistors of 10 Ω and 100 Ω were compared by calculating the standard deviation (STD) of 17 measurements, each with a duration of 0.5 s and a Tx–Rx separation of 0.3 m. Using the transmitter current to normalize the measured receiver voltage like in (3.2) results in a worst-case-STD of 10 mS/m at 5 kHz when using the 10-Ohm shunt resistor, which is better than the expected accuracy of 13 mS/m. Furthermore, using the 100-Ohm resistor results in a STD of 2.5 mS/m. This means, that increasing the measured voltage drop at the shunt resistor decreases the overall noise and thereby increases the accuracy of the system. These results show that the dynamic range of the ADC was underestimated with $8.9{\cdot}10^4$, and its observed value is higher. In order to further increase the sensitivity of the system, the dynamic range of the ADC needs to be analyzed in more detail in future studies.

Extrapolating the observed instrumental accuracy from the first experimental results with a Tx–Rx separation of 0.3 m for the smaller RDR at the aimed Tx–Rx separation of 1.0 m using (2.4) and (3.4) suggests that the instrumental accuracy for $s = 1.0$ m matches the aim of 1 mS/m.

3.3.3. Temperature Drift

Measuring with sensor units in an isolated volume (see figure 3.8) with decreasing temperature yields a decreasing apparent conductivity (figure 3.11). Generally, the apparent conductivity value follows the ambient temperature. However, the drift of the signal shows a delay with respect to the ambient temperature because the copper coils heat up slower compared to the temperature sensor (figure 3.11, dashed red line).

The influence of each electrical coil parameter on the measured value is analyzed using the described SPICE model. Due to the delayed response of the coil temperature to the ambient temperature, the analysis is based on the data from between the intersection of the two temperature values (about 10 minutes after the start of the measurement) to the end of the measurement. The measured and the simulated apparent conductivity values for 8 kHz are

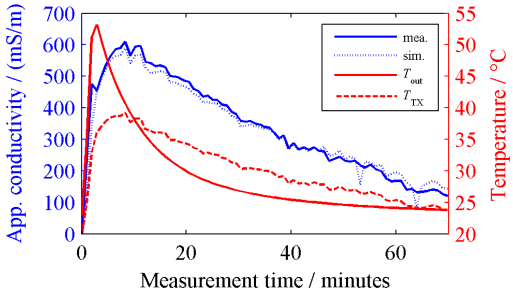

Figure 3.11.: A change in the ambient temperature (red line, T_{out}) around the sensor units cause a thermal drift in the measured apparent conductivity signal (blue line for 8 kHz). By measuring the impedance of the coils, the apparent conductivity drift is simulated for the same frequency (blue dotted line). The dashed red line shows the coil temperature of the transmitter (T_{Tx}), which is calculated from the measured coil resistance. The initial temperature is 22°C and the apparent conductivity value is zero at the starting time.

shown in figure 3.11 (solid and dashed blue line, respectively). The STD between measurement and simulation is 19 mS/m for the shown 8 kHz data set and smaller than 24 mS/m for the frequency range between 8 kHz and 33 kHz (not shown). Only the lowest used frequency of 3.3 kHz shows a larger deviation, which depends linearly on the temperature and is probably due to an unconsidered resistivity in the simulation. However, its influence becomes negligible for the higher frequencies. The overall temperature change in this region is 14.5 K. Due to the roughly linear relationship between the coil temperature (i.e. resistance) and the apparent conductivity values in figure 3.11, an average temperature drift of 39 mS/m/K at 8 kHz can be calculated. Because some parameters cause a negative and others a positive shift in the apparent conductivity values, the percentage of influence for all parameters is based on the sum of the absolute values of all single parameters, and is calculated exemplarily for a the frequency of 8 kHz (figure 3.12). Most drift effects in the result are due to the resistivity change in the transmitter coil of about 88.2 %. Second most important parameter is the transmitter inductance with an influence of 4.3 %, followed by the receiver inductance (1.4 %). The influence of the receiver resistance (0.4 %), the receiver capacitance (0.2 %), and the transmitter capacitance (< 0.1 %) is rather small. The remaining 5.6 % are due to other electrical components in the receiver circuit, such as e.g. the load resistance R_1 and the amplifier. The temperature dependency of those other components is based on temperature coefficients from the corresponding datasheets. Note, that the significance of each electrical

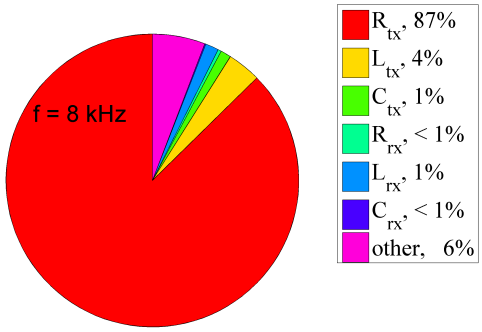

Figure 3.12.: The major source of drifts at a measurement frequency of 8 kHz is the transmitter resistance (R_{Tx}), followed by its inductance (L_{Tx}) and capacitance (C_{Tx}). The receiver properties R_{Rx}, L_{Rx} and C_{Rx} have a minor influence. Other components of the receiver system are influencing the result by 6 %.

component is strongly depending on the measurement frequency. Using the same measured impedances at different temperatures, the influence of each circuit element was simulated for frequencies of 5, 10, 15, 20, 25, and 30 kHz (figure 3.13). As the influence of the coil resistance on the impedance decreases with increasing frequency, the influence of the other components increase. Compared to the 8-kHz-data, the distribution of influences on the drift is changed significantly for the 30-kHz-data: The transmitter resistance (39 %) is nearly as important as the electrical components of the amplification circuit in the receiver unit (figure 3.13: "other", 35 %); in addition, the influence of the transmitter capacitance (7 %), the receiver inductance (8 %) and the receiver capacitance (7 %) is increased, while that of the transmitter inductance is decreased (2 %) and the influence of the receiver resistance is steady (2 %).

These results for a setup with a Tx–Rx separation of 0.3 m enable three observations: First, the temperature related drift is huge compared to the required stability to reach the aimed instrumental accuracy of 1 mS/m. This was expected as long as no temperature compensation is applied to the data. Next, the circuit simulation is able to reproduce the drift effects in the measured data with an accuracy that is depending on the accuracy of the current measurement, which enables the correction of drift effects up to the same accuracy. Finally, the major part of the drifts at 8 kHz is due to the transmitter system and in particular its resistivity, which might allow for skipping the additional drift measurements in the receiver

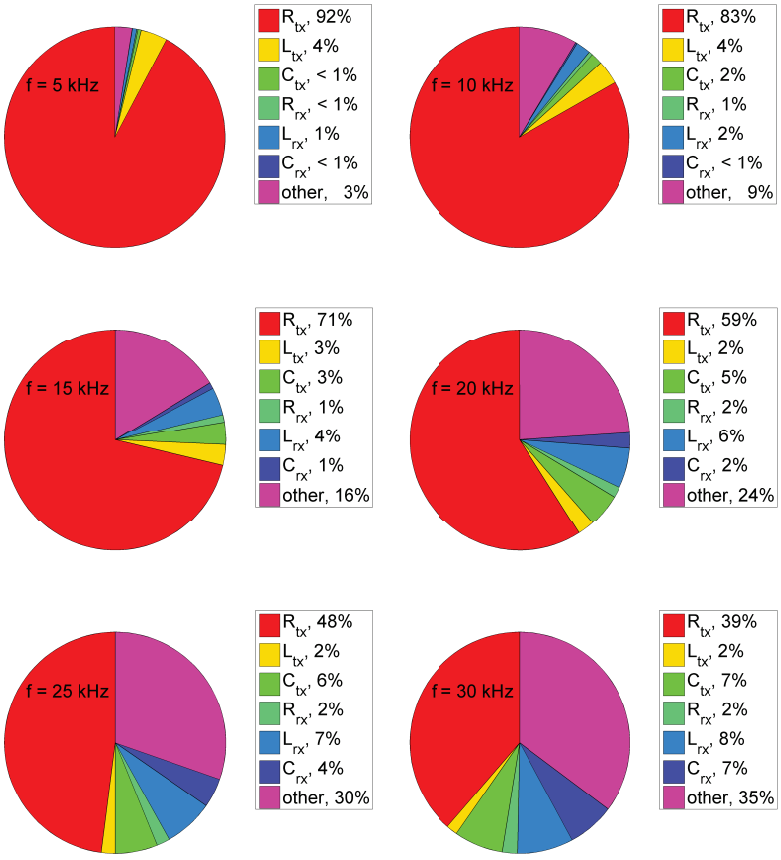

Figure 3.13.: The same analysis of the influence of certain electrical components as shown in figure 3.12 for the whole range of available frequencies, which are 5, 10, 15, 20, 25, and 30 kHz. Specified are the transmitter and receiver coil properties shown in figure 3.5. The label "other" combines the influence of the resistances in the receivers amplification circuit (R_1,R_2, and R_3).

coils and performing a temperature compensation based on the transmitter drift only, which is implicitly done by using the transfer impedance (3.2) for the post-processing. Moreover, for some observations and stable temperature conditions it might be sufficient to just measure the electrical parameters of the receiver at every few measurement points, and not for every single point, to reduce the survey time. However, for the analyzed setup with a temperature change of about 15 K in the coils, even 1 % of the overall drift in the apparent conductivity value would result in a significant error of 5 mS/m in the measurement value at 8 kHz and for a Tx–Rx separation of 0.3 m.

3.3.4. Influence of Coil Shielding

Using a shielded and an unshielded sensor, exhibits the influence and importance of the shielding for an EMI instrument. Figure 3.14 shows the difference in the mean values from the air calibration and the soil measurement, ordered in five frequency groups. Each group consists of the data from the four combinations of transmitters and receivers: First, a shielded transmitter and receiver (blue), second, a shielded transmitter and an unshielded receiver (green), third, an unshielded transmitter and a shielded receiver (red), and fourth, an unshielded transmitter and receiver. All combinations show different results. Most obviously, the unshielded receivers resulted in the worst measurements. Using such a sensor in combination with a shielded transmitter results in a negative and strongly decreasing apparent conductivity value with increasing frequency, being about -5 mS/m at 5 kHz and -90 mS/m at 30 kHz. Using this sensor with an unshielded transmitter results in a major skip in the measured apparent conductivity when moving the system from the air to the soil. In addition, the apparent conductivity value is slightly correlated to the measurement frequency, starting with about 200 mS/m at 5 kHz and reaching 220 mS/m at 30 kHz. This experiment proves that there is a capacitive coupling between the coils and the soil. In addition, when using unshielded transmitter and receiver units, there is probably a strong capacitive coupling between the two coils directly.

Much better results are achieved for shielded receiver coils, either in combination with a shielded or an unshielded transmitter. Both measurements show rather stable apparent electrical conductivity (σ_a) values of about 20 mS/m for measurement frequencies between 5 and 20 kHz, with more noise at 5 kHz, which is due to the weaker sensitivity. The 30-kHz measurement shows an apparent conductivity of only 10 mS/m, which is lower than the true

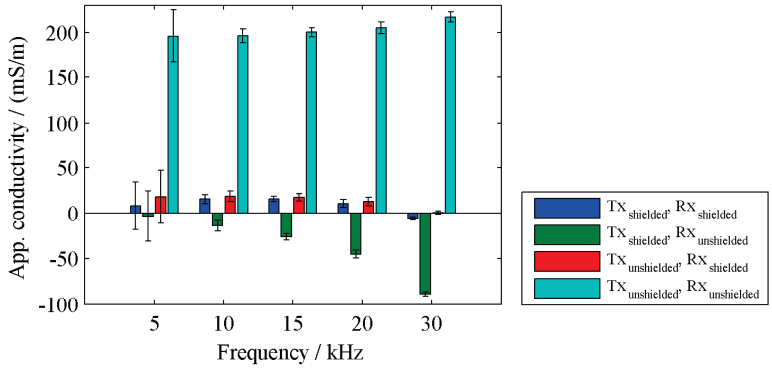

Figure 3.14.: The data from shielded and unshielded coils exhibit the capacitive effects that occur, when bringing the instrument from the air (approx. 2 m high) to the surface of a soil with an apparent conductivity of approx. 18 mS/m (measured with a CMD-MiniExplorer a few weeks earlier on the same spot). The bars show different combinations of unshielded and shielded transmitter (Tx) and receiver (Rx) coils in five groups of different measurement frequencies (f).

apparent conductivity, though the standard deviation (STD) of the 19 measurements implies a rather accurate measurement. This means, that the measurement itself is rather accurate, but there is some systematic error for this higher frequency.

3.3.5. Field Measurement

Shifting the sensors between a calibration rack and a test object of known homogeneous electrical conductivity (σ) enables an analysis of the accuracy and the stability of the system under realistic field conditions without drift correction. First, apparent conductivity data is calibrated to the mean apparent conductivity of the measurements on the calibration rack (figure 3.15). The result shows a clearly visible increase of the measured apparent conductivity, when moving the sensor above the pool. It is also visible that the apparent conductivity values from the second calibration measurement are slightly smaller compared to the first three measurements. In addition, a dependency between frequency and measured apparent conductivity was observed. This becomes more visible by plotting the calibrated mean apparent conductivity values from above the pool as function of the frequency (figure 3.16). The apparent conductivity value decreases from about 50 mS/m at 5 kHz, which is roughly the conductivity of the pool water, to about 30 mS/m at 30 kHz.

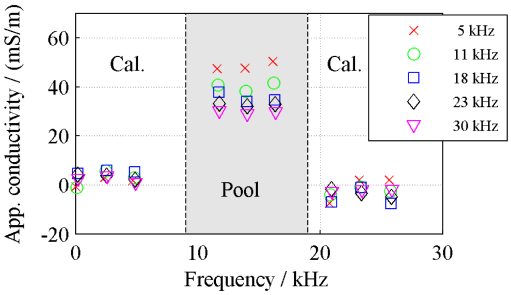

Figure 3.15.: The plot shows measured apparent conductivity over time for five selected measurement frequencies. The first three measurements are from the calibration rack (cal.), which is shown in figure 3.9. The next three measurements are from above the water-filled pool, and the last three are from the calibration rack, again. The pool-measurement shows a clearly higher conductivity, than the calibration in air. Above the pool, the apparent conductivity values show an unexpected frequency dependency, which is analyzed in detail in figure 3.16. Furthermore, the second calibration measurements after about 20 minutes show a slightly lower apparent conductivity than the first.

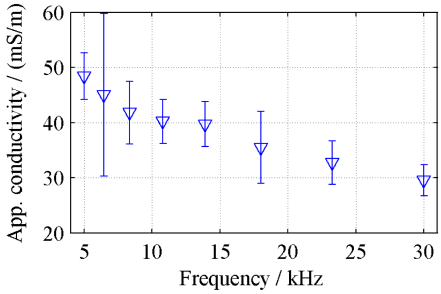

Figure 3.16.: Calibrated apparent conductivity data from above the swimming pool (figure 3.9 and 3.15) and for Tx–Rx separations (s) of 0.3 m show an unexpected decrease with increasing measurement frequency. The vertical bars show the STD of the shown mean apparent conductivity value. The 6-kHz measurement shows a larger variation, which indicates an external noise source at this frequency.

In general, it is obvious from the experiment description, that the pool is still too small to be considered as a homogeneous volume, even for the used Tx–Rx separation of 0.3 meters. Furthermore, the air gap in between the sensors and the water surface decreases the expected apparent conductivity value from 50 mS/m to about 41 mS/m, which is estimated using the forward model from chapter 2. The STD of the mean values is between 3 and 4 mS/m, except for 7 mS/m at 18 kHz and 15 mS/m at 6 kHz. This is close to the measured system accuracy of 2 mS/m in the shielded room (R_s = 100 Ω). The larger noise level at 6 and 18 kHz might be due to ambient noise or system noise due to the unfiltered power supply of the measurement system. Furthermore, the stable but lower apparent conductivity value from the second calibration compared to the first might be caused by a slightly different positioning of the sensor bar on the calibration rack. Finally, the descending apparent conductivity values for increasing measurement frequencies are not understood yet, and need to be investigated in further studies. Nevertheless, the experiment shows that the system is clearly responding to a volume with an electrical conductivity within the range of geophysical applications. Furthermore, the achieved accuracy matches the expected values and suggest that the instrumental accuracy for s = 1.0 m is at least 1 mS/m.

3.4. Conclusions

The presented electromagnetic induction (EMI) measurement system consists of modular sensor units for transmitters and receivers. These receivers can be placed by the operator at any Tx–Rx separation (s), though the instrument is optimized for s=1.0 m and its instrumental σ_a-accuracy decreases for other Tx–Rx separations. The sensor units only differ in the included coils and the adjustment of its amplification circuit. In order to reduce parasitic capacitive effects between the coils among themselves, and between the coils and the ground, the Rx coils need to be shielded. Shielding the Tx coil does not influence the measurement in a positive or negative way. Nevertheless, to avoid parasitic effects when using a Tx coil in Rx mode, all coils were shielded in the same way using a toroidally wound aluminum tape (see section 3.2.3). Note that, even with the shielded receiver coils, a systematic offset was observed in the apparent conductivity data for the highest frequency of 30 kHz, which needs to be analyzed in future studies.

The system is optimized for a measurement frequency range from 5 to 30 kHz which enables

adjusting the measurement frequencies away from the site-specific electromagnetic noise, and, thereby, avoiding measurements at noisy frequencies such as observed in figure 3.10 strip (c) and strip (d) between 20 and 25 kHz. The actual sensitivity of the system is limited by the dynamic range of the used analog-to-digital converters (ADC's). This was observed by measurements with different shunt resistors (R_s), i.e. different signal amplitudes for the current measurement, which result in a visible difference in the signal noise. Using a 10-Ohm resistor results in an equivalent σ_a-noise of 10 mS/m at 5 kHz for a Tx–Rx separation of 0.3 m and a measurement rate of 2 Hz, while measurements with a 100-Ohm resistor show a noise level of 2.5 mS/m. The required dynamic range (RDR) for measuring the primary and the secondary fields without any compensation decreases quadratically with the Tx–Rx separation, and, hence, the aimed instrumental accuracy of 1 mS/m at $s = 1.0$ m and a measurement rate of 2 Hz is expected to be reached by the system, even for measurements with the 10-Ohm shunt resistor. Next, measuring the sensor impedance allows to analyze and simulate the drift of the sensors and to correct it in the post-processing. Most of the thermal drift at 8 kHz is due to the transmitter properties (93 %) and in particular its resistance (88 %). Note that the transmitter impedance is implicitly observed during apparent conductivity measurements by measuring the transmitter current and the generator voltage. First results for a Tx–Rx separation of 0.3 m show that the observed accuracy of the full temperature drift correction of both coils is better than 30 mS/m for a temperature stress of approximately 0.5 K/minute. The accuracy of this drift correction is limited by the accuracy of the current measurement at both corresponding coils.

Finally, a sensitivity test under field conditions shows that the sensor is able to detect a water filled swimming pool with a conductivity of 50 mS/m. An observed frequency dependency of the response from this pool measurement needs to be analyzed in future studies.

4. Field-Optimization and Validation of a Novel Multi-Channel Electromagnetic Induction System[1]

Based on the experience with the ElMa1 system, which is described in the previous chapter, here, a novel multi-channel measurement system ElMa2 is setup, which has the potential for improving the depth-resolution of electromagnetic induction (EMI) surveys. Besides the optimization of the system in terms of measurement accuracy and regarding the observed limitations of ElMa1, the system is optimized for remote outdoor applications and consists of a portable system unit, including the signal electronics, the sensor control and the power supply, a laptop computer which is used as user interface and data storage system, and nine modular EMI sensor units. The instrument is optimized for shallow applications, and, in particular, is designed to reach an instrumental σ_a-accuracy of 1 mS/m for variable Tx–Rx separations between 0.5 and 1.0 m and a measurement time per point of 0.5 s. Different multi-frequency excitation signals with measurement frequencies from 5 to 30 kHz were analyzed, resulting in the most efficient excitation method being a successive measurement with single-frequency sinusoidal signals using the maximum voltage provided by the used generator (5 Vp). The system was tested along a well-known transect on a field-site of the research center using inverted ERT data from selected locations to calibrate the EMI data. The post-calibrated data were inverted and compared to reference EMI data from an earlier survey with a commercial EMI instrument. The results show, that the system is capable of providing a comparable accuracy in the inverted data, though the used inversion algorithm only resolves up to two or three layers, respectively, and needs to be improved to analyze the resolution of the novel customizable sensor-array EMI instrument.

[1] adapted from Mester et al. (in prep.).

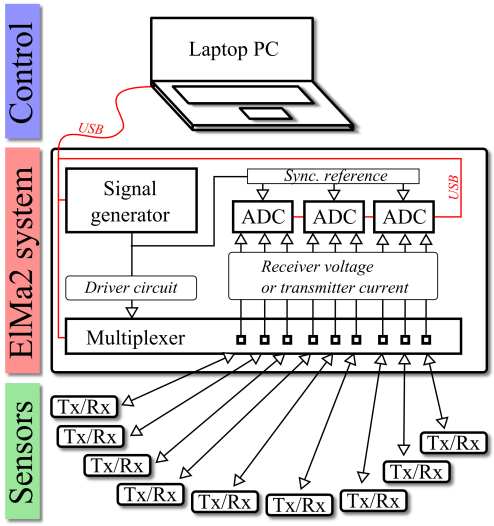

Figure 4.1.: The new ElMa2 measurement system is controlled via universal serial bus (USB) by a laptop personal computer (PC). The system consists of a signal generator, a multiplexer and three independent analog-to-digital converter (ADC) units, each with four input channels. Up to nine EMI (Tx/Rx) sensors can be connected to the multiplexer unit.

4.1. Setup and Optimization

In the following, the advancements of the new system, which is called ElMa2, are described and compared to the previous system from chapter 3. Instrumental improvements affect the measurement system, the receiver (Rx) circuit and the transmitter (Tx) circuit, respectively.

4.1.1. The ElMa2 System

The ElMa2 measurement system is designed to be flexible in connecting Tx and Rx units with Tx–Rx separations (s) between 0.4 m and 2.0 m and to include a sufficient amount of sensor channels while being portable in terms of size and weight. The system basically consists of the three components shown in figure 4.1: A laptop PC which is used to control the system and to store the data over the USB 2.0; the ElMa2 system unit which includes a signal generator, a multiplexer unit and the ADC units which are all connected to an USB hub; and the up to nine sensor units (Tx and Rx units) which are connected to the multiplexer in the ElMa2 system using an individual cable for each sensor. In addition to the components shown in

figure 4.1, an external temperature sensor can be connected to the system in order to store temperature data for each measurement point.

All components are battery powered: The laptop computer is powered using replaceable Li-Ion batteries and the ElMa2 system includes a standard 12-Volt-$LiFePO_4$-battery[2] with 10 Ah, which supplies power for more than four hours of measurement time for the system unit and all sensors.

The signal generator provides sinusoidal and arbitrary signals with amplitudes up to 5 Vp and an output impedance of 50 Ω. In order to achieve a maximum current through the Tx coils, a video-line driver is connected to the output of the generator, which reduces its effective output impedance before the signal is feed into the multiplexer and, finally, into the selected Tx unit.

The data acquisition is performed using three state-of-the-art 24-bit USB ADC units. Each of those units has four input channels, which are sampled synchronously and synchronized precisely. The large dynamic range is essential for the measurement since the required dynamic range (RDR) is the ratio between the secondary magnetic field strength (H_s^*) and the roughly six orders of magnitude larger primary magnetic field strength (H_p^*).

More details about the introduced hardware components can be found in chapter A.2.

During the post-processing, the measured signals are filtered and translated into complex voltages using the lock-in technique. Therefore, a synthetic sinusoidal signal ($\vec{s}$),

$$\vec{s} = \exp\left(i\omega\vec{t}\right), \tag{4.1}$$

is computed, where the discrete time vector $\vec{t}$ corresponds to the sampling rate and the sampling time of the measured signal $\vec{m}$ and thus has the same length n. The synthetic signal is scalar multiplied with the measured signal to derive the complex peak voltage (U_p^*),

$$U_p^* = 2\frac{\vec{s}\cdot\vec{m}}{n}, \tag{4.2}$$

for the given angular frequency (ω) and n samples. In order to synchronize the three independent ADC units on a common time base, the first channel of each unit is connected to the signal generator (figure 4.1). In the post-processing, the phase angles between the first

[2] Vision Lithium Iron Phosphate Battery; Shenzhan Center Power Tech. Co. Ltd.; Shenzhen, China.

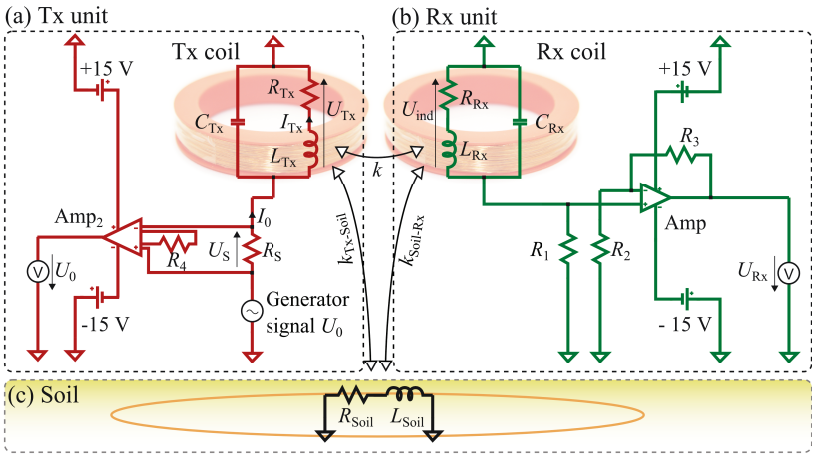

Figure 4.2.: Each sensor unit contains (a) a Tx-circuit (red circuit diagram) and (b) a Rx-circuit (green circuit diagram). During an EMI measurement, the Tx-unit creates an alternating electromagnetic field, which is coupled into the Rx-unit directly (k) and, additionally, coupled into the Rx-unit through the ground ($k_{\text{Tx-soil}} + k_{\text{soil-Rx}}$), which is represented by (c) the "soil"-circuit (black circuit diagram).

channel of the first ADC unit and the first channels of all other ADC units are derived and used to synchronize the corresponding channels of each unit, respectively. For example, the phase information of channel one of the first ADC unit is defined as the reference and its difference compared to channel one of the third ADC unit is used as correction angle for all other channels of the third ADC unit.

4.1.2. Receiver Optimization

The Rx-design from chapter 3 is optimized for a measurement frequency (f) range between 5 kHz and 30 kHz. In order to allow for larger Tx–Rx separations compared to the system described in chapter 3, a faster amplifier is used which enables greater signal amplifications for an unchanged signal bandwidth. The noise level of the improved receiver is dominated by the input voltage noise of the amplifier (U_{na}), which is 7 nV/$\sqrt{\text{Hz}}$, while the input current noise of the amplifier (I_{na}) is 0.6 fA/$\sqrt{\text{Hz}}$ and the thermal noise voltage level (U_{nt}) of the coil (1 nV/$\sqrt{\text{Hz}}$) is negligible. The resulting receiver noise level is smaller compared to the expected noise level from the induced magnetic ambient noise in the field, which is approximately 9 nV/$\sqrt{\text{Hz}}$ (see chapter 3). More details about the improvements in the sensor unit design are given in chapter A.4.

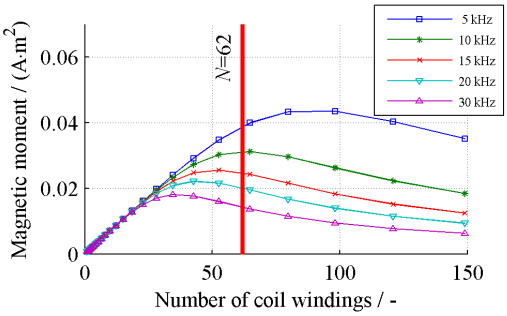

Figure 4.3.: The magnetic moment of the Tx-coil is calculated as function of the coil windings using (3.9) for five measurement frequencies between 5 and 30 kHz, and a shunt resistor (R_s) of 20 Ω. A transmitter coil with 62 windings was chosen since an optimum magnetic moment for all frequencies was obtained whereby also the rated power of the shunt resistor was taken into account.

4.1.3. Transmitter Design

The Tx-unit is designed to generate a maximal magnetic field within the specifications of the system components and to enable high-precision impedance measurement at the Tx-coil. The latter is necessary to correct for drift effects due to changes in the coil impedance during a measurement. Compared to the system presented in chapter 3, the current measurement was improved by placing the shunt resistor on the sensor board and measuring the voltage drop along it using an instrumental amplifier (Amp_2 in figure 4.2) inside the sensor unit (see chapter A.4). The improved design allows adjusting the signal amplitude to the input range of the ADC and using a single channel for the current measurement, thus reducing the needed number of ADC channels compared to the system described in chapter 3.

In order to increase the transmission power of the transmitter compared to ElMa1, the generator signal is fed into a driver, which reduces the output impedance from 50 Ω at the generator to about 7 Ω (not shown in figure 4.3). Considering the new output impedance, a transmitter coil with 62 windings and a shunt resistor with 20 Ω is ideal for transmitting in the measurement frequency range between 5 and 30 kHz, resulting in a magnetic moment (m) of 25 $\text{mA} \cdot \text{m}^2$ at 15 kHz (figure 4.3). The maximum voltage drop at the shunt resistor is 3.0 V, which occurs at 5 kHz. Using a gain of two at the amplifier, the voltage at its output is between 1.7 and 6.0 V for measurement frequencies between 30 and 5 kHz, respectively. The power dissipation at the shunt resistor, which is also an optimization criterion, is smaller than 0.3 W, which is inside its specifications (< 0.6 W).

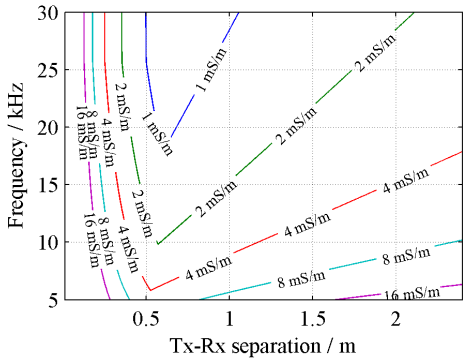

Figure 4.4.: Instrumental σ_a-accuracy for considered combinations of Tx–Rx separations and measurement frequencies. The lines indicate configurations of equal σ_a-accuracy for a measurement rate of 2 Hz and a signal voltage of 5 Vp. For example, for Tx–Rx separations between 0.5 and 1.0 m and a measurement frequency of 30 kHz a resolution of better than 1 mS/m is achieved.

4.1.4. Instrumental Accuracy

The instrumental accuracy of the measurement system is estimated for specific measurement configurations by considering all known limitations and translating them into apparent electrical conductivity (σ_a) values (figure 4.4). Starting from the Tx–Rx separation for which the instrument is optimized, the limiting factors can be separated in those which limit the accuracy for smaller Tx–Rx separations and for larger Tx–Rx separations, respectively.

For the smaller Tx–Rx separations, the dynamic range of the used ADC, which is specified with $8.9 \cdot 10^4$ at 100 kSamples/s, limits the accuracy of magnetic field measurement at the Rx-unit. In order to translate this limit into an instrumental σ_a-accuracy, the dynamic range is inserted into the low-induction number (LIN) approximation (equation 2.4) from McNeill (1980) as the ratio between the primary and the secondary magnetic field strength. Since the current measurement at the transmitter unit is used to normalize the received signal (equation 3.2), the RDR needed for the current measurement is the same as for the receiver signal. Using the voltage drop at the shunt resistor and dividing it by the estimated voltage noise level of the transmitter unit, a second dynamic range limit is derived which is converted into an instrumental σ_a-accuracy limit as before. Moreover, experimental results showed that there is a reproducible phase resolution limit of about 5 µrad in the current measurement at the Tx-unit, which is converted into a limiting voltage level of approximately $5 \cdot 10^{-6} \cdot U_0$.

For the larger Tx–Rx separations, the instrumental σ_a-accuracy is limited due to the ambient magnetic noise level (B_{noise}) in the field in combination with the magnetic moment of the Tx-unit. In general, the ambient magnetic noise level decreases with the reciprocal of the frequency (Fuellekrug and Fraser-Smith 2011) while it is independent from the chosen Tx–Rx separation. However, the primary magnetic flux through the Rx unit decreases with its separation from the transmitter, dropping below the noise level at a certain Tx–Rx separation for which it limits the instrumental σ_a-accuracy of the system. Experimental results from the ElMa2 system showed an induced voltage ($U_{\text{ind.}}$) due to the ambient magnetic noise that is smaller than 30 nV over the frequency range from 5 to 30 kHz. This voltage noise is translated into a limiting magnetic flux using (3.10) which is converted into a magnetic field strength and inserted into the LIN approximation as the smallest measurable secondary magnetic field strength together with the dipole approximation for the primary magnetic field strength, resulting in another limiting σ_{a}-accuracy value.

Figure 4.4 shows that the system is optimized for small Tx–Rx separations between 0.5 and 1.0 m, reaching an instrumental σ_a-accuracy of better than 1 mS/m at 30 kHz. For Tx–Rx separations of 0.4 and 2.0 m, the accuracy decreases to about 2 mS/m (30 kHz) as well as it decreases for the lower measurement frequencies, being about 4 mS/m for the same Tx–Rx separations at 15 kHz and between 13 and 18 mS/m at 5 kHz. Note that these estimations are worst-case scenarios and the measured induced voltage from the ambient magnetic noise level was even less than 30 nV for the higher frequencies as well as the underlying dynamic range value of the ADC is the guarantied value from the manufacturer.

4.2. Pre-Measurements and General Methods

4.2.1. Transmitter Signal

Multiple measurement frequencies are used to measure the impedance of the transmitter coil, which enables the simulation of its drift (see chapter 3), and to be flexible in terms of narrow-banded ambient noise sources on a field site. In order to find the most suitable excitation mode in terms of sensitivity and drift performance, three kinds of excitation signals with multiple measurement frequencies are analyzed in detail (figure 4.5 and table 4.1): A “slow sequential” signal (a), a “super-positioned” waveform (b) and a “fast sequential” waveform (c). The measurement time (t_0) is chosen in the control software and its meaning depends

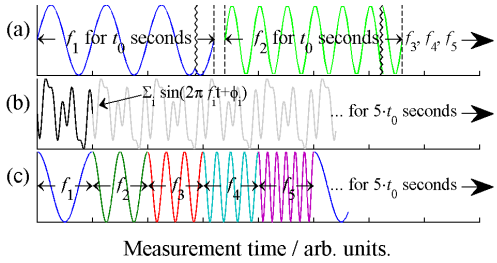

Figure 4.5.: Three kinds of excitation signals are considered: A "slow sequential" (a), a "super-positioned" (b) and a "fast sequential" signal (c), each containing five measurement frequencies. The selected measurement time (t_0) includes all measurement frequencies for signals (b) and (c), and only one frequency for (a).

on the selected excitation signal type and is explained in the following. For all methods, the measurement time needs to be an integer multiple of the shortest period of the signal such that only complete periods are recorded, which is important for the use of the lock-in technique in the post-processing.

Table 4.1.: Characteristics of the three considered shapes of excitation signals shown in figure 4.5.

Type of signal	Slow sequential	Super-positioned	Fast sequential
Amplitude per frequency and RDR	+	−	+
Drift susceptibility (electrical load)	−	+	∘
Flexibility in choice of frequencies	free	common divisor	free
effective voltage ($U_{\text{effective}}$)	$0.71 \cdot U_{\text{peak}}$	$0.60 \cdot U_{\text{peak}}$ (for five frequencies)	$0.71 \cdot U_{\text{peak}}$

For the "slow sequential" signal, the generator is switched to a specific frequency and the measurement is started after a user-defined pause. After t_0 seconds, the data acquisition is stopped, the data stored, and the generator is switched to the next frequencies successively. If not stated explicitly, the generator is used with its maximum output voltage (5 Vp) to achieve the maximum field strength.

The second method is based on the super-position of sinusoidal signals of different frequencies. In order to generate a continuous signal, the greatest common divisor (GCD) of the selected frequencies determines the length of the waveform, which is $1/\text{GCD}(f)$ seconds. This ensures

that no skips occur due to the repetition of waveform by the generator. Here, measurement frequencies of 5, 10, 15, 20, and 30 kHz are used, resulting in a GCD of 5 kHz and, consequently, a waveform length of 0.2 ms (figure 4.5, strip b, dark black curve). A limitation of this method is the maximum amplitude of the signal, which is given by the used generator and split up to all included measurement frequencies, resulting in an increased RDR of the ADC. On the contrary, the measurement time includes measurements at all selected measurement frequency at the same time, compared to only one frequency for the "slow sequential" signal. The overall noise level for the same measurement time depends on the effective voltage of the signal (table 4.1), as long as the dynamic range of the ADC does not limit the accuracy.

The third method uses a waveform, where all sinusoidal time series are put together at the point of slowest amplitude change (i.e. its maximum). In order to have the same measurement time for each measurement frequency, the waveform for n frequencies is $n/\mathrm{GCD}(f)$ long. The advantage compared to the second method is the increased signal voltage per frequency, and the difference compared to the "slow sequential" signal is that the multiple frequencies are swapped with the rate given by $\mathrm{GCD}(f)$ which results in a more uniform load of the system. Note that, in contrast to the other methods, the slope of the waveform is not continuous, resulting in a more complex frequency spectrum. In order to acquire data for the same measurement duration per frequency as with the other methods, this "fast sequential" waveform can be repeated for n times.

Those three excitation methods are different regarding the load of the electronic components, i.e. heat-up and drift effects, and regarding the operational mode of the signal generator. Method 2 and 3 make use of the arbitrary waveform feature of the generator, which means that the signal shape is designed on a PC, uploaded to the device and then continuously emitted from it. In contrast, the "slow sequential" signal is excited using the sinusoidal signal mode of the generator. In terms of drift effects, the "super-positioned" waveform is considered to be the most robust signal, because the load of the system does not change over the entire measurement, as long as the transmitter coil is not switched. The opposite extreme is the "slow sequential" signal, where the full output voltage of the generator is used for each single measurement frequency, and the system load is changed from frequency to frequency. A compromise between both approaches is the "fast sequential" waveform, where the generator repeats the same waveform for the whole measurement time, though the frequency changes with a rate of the GCD of the selected measurement frequencies.

A related issue is that warm-up effects strongly influence the measurements if the transmitter is switched during a survey, allowing an acclimated transmitter system to cool down in between of measurements and to heat-up once more when measuring again.

All three methods are analyzed using measurement frequencies of 5, 10, 15, 20, and 30 kHz and the results are summarized in table 4.2. The output level of the generator is adjusted to its maximum (5 Vp), except for a 1.5-Vp measurement with the "slow sequential" signal. The measurement time is $t_0 = 0.5$ s per frequency for the "slow sequential" signal and the "fast sequential" waveform, and 5×0.5 s for all frequencies for the "super-positioned" waveform. For each method, 40 repetitions are measured with the instrument standing still on the ground. Considering a time factor of about three for the data acquisition, the overall measurement time per method is approximately five minutes. In order to distinguish a possible accuracy limit due to the dynamic range of the ADC, measurements are performed with Tx–Rx separations of 0.4 and 1.2 m using signal amplifications of 121 (figure 4.2, $R_2 = 91\ \Omega$ and $R_3 = 1$ kΩ) and 3982 ($R_2 = 2.7\ \Omega$ and $R_3 = 1$ kΩ), respectively. The drift values in table 4.2 are derived from a linear regression, which is fitted to the 40 repetitive measurements for each method, respectively, and represents the observed drift well. The given noise values in table 4.2 are standard deviations in the measurement signal after subtraction of the linear drift.

Table 4.2.: The three considered types of excitation signals (figure 4.5, table 4.1) are investigated for a lock-in frequency of 15 kHz, measurement frequencies of 5, 10, 15, 20, and 30 kHz and a measurement time of approximately five minutes. Note that the instrument was not moved during the measurements.

Type of signal	Slow sequential		Super-positioned	Fast sequential
Set U_{peak} / V	1.5	5.0	5.0	5.0
Drift for $s = 0.4$ / 1.2 m / (mS/m/minute)	-0.8 / 0.2	-0.8 / 0.2	0.7 / 0.4	2.0 / 0.5
Noise for $s = 0.4$ / 1.2 m / (mS/m)	1.7 / 1.9	1.3 / 0.8	9.0 / 0.9	19.6 / 2.7

The drift is most stable over different Tx–Rx separations for the "super-positioned" waveform, being between 0.4 and 0.7 mS/m per minute. For the "slow sequential" signal, it depends on the Tx–Rx separation, being constant over separate measurements with 1.5-Vp and 5.0-Vp

signals. The worst drift effects were observed for the "fast sequential" waveform, being up to 2 mS/m per minute for a Tx–Rx separation of 0.4 m (table 4.2).

The analysis of the signal noise allows differentiating between two noise sources: A RDR-dependent component and a transmitter-power dependent component (left and right part in figure 4.4, respectively).

The latter is related to the effective signal voltage (see table 4.1) and the ambient noise level, and explains the 1.2-m values in table 4.2, where the RDR of the signal is considered to be inside the ADC's specification and the signal amplitude is above the ambient noise level (compare figure 4.4). This noise component can be estimated numerically by adding a normal distributed noise to a synthetic signal and performing the lock-in procedure. The results show the smallest noise level for the "slow sequential" signal and a 1.16 times larger noise level for the "super-positioned" waveform, which is in good agreement with the 1.2-m measurement shown in table 4.2 and can therefore be explained by the 1.18 times smaller effective voltage of the signal (see table 4.1). The same simulation gives a factor of 1.83 between the "slow sequential" signal and the "fast sequential" waveform, which is underestimating the noise observed by the measurement. Considering the ElMa2 system, this noise source limits the instrumental σ_a-accuracy for Tx–Rx separations of more than 1.0 m and increases linearly with the Tx–Rx separation (figure 4.4).

The second source of noise is due to the RDR, which increases quadratically with decreasing Tx–Rx separation (chapter 3). Therefore, this noise component limits the instrumental σ_a-accuracy for Tx–Rx separations smaller than about 1.0 m, which is visible in the measurement data for the 0.4-m Tx–Rx separation in combination with all three excitation methods (table 4.2). The smallest noise level was observed for the "slow sequential" signal with $U_{\mathrm{peak}} = 5\ V$, whereas the "super-positioned" waveform shows a seven times larger standard deviation (STD) for the same Tx–Rx separation. This cannot be explained by the factor 1.16, which was derived above. It is also not caused by the smaller amplitude of the processed frequency component, which is 1.8 Vp and still larger compared to the 1.5 Vp of the "slow sequential" signal. The "fast sequential" waveform shows an even larger noise level. Due to the RDR-related noise source, the instrumental σ_a-accuracy decreases more than linearly with decreasing Tx–Rx separation (figure 4.4), which is a major issue when optimizing the instrument for small Tx–Rx separation, and needs to be analyzed in future studies. For the

following experiments, the "slow sequential" signal was used.

4.2.2. Constructional Limitations

Conductive objects in the sensitive region of an EMI device influence the measurements. Therefore, the amount of conductive material (and in particular metal) in the vicinity of the sensors should be minimized or at least must stay fixed relative to the sensors in order to allow for a calibration of the system. This kind of disturbing material includes the components of the measurement system itself and, therefore, all sensor units are mounted on a non-conductive plastic construction. However, the sensors itself contain metal due to the copper-wire coils, the printed circuit boards and their connection cables and need to be mounted as rigid as possible. Nevertheless, these components may influence the instrumental σ_a-accuracy due to mechanical deformation of the construction, i.e. displacement of the sensors and cables, during a measurement.

A pre-experiment was performed to measure effects due to worst-case scenarios in terms of (I) cable displacement and (II) sensor movement. In order to create realistic conditions, the sensor units are attached to the mounting system which is intended for the use in the final field-setup. This construction kit has visible mechanical tolerance at all connections. Therefore, the first test was to measure before and after manually changing the position of the wiring. The second issue was analyzed by manually deforming the construction.

The test measurement was performed with a Tx–Rx separation of 0.4 m and a sampling time of 0.5 s, using the "slow sequential" signal and doing three repetitions for each configuration. The results for 15 kHz show that changing the cable position between the sensors by approximately 2 cm to one side affects the measurement signal by 8 mS/m. Moving the cable back to its original position reverses this effect. Next, the Tx-unit is pushed to one side without removing it from its mount. Measuring with the same measurement settings as earlier, but pushing the sensor back and forth resulted in a distortion of the apparent conductivity value of 6 mS/m.

An outlier during a survey may therefore be caused by a local deformation of the prototype sledge, resulting in a displacement of a sensor and/or a cable during a survey. Assuming that both effects superimpose in a worst-case scenario, deviations of about 14 mS/m may occur from time to time after moving the setup in between of measurements, which is accepted

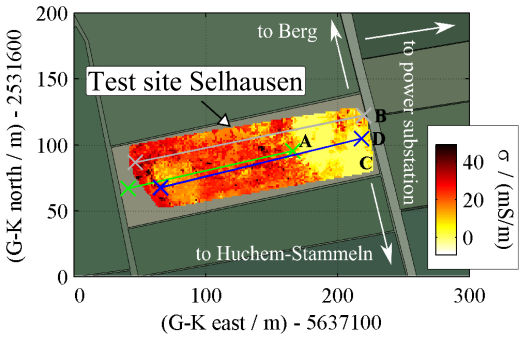

Figure 4.6.: The test site Selhausen is indicated on the Gauss-Krüger reference grid by the light brown rectangular, which is superimposed by (C) a slice at 0.7-m depth through a 3D electrical conductivity (σ) data set that was obtained from an 2012-EMI -survey by von Hebel et al. (2014). Former EMI transects from the years (A) 2009, (B) 2010, as well as (D) the new ElMa2 transect are marked. The site is surrounded by actively cultivated fields (dark green).

for this first prototype setup. Note that the magnitude of this distortion depends on the setup and, in particular, on the amount of conductive material in the vicinity of the sensor units. Consequently, the deviation increases if more sensor units and cables are attached. Because the control and data acquisition system would also disturb the measurement it is always placed as far as possible away from the sensor units.

4.2.3. Field Measurements

The novel EMI system ElMa2 was tested on a transect of 158-meter length at the same test site (Selhausen) (figure 4.6) where the data were measured which were used to evaluate the inversion described in chapter 2. The closest anthropogenic construction is a power substation, which is about 200 m east of the test site. The next villages are about 1 km away. Electromagnetic induction measurements have been performed on the test site before, and the measurements performed in 2009 (A), 2010 (B), 2012 (C) are marked in figure 4.6 and are discussed in detail in Lavoue et al. (2010), Busch (2013) and von Hebel et al. (2014), respectively. The transect marked with the letter 'D' in figure 4.6 was measured with ElMa2 and is analyzed in the following. The transect location was chosen based on the data from the previous measurements in order to cover various soil conductivity distributions over depth.

Nine sensor units, one transmitter and eight receivers, are attached to a sledge-like tube

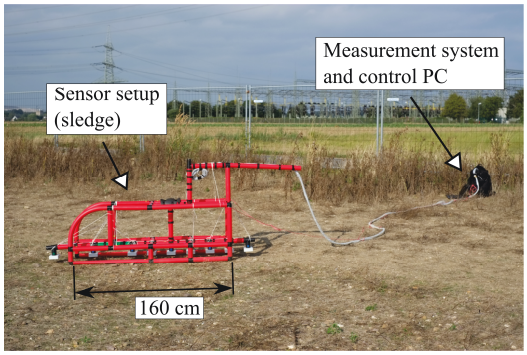

Figure 4.7.: The sensors are mounted on a Quadro construction kit. The depicted setup has Tx–Rx separations of 0.4 (twice), 0.6, 0.8, 1.0, 1.2, 1.4 and 1.6 m with a vertical dipole arrangement. The data acquisition and measurement control system is moved in front of the system, approximately seven meter away from the sensors.

construction, which is made out of plastic (figure 4.7). All sensors are mounted as horizontal coplanar loops (HCP) with Tx–Rx separations of 0.4 (twice), 0.6, 0.8, 1.0, 1.2, 1.4 and 1.6 m. The sensor-cables are carefully fixed to the tubes, bundled in the center and led up to the top and then to the back of the construction in approximately 80 cm height above the sensors, before the cable bundle is guided away from the sensors to the measurement system (figure 4.7).

The system was moved stepwise along the transect with measurements every meter, measuring each point for two seconds using the discussed slow sequential excitation signal with an amplitude of 1.5 Vp. The same transect was also measured with a CMD-MiniExplorer, which has Tx–Rx separations of 0.3, 0.7 and 1.2 m, and allows a faster data acquisition/measurement (< 1 s per point).

In order to calibrate the EMI data (from ElMa2 and CMD-MiniExplorer), two 30 m long electrical resistivity tomography (ERT) profiles, one along the beginning and one at the end of the EMI transect, were performed using an electrode spacing of 0.25 m.

In the post processing, first, the ERT data were inverted using RES2DINV, before the resulting conductivity-over-depth data were translated into reference EMI data (σ_a) using the forward models described in chapter 2. By fitting the measured EMI data to the reference data, two mean offset corrections are derived for the first and last 30 m of the transect, respectively. In between of the ERT reference measurements, the correction offsets are inter-

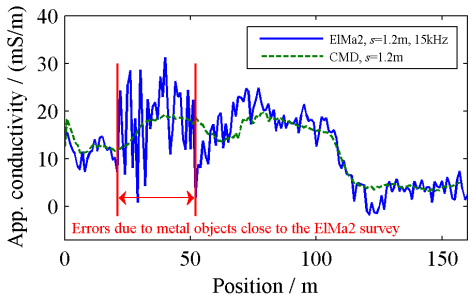

Figure 4.8.: Electromagnetic induction measurements were performed along a 158-m long transect using the new ElMa2 system (blue solid line) and a commercial EMI instrument (CMD, green dashed line), both with a Tx–Rx separation of 1.2 m. The ElMa2 data was calibrated using reference data from ERT from two 30-m measurements, one from the beginning and one from the end of the shown transect. The CMD was calibrated in the same way and shows a smaller noise level.

polated linearly for each coil configuration separately. Next, the CMD and ElMa2 data were compared qualitatively for the 1.2-m Tx–Rx separation. Finally, the ElMa2 data from six sensors in HCP coil orientation (o) and with Tx–Rx separations between 0.4 and 1.4 meter were inverted using the two-layer inversion from chapter 2. To constrain the EMI data laterally, the data were passed through a simple moving average filter over three measurement points before they were calibrated using ERT data. In addition, three obviously erroneous jumps in the EMI raw data from a 0.4-m, the 0.6-m and the 0.8-m configuration and two outliers in the 0.4-m measurement were removed.

4.3. Results and Discussion

First, the EMI measurements with 1.2-m Tx–Rx separation from the ElMa2 system and from the CMD-MiniExplorer were compared to each other (figure 4.8). The noise in the CMD data (green dashed line) is clearly smaller compared to the ElMa2 data (blue solid line), which was expected and also measured before (table 4.2). In addition, between positions 19 m and 52 m, metal objects in the surrounding of the ElMa2 system distorted the measurement values. These data are removed for further processing steps.

In general, both instruments show the same trend, with an intermediate electrical conductivity along the first 20 meters, two more conductive regions from 30 to 50 m, and from 70 to 110 m, and a very resistive region from about 120 m up to 160 m.

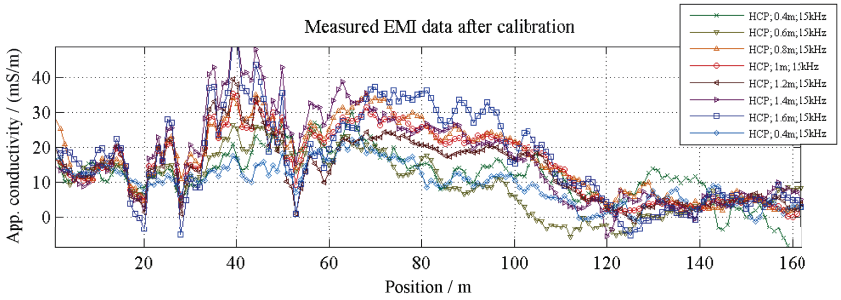

Figure 4.9.: The figure shows the calibrated ElMa2 data for all measured configurations. The influence of metallic objects between position 19 and 52 m is clearly visible, though it is most disturbing for the larger Tx–Rx separations.

The calibrated apparent conductivity from all ElMa2 sensors is shown in figure 4.9. Besides the explained distortion of the data between positions 19 and 52 m, the survey data reveals homogeneous apparent conductivity distributions-over-depth along the first 20 and the last 40 m of the transect and a heterogeneous apparent conductivity distribution in between from position 50 and 120 m. In addition, the data from one 0.4-m (green ×-symbol), the 0.6-m and the 1.6-m Rx unit stand out by being unrealistic variable along the transect and, in particular, negative at some points along the last 50 meters of the transect. Therefore, these data were considered to be less reliable and were removed from the data set before the inversion was performed. Furthermore, a skip in the 0.8-m configuration was corrected in the post-processing after carefully checking for plausibility. This skip occurred in between of two measurement locations, after the system was moved. The skip was extraordinary large (16 mS/m) and, in addition, no other sensor showed a skip between the two locations. Therefore, the skip is explained by a displacement of the Rx unit during the movement of the system, as considered in chapter 4.2.2, and the data are correct by subtracting the skip from all following measurement values.

The inverted ElMa2 data are shown in figure 4.10a. The missing data between position 18 and 49 is due to the discussed erroneous data, caused by steel in the vicinity of the sensors. The inverted data show the (from the analysis of the raw data) expected homogeneous parts along the first 20 meters and the last 40 meters of the transect. In between, the inversion reveals a plowing horizon at approximately 30-cm depth from positions 50 to 80 m, followed by some sort of conductive pit between position 80 and 120 m. In addition, the misfit for the

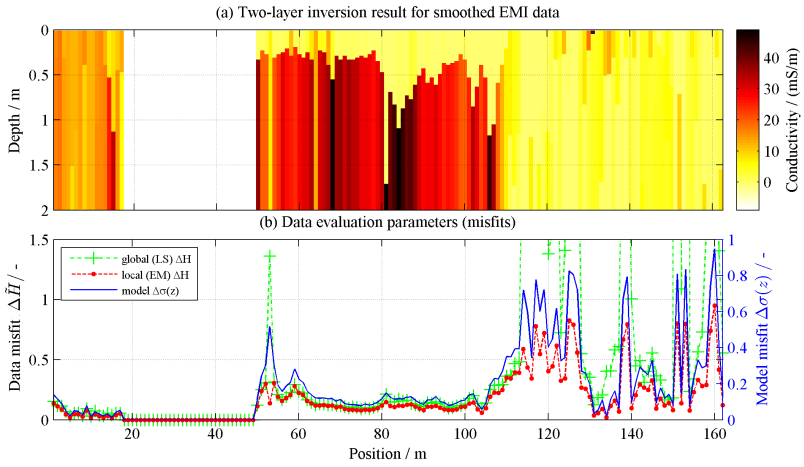

Figure 4.10.: The upper figure (a) shows inverted EMI data from our new ElMa2 system with a measurement frequency of 15 kHz and five HCP configurations (0.4, 0.8, 1.0, 1.2, and 1.4 m) using the inversion algorithm described in chapter 2 and a simple moving average over the nearest neighbors (3 m). The white region between 18 and 49 m was cleared out because of the presence of metal objects (see figure 4.8). The lower figure shows the misfit-values described in chapter 2. The small misfits from 0-20 m and 60-100 m indicate a robust inversion with sufficient EMI-configurations to describe the soil-layering. The larger misfit around 50 m and between 110 and 160 m indicate a less reliable inversion result.

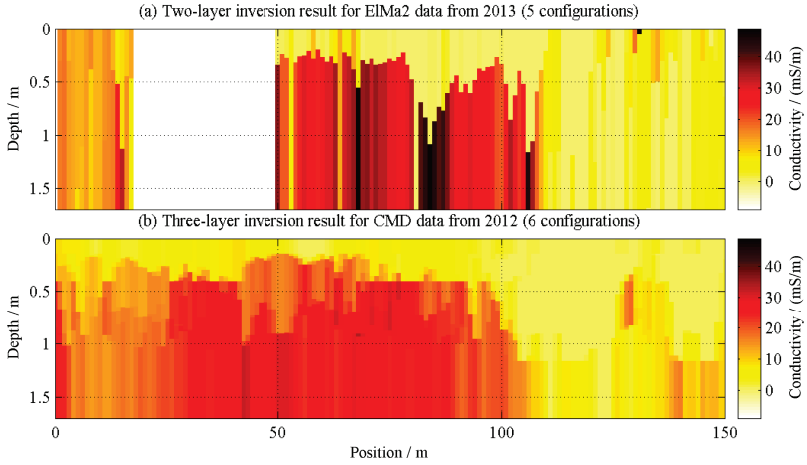

Figure 4.11.: The upper figure (a) shows inverted EMI data from our new ElMa2 system as shown in figure (4.10a). The lower figure (b) shows inverted CMD data from six configurations (0.3, 0.7, and 1.2 m Tx–Rx separation, each measured in HCP and VCP configuration) for the same transect but from 2012, which were measured and inverted by von Hebel et al. (2014). General features, like the homogeneous part in the first 20 meters and the plowing horizon at about 30 cm depth in the region between 50 and 80 meters are visible in both inversion results.

inversion (figure 4.10b) reveals that the inversion is rather robust for the first 100 meter with the smallest misfit in the homogeneous region, a slightly larger misfit in the two-layer region between 60 and 100 m, and a locally increased misfit around position 50-m. The second region with an increased misfit is at the end of the transect between 110 m and 160 m, where the inversion shows a homogeneous result, which is in good agreement with the reference ERT-data, though the EMI raw-data (figure 4.9) show slightly inconsistent trends from some EMI configurations in this region, which complicates the inversion. In general, such a large and alternating misfit indicate inconsistent (i.e. erroneous) measurement data or a too complex soil structure for the two-layer inversion approach, respectively.

In order to validate the results, the data are compared to EMI data from 2012 measured by von Hebel et al. (2014) using a CMD-MiniExplorer with three Tx–Rx separations (0.3, 0.7 and 1.2 m), each measured in horizontal coplanar loops (HCP) and vertical coplanar loops (VCP) orientations (figure 4.11). This CMD data set was inverted by von Hebel et al. (2014) using an advanced inversion algorithm, which is based on the inversion from chapter 2, but was extended for three soil layers in order to account for the increased number of

available configurations. In addition, this new inversion algorithm uses more sophisticated lateral constraints (von Hebel et al. 2014) compared to the simple moving average used for the inversion of the ElMa2 data. For comparison, both inversion results are shown in figure 4.11. Along the first 20 meters, the ElMa2 data show a homogeneous part, though the CMD exhibits a non-continuous horizon at about 30 cm depth. In the region between 50 and 80 m, both data sets consistently show a plowing horizon at about 30 cm depth with the CMD inverted data appearing more smooth in the electrical conductivity values and the depth of the plowing horizon, though the latter is about equally good resolved in both data sets. In the region between 80 and 100 m, the CMD data show a slightly deeper plowing horizon at about 40 cm, though the ElMa2 data show an even deeper first layer with a thickness between 0.5 and 1.0 m from position 80 to 90 m, followed by a similar thickness of about 40 cm between positions 90 and 100 m. Note that the region of the thicker first layer shows an (unrealistic) increase in the conductivity of the second layer in the ElMa2 data (figure 4.11a), which indicates an overestimation of the thickness of the first layer by the inversion algorithm. Along the homogeneous part from position 110 to 150 m, the results are in good agreement. To sum up, the inverted apparent conductivity data from both instruments show a rather good agreement, even though the underlying data were measured with about one year in between. Noticeable differences around position 85 m can be explained by the different inversion algorithms applied to the CMD and ElMa2 data, respectively.

4.4. Conclusions

A new prototype modular EMI field instrument (ElMa2) for near-surface applications with flexible Tx–Rx separations between 0.4 and 2.0 m was developed. Whereas the initial system, described in chapter 3, is a 230-Volt system in a 19”-rack which weighs 39 kg, the ElMa2 main unit only weighs about 10 kg, is battery-powered and fits into a backpack. The control-PC is a common laptop computer with Microsoft Windows operating system. Furthermore, the current measurement at the transmitter coil(s) is now performed in the sensor unit(s) instead of inside the measurement system and, thereby, two ADC channels were saved and the current measurement (i.e. its shunt resistor and the amplification circuit) can be adjusted to the specific coil impedance of the sensor, which increases the accuracy.

The presented system design includes nine channels that can be used either for Tx or Rx units,

resulting in up to eight simultaneously measured EMI configurations. The main difference compared to common commercial EMI devices is the modular system design which enables adjusting the configuration for a specific survey in terms of Tx–Rx separations and coil orientations, resulting in an adjustable depth resolution. The trade-off for this flexible design is a smaller signal-to-noise ratio compared to available fixed-configuration systems. Another feature of the ElMa2 system is the capability to adjust the measurement frequency in a range from 5 to 30 kHz, which enables to avoid narrow-band noise sources, as observed in section 3.3.1. Note that the system allows measuring the noise spectrum on the specific test site before the survey.

In order to optimize the efficiency of the measurement method and to reduce drift effects in the transmitter system, three types of multi-frequency excitation signals were analyzed: A "slow sequential" mode, where sinusoidal sequences are measured independently one after another, a "super-positioned" mode, where the time-series of all frequencies are summed up and excited periodically as one waveform, and a "fast sequential" mode which combines the sequential approach with the periodic excitation by using a compressed waveform, where each frequency is included for $1/\min(f)$ seconds, which is repeated for the chosen measurement time. The "slow sequential" mode shows the best signal-to-noise ratio, resulting in an σ_{a}-accuracy of up to 2 mS/m (for s=1.2 m), which was expected from the theoretical assessment. In addition, its drift characteristics are very similar compared to the "super-positioned" mode. The "fast sequential" mode shows a significantly worse drift and noise performance. Consequently, the "slow sequential" mode is considered the most accurate excitation method.

The system was tested on a well-known test site using eight receiver sensors in HCP mode with Tx–Rx separations between 0.4 and 1.6 m, and a "slow sequential" excitation signal with 1.5 Vp. Note that data from three sensors needed to be excluded from the inversion due to partly erroneous values, which were probably caused by mechanical deformation of the prototype's sensor mounting. The remaining data were inverted for true electrical conductivity over depth using the two-layer inversion described in chapter 2. For the presented case, the two-layer model is sufficient to represent the soil layering, showing a clearly resolved plowing horizon at a depth level that is in good agreement with earlier reference measurements at the same transect. In general, the data from the eight different Tx–Rx separations allow for a more detailed soil reconstruction when using a three-layer inversion approach, such as described by von Hebel et al. (2014).

5. Final Conclusions and Outlook

The presented thesis combines a novel two-layer inversion approach of multi-configuration electromagnetic induction (EMI) data (chapter 2) with the development of appropriate novel flexible-configuration EMI devices (chapter 3 & 4). In section 5.1 a final conclusion is given, whereas section 5.2 focuses on starting points for future improvements.

5.1. Conclusions

The implementation and optimization of an one-dimensional (1D) inversion algorithm that resolves the electrical conductivity of two soil layers (σ_1, σ_2) and the thickness of the first layer (h_1) without the use of a regularization is described in chapter 2. Based on the vertical sensitivity of the available EMI devices and the observed apparent electrical conductivities (σ_a), appropriate two-layer medium parameter ($\vec{p} = (\sigma_1, \sigma_2, h_1)$) ranges were estimated for a grid search that finds the two best forward models using the fast and approximate local-sensitivity forward model (LS model). These two models were refined by the less constrained simplex algorithm using the more precise full solution electromagnetic forward model (EM model). From the two refined parameter sets, the model with the smallest data misfit ($\Delta\tilde{H}$) was selected. The method was analyzed and validated by applying it to synthetic one-, two-, and three-layer models, and, in addition, to realistic models yielded from inverted electrical resistivity tomography (ERT) data. In particular, these models were processed into synthetic multi-configuration EMI data using the EM model and considering eight combinations of coil orientations (o), Tx–Rx separations (s), and measurement frequencies (f) that match with configurations of available EMI instruments: s=1.0 m with f=15 kHz, 1.2 m with 1 kHz, 1.2 m with 8 kHz, and 1.2 m with 16 kHz, each with horizontal coplanar loops (HCP) and vertical coplanar loops (VCP). The resulting apparent conductivity data were inverted back into soil models. Comparing the original model to the inverted data shows that the algorithm

is properly working for one- and two-layer soils and deviate for soils with a more complex layering. In such cases, the data misfit rises, indicating that the results are less reliable. Next, the inversion procedure was applied to quantitative measured EMI data which were collected at the same transect as the mentioned ERT data set. By analyzing the differences in the apparent conductivity data, it is shown that the coil orientation (HCP, VCP) and the Tx–Rx separation (1.0 m and 1.2 m) has the greatest influence on the sensing depth of the instrument. The used measurement frequencies (1 – 16 kHz) did not add significant information. Nevertheless, inverting measured data from the different Tx–Rx separations and coil orientations resulted in a satisfactory two-layer conductivity profile of the studied transect, which enables for geological and environmental interpretations. For example, the inverted EMI data resolve the plowing horizon of an agricultural field-site at a depth level of about 0.3 m. The results were compared to two-dimensional (2D)-inverted ERT data, which are more elaborate to measure, showing that the two-layer 1D-inversion results are in agreement at those parts of the transect, where the soil layering is horizontal and no 2D effects in the layering affect the measured data.

The experience with the inversion of EMI data from available configurations resulted in four starting points for the instrumental design of a novel EMI instrument that is described in chapters 3 and 4:

- a modular system design with flexible sensor configurations will allow to adjust and thereby improve the vertical resolution for a specific depth-region of interest,
- a multi-channel system enables to measure multiple EMI configurations simultaneously, such that the overall survey time is reduced and the data from all configurations are measured under exactly the same circumstances (e.g. ambient temperature, system conditions, soil conditions, etc.),
- the uncalibrated and uncompensated raw data should be stored such that the calibration and drift correction is reproducible and the behavior of the instrument can be studied in order to evaluate its accuracy under different measurement conditions, and
- adjustable measurement frequencies will help to avoid narrow-banded ambient noise sources.

These observations were addressed in chapter 3 by developing a novel laboratory EMI instrument design, which was analyzed and optimized in numerical studies and setup as a prototype

measurement system. The presented ElMa1 system combines novel modular EMI sensor units with an established data acquisition (DAQ) and measurement control system developed by Zimmermann et al. (2008). The system reaches an instrumental σ_a-accuracy of 1 mS/m at a Tx–Rx separation of about 1.0 m and for a measurement frequency of 20 kHz, although the sensors can be placed at different Tx–Rx separations, resulting in an apparent conductivity-accuracy of e.g. 2 mS/m for Tx–Rx separations between 0.4 and 2.3 m (f=20 kHz). See figure A.2 for more details about the instrumental σ_a-accuracy of ElMa1. Note that the maximum Tx–Rx separation depends on the ambient magnetic noise level which is in general depending on the measurement frequency and location-specific artificial noise sources. The ElMa1 system is designed to measure with frequencies between 3.3 and 33.0 kHz such that narrow-banded noisy frequency ranges can be encountered on a field-site and avoided for the measurement. In addition, the frequency range is used for spectral measurements of the coil impedance such that electrical drift effects can be observed.

In order to investigate and correct for drift effects, the receiver (Rx) and transmitter (Tx) units are kept similar to enable the measurement of its individual impedances using the same measurement system. All sensor units include air-cored Tx/Rx-coils, which were electrically shielded to avoid parasitic capacitive effects. The circuit board design allows to switch remotely between Tx-mode, which includes the coil impedance measurement, and Rx-mode, thus allowing to measure the impedances of both coils, sequentially, during a survey. The measured coil impedances contain the thermal drift of the electrical circuit and were used to simulate the Tx–Rx system. Based on these data, the original data were corrected. The results showed an instrumental σ_a-accuracy of about 30 mS/m after the correction process (compared to 500 mS/m without correction), which was observed in a drift experiment over the temperature range from 23 to 38°C, using a measurement frequency of 8 kHz. A simulation based investigation of the influence of the electrical system components on the overall drift revealed that 93 % of the drift at 8 kHz is due to the drift of the transmitter impedance. A spectral analysis showed that for the higher frequencies ($>$ 20 kHz), the amplification circuit of the receiver unit is another major source of drift effects ($>$ 24 %). Considering measurements during varying ambient temperature and typical electrical conductivity (σ) values of soils, which are between 0.1 and 100 mS/m (Rubin and Hubbard 2005, chapter 6), the achieved accuracy of the numerical drift correction (30 mS/m) needs to be improved by a more precise impedance measurement in future developments.

In order to verify the sensitivity of the system, this first prototype was set up for a measurement under ideal field-like conditions by mounting the sensor units above a homogeneous test object, which was a swimming pool filled with about 11 m^3 of tap water (σ = 50 mS/m). Though the measured values deviate from the real electrical conductivity, the system showed that it is capable of acquiring apparent conductivity data in the amplitude range of real soils and with the estimated σ_a-accuracy.

Based on the experience gained with the ElMa1 prototype system which was aimed for laboratory studies, chapter 4 describes the development of an improved EMI prototype system for field surveys (ElMa2) with optimized sensor circuits for individual transmitter current measurements and adjustments of the measurement system for mobile near-surface applications with flexible Tx–Rx separations between 0.4 and 2.0 m. A comparison between the ElMa1 and the ElMa2 system is given in table 5.1.

Table 5.1.: Comparison of the two novel electromagnetic induction systems, ElMa1 and ElMa2, which are described in detail in chapter 3 and 4, respectively.

	ElMa1	ElMa2
power supply	230 V (AC)	12 V (DC)
weight	39 kg	10 kg
dimensions (H×W×D)	46 × 56 × 50 cm (19"-rack)	4 × 38 × 34 cm (backpack)
generator output	± 10 V at 50 Ω	± 5 V at 7 Ω
number of sensor channels	up to 36[a]	9[b]
24-bit sigma-delta ADC's	✓	✓
ADC-device synchronization	PXI bus (NI)	analog reference signal
data storage & measurement controller	desktop PC	laptop PC
flexible configurations	✓	✓
measurement frequencies	3.3 – 33 kHz	5 – 30 kHz
recommended Tx–Rx separations[c]	0.4 - 2.3 m (figure A.2)	0.4 - 1.4 m (figure 4.4)

[a] limited only by the space for multiplexer units in the current setup.
[b] number can be increased in steps of three channels by including more than the current three USB-units (see chapter A.2).
[c] based on an σ_a-accuracy of 2 mS/m, an intermediate measurement frequency of 20 kHz, and a Rx-voltage noise of 30 nV/$\sqrt{\text{Hz}}$, which was observed due to environmental noise sources.

The ElMa2 system is capable of collecting data for more than four hours with one battery filling and can be operated by one person. The sensors were mounted on a modular construction kit which allows to easily change between different configurations. The system was tested on

a transect at a well-known agricultural test-site. In order to gather quantitative EMI data, the system was calibrated using collocated ERT inverted data from the beginning and the end of the analyzed EMI transect. After the calibration, the data from all configurations were manually checked for errors such as sudden skips in the data from single configurations and similar inconsistencies which are, for example, due to stiffness issues with the prototype mounting system. The remaining data were inverted using the two-layer inversion algorithm from the first part of this thesis. The presented inversion results obtained from the new ElMa2 system with HCP sensors at Tx–Rx separations of 0.4, 0.8, 1.0, 1.2, and 1.4 m and a measurement frequency of 15 kHz are in agreement with collocated inverted data from previous surveys.

Considering the achievements in the inversion of EMI data, the novel EMI system-design and the experimental results of the first test measurements, this work offers a great potential for a wide range of applications that benefit from the depth-resolution of the ElMa2 system in combination with an appropriate inversion. Note that the presented 1D inversion algorithm is already extended for a third layer by von Hebel et al. 2014. In addition to the multiple sensor channels, the modular sensor design enables for customizable configurations, including small Tx–Rx separations between 0.3 and 0.4 m. Therefore, the described system and inversion may lead to a more precise areal characterization of the shallow soil, enabling the investigation of its influence on the transport processes in the hydrological cycle.

5.2. Outlook

The following sections contain suggestions for the further development of the presented work, such as the design of a survey system with a rigid mounting system and a user-friendly operating software (section 5.2.1), the improvement of the measurement speed by increasing the sensitivity (5.2.2), the implementation of a drift-correction and calibration method (section 5.2.3), and a two- or three-dimensional inversion algorithm which unlocks the potential of the flexible EMI configurations provided by the ElMa2 system (section 5.2.4).

5.2.1. Survey System

The development of a survey system basically means to remove some known and obvious restrictions of the described ElMa2 prototype. This includes issues like the mechanical sta-

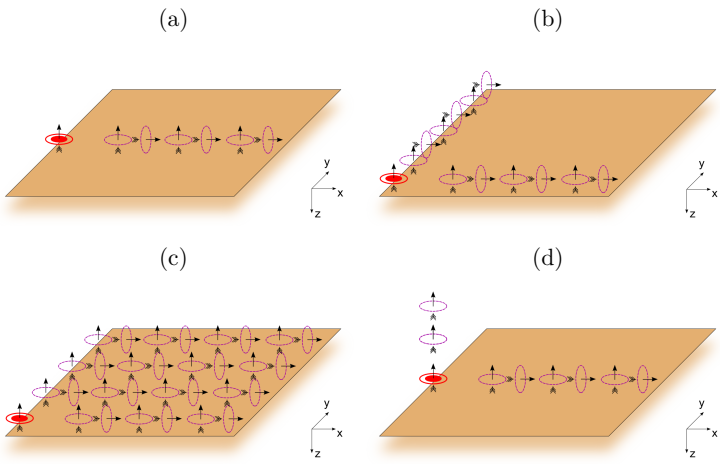

Figure 5.1.: Possible EMI sensor-configurations are (a) a linear array with the transmitter coil in vertical dipole configuration and multiple coplanar and perpendicular receiver coils, (b) a L-shaped geometry with the transmitter in the corner, (c) a fully two-dimensional array with one vertical dipole transmitter and several receivers arranged around it, and (d) a linear array with additional receivers above the transmitter.

bility and stiffness of the sledge, the focus on a specific array type (e.g. linear array), and a moisture resistant sensor housing. Since the prototype was tested successfully (see chapter 4), this 'survey system' can be setup as soon as it is needed and the specific array and sledge geometry is chosen (e.g. from figure 5.1). In addition, the actual operating software lacks a user-friendly preview of the survey data, which would be helpful to evaluate the data during the survey.

5.2.2. Sensitivity

The most important property of the system design is the achieved sensitivity, which determines the measurement speed and accuracy. The sensitivity needs to be addressed by optimizing (I) the dynamic range of the used analog-to-digital converters (ADC's) and (II) the primary magnetic field strength which depends on the magnetic moment (m) of the transmitter. For an uncompensated measurement system, such as ElMa1 and ElMa2, the required dynamic range (RDR) for a certain coil configuration cannot be altered and needs to be met by the specification of the used ADC. Therefore, switching to an ADC with increased dynamic range would result in a better sensitivity for the small Tx–Rx separations ($s < 1$ m).

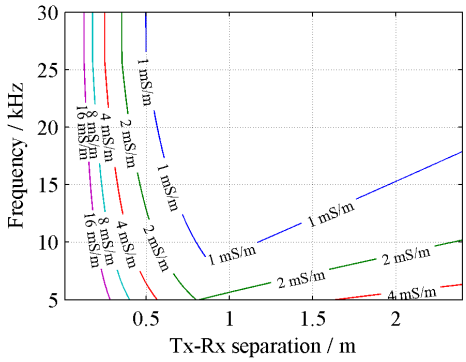

Figure 5.2.: Instrumental σ_a-accuracy for different measurement frequencies and Tx–Rx separations, a transmitter voltage of 20 Vp, and a measurement time of 0.5 s for the ElMa2 system with a shunt resistance of 20 Ω.

The accuracy for the larger Tx–Rx separations ($s > 1$ m) is limited by the environmental noise level in combination with the transmitter power. Therefore, the primary magnetic field strength (H_{p}^{*}) needs to be increased in order to achieve a better signal-to-noise ratio for the larger Tx–Rx separations. Increasing the transmitter voltage (U_{Tx}^{*}) results in a linear increase of the magnetic moment, thus an increase from 5 Vp to 20 Vp results in a significant change in the accuracy for the larger Tx–Rx separations. The estimated instrumental σ_a-accuracy for this example is shown in figure 5.2 and can be compared to that of ElMa1 and ElMa2, which is given in figure A.2 and figure 4.4, respectively.

5.2.3. Drift-Correction and Calibration

The latest results were achieved without correcting for a possible receiver drift, though the system generally allows to measure it. However, this measurement is an additional measurement which increases the overall measurement time and the focus up to this point was the development of a working prototype. Nevertheless, the ElMa2 system and its sensors were improved by enabling simultaneous impedance measurements at all sensor-channels instead of measuring it sequentially as with the ElMa1 system. In order to take advantage of this improvement, the measurement firmware and software needs be upgraded. Furthermore, the receiver-drift correction from chapter 3 needs to be included in the post-processing software.

A reliable drift-correction supports the calibration of the system because it enables the cal-

ibration based on a single vertical soil conductivity profile. However, a reliable and efficient calibration method needs to be found, too.

5.2.4. Inversion

At the moment, the possible coil configurations are limited by the used inversion software which only allows to process HCP and VCP coil orientations, though the novel ElMa2 system enables flexible sensor orientations like the ones given in figure 5.1. Therefore, the forward model and the inversion from chapter 2 needs to be improved to support the flexibility of the novel EMI system. Such a forward model would also be useful to find the most appropriate sensor configurations for a specific survey. The combination of the ElMa2 measurement system with a 2D or three-dimensional (3D) forward model would allow to investigate 2D or 3D structures, respectively, which could be measured in a single survey and even for a single measurement transect when using a perpendicular or 2D sensor array like for example shown in figure 5.1 (b) and (c).

Appendix

A. Hardware

A.1. ElMa1 System

The ElMa1-system is shown in figure A.1. It includes 24-bit Delta-sigma ADC devices (NI PXI-4472) which are sampled synchronously using a PXI bus system and a personal computer (PC). More details about the ADC can be found in table A.1. Furthermore, an Agilent generator (33220A) is included, which is controlled via universal serial bus (USB) by the PC and is capable of generating sinusoidal and arbitrary signals with up to 10 Vp. More details about the generator can be found in table A.2. The system is completed by a custom-made multiplexer unit (see appendix A.3) which consists of a chassis with up to ten multiplexer boards, each of them providing four sensor channels which can be switched either to the signal generator or to the ADC input. The multiplexer is also controlled by the measurement PC. In addition, the multiplexer chassis contains a board with the shunt resistors (R_s) which are used to measure the transmitter current and the coil impedances. The whole measurement

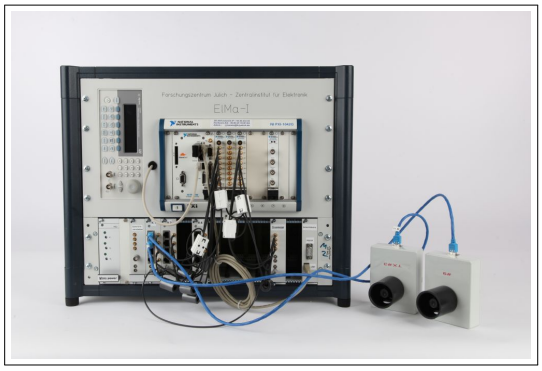

Figure A.1.: Picture of the ElMa1 measurement system, including a signal generator (upper left), a personal computer with ADC-boards (center), the multiplexer unit (bottom) and two exemplary sensor units (bottom right).

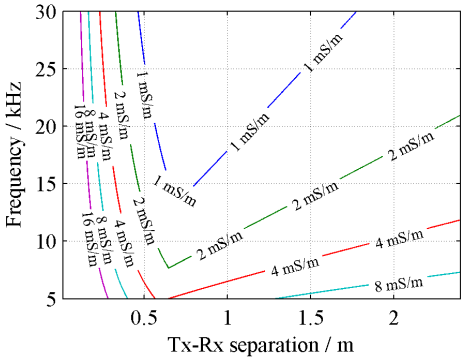

Figure A.2.: Instrumental σ_a-accuracy of the ElMa1 system with R_s=10 Ωand for Tx–Rx separations of up to 2 m and a frequency range from 5 to 30 kHz. The iso-σ_a-lines mark the configurations with equal and better instrumental accuracy as indicated at the line.

system is integrated in a small 19"-rack and needs to be powered over a 230 V supply.

Instrumental Accuracy

The instrumental σ_a-accuracy of the ElMa1 system can be estimated for the measured receiver noise voltage of 30 nV/$\sqrt{\text{Hz}}$ and based on the specified dynamic range of the ADC units. The result for the system with a shunt resistance of 10 Ω is shown in figure A.2.

Note that the observed accuracy for the smaller Tx–Rx separations (left limit in figure A.2) is even better than the estimated value in the figure, which is based on the specified dynamic range of the ADC ($8.9 \cdot 10^4$).

Analog-to-digital Converter Boards

For the data acquisition, National Instruments PXI-4472 boards are used in combination with a PXI-1042 chassis and a PXI-8196 controller. The specification of the ADC-devices is given in table A.1 and a picture is shown in figure A.3.

Signal Generator

To generate the transmitter signals, an Agilent 33220A function generator (see figure A.4) is included in the ElMa1 system. Some of its specifications are summarized in table A.2.

Table A.1.: Specification of National Instruments PXI-4472 boards, based in the manufactures manual (373861D-01 from July 2009).

connection port	PXI
input channels per board	8
voltage range	± 10 V
resolution	24 bits
maximum sampling rate	102.4 kS/s
dynamic range	99 dB[a]
total harmonic distortion	-103 dB[a] (-89 dB)[b]
maximum alias free bandwidth	45 kHz
interchannel phase mismatch	$< f_{\text{in}}$ (in kHz) × 0.3 mrad + 1.4 mrad

[a]measured with 1 kHz sine input, -1 dBFS, and 102.4kS/s.
[b]measured with 20 kHz sine input, -1 dBFS, and 102.4kS/s.

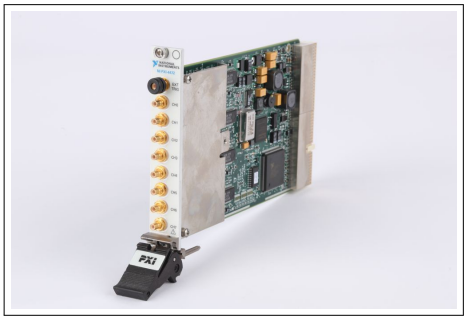

Figure A.3.: National Instruments PXI-4472.

Figure A.4.: Agilent 33220A signal generator.

Table A.2.: Specifications of the Agilent 33220A signal generator.

connection port	GPIB, USB, LAN
resolution	14 bits
signal type's	Sine, Square, Ramp, Triangle, Pulse, Noise, DC, Arbitrary
output voltage range	± 10 V
power supply voltage	230 V

A.2. ElMa2 System

The ElMa2 system is a replacement for the ElMa1 measurement system and is optimized for portable operation (figure A.5). Major changes are due to the required change to a 12-V based power supply and the reduction of the size and weight of the system. The ElMa2 system includes three ADC devices with nine sensor channels and a 12-V LiFePO battery with sufficient power to supply the system for more than four hours.

The desktop-PC in the ElMa1 system is replaced by a laptop computer which is powered by its own replaceable battery. In order to replace the ADC units and the signal generator with 12-V powered devices, two disadvantages were accepted: First, the new Agilent U2761-USB signal generator outputs only half of the formerly used voltage (5 Vp), resulting in a weaker magnetic moment of the transmitter, and, second, each National Instruments USB-4431 ADC unit only includes four input channels and does not provide a PXI bus for inter-device synchronization. Therefore, one of the four channels is used to synchronize multiple ADC units to each other, resulting in only three channels per device left for connecting sensor units, and the transmitter power is increased by decreasing the output impedance of the generator to 7 Ω using an external driver unit.

In addition, the sensor boards were optimized based on the experience with the earlier versions. For example, the number of required ADC-channels for the current measurement is reduced by combined the shunt resistor with a differential amplifier, which saves one of the two ADC-channel which were formerly used to digitize both signals separately. More information about the sensor units can be found in chapter A.4 (Sensor V3).

Analog-to-digital Converter Units

Multiple USB-4431 devices from National Instruments are used in ElMa2 for the data acquisition in combination with a laptop computer. The specification of the devices is given in table A.3 and a picture of a single device is shown in figure A.6. Compared to the PXI-4472 units, these ADC units are only slightly weaker in terms of dynamic range.

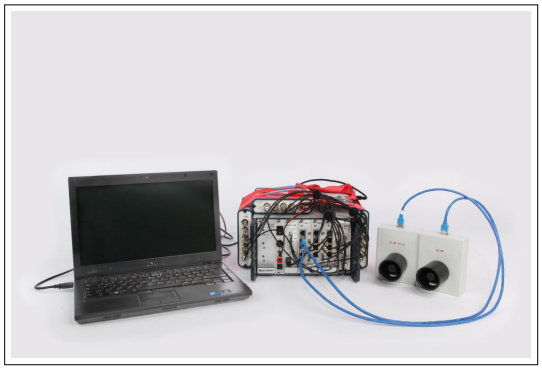

Figure A.5.: Picture of a ElMa2 measurement system. The ElMa2 system unit in the middle of the image fits into a backpack that can be used to carry the instrument. The laptop computer is used to control the measurement and store the data. Exemplary, two single sensor units are connected and shown on the right side.

Table A.3.: Specification of National Instruments USB-4431 devices, based in the manufactures manual.

connection port	USB
input channels per device	4
voltage range	± 10 V
resolution	24 bits
maximum sampling rate	102.4 kS/s
dynamic range	99 dB[a]
total harmonic distortion	-93 dB[b] (-87 db)[c]
interchannel phase mismatch	$< f_{\text{in}}$ (in kHz) × 0.7 mrad

[a] measured with 1 kHz sine input, -1 dBFS, and 102.4kS/s.
[b] for distortion frequencies smaller than 20 kHz, -1 dBFS, and 102.4kS/s.
[c] for distortion frequencies smaller than 46 kHz, -1 dBFS, and 102.4kS/s.

Signal Generator

In the ElMa2 system, the Agilent U2761A USB signal generator was included. Some details about the generator are summarized in table A.4 and a picture of a separate device is shown in figure A.7.

Figure A.6.: National Instruments USB-4431.

Figure A.7.: Agilent U2761A signal generator.

Table A.4.: Specifications of the Agilent U2761A USB signal generator.

connection port	USB
resolution	14 bits (waveform); 4 digits (common)
signal type's	Sine, Square, Ramp, Triangle, Pulse, DC, Arbitrary
output voltage range	± 5 V (50 Ω), ± 10 V (open cicuit)
power supply voltage	12 V

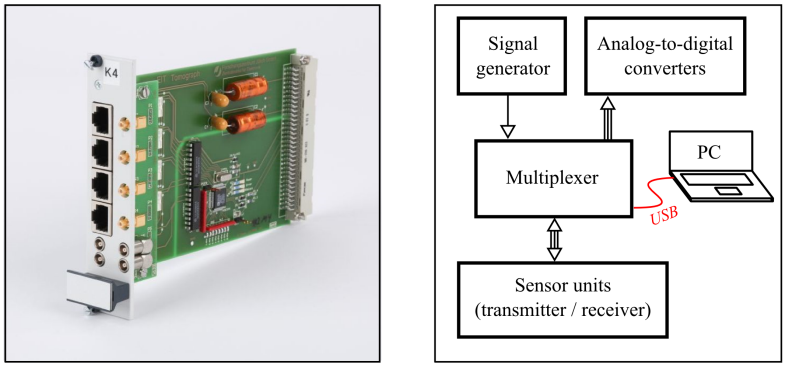

(a) (b)

Figure A.8.: Picture of (a) a single multiplexer board and (b) a flow chart of the multiplexer environment.

A.3. Multiplexer

Both generations of ElMa-systems use custom modular multiplexer units that allow switching the generator signal to a specific sensor channel and switching the sensor boards from transmitter-current measurement (Tx mode) to receiver-voltage measurement (Rx mode) and vice versa. The multiplexer is placed in between the generator, the ADC's and the sensor boards. Figure A.8 shows a picture of a multiplexer chassis with a disassembled board and a flow chart of the multiplexer environment.

A.4. Sensor Units

Sensor V1 (for ElMa1)

The first version of the EMI sensor boards contains a switch that is controlled through the multiplexer and either connects the coil to the generator signal (Tx mode) or to the amplification circuit (Rx mode). A picture and a block chart of the device is shown in figure A.9. The current through the transmitter coils is measured at a shunt resistor on a separate measurement board inside the ElMa1 main unit.

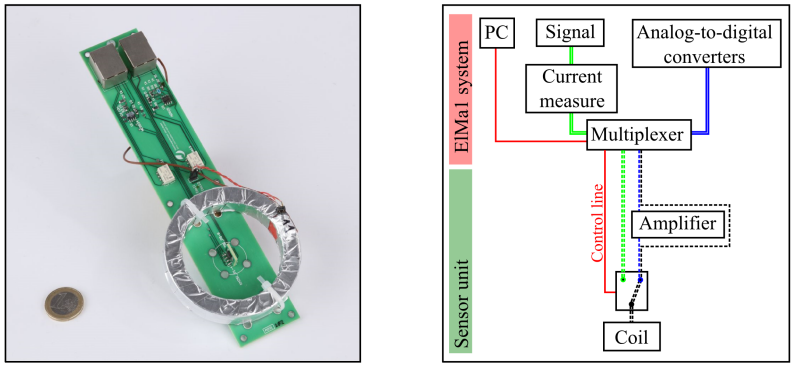

(a) (b)

Figure A.9.: Picture of (a) a sensor board (V1) and (b) a block chart of the system circuit.

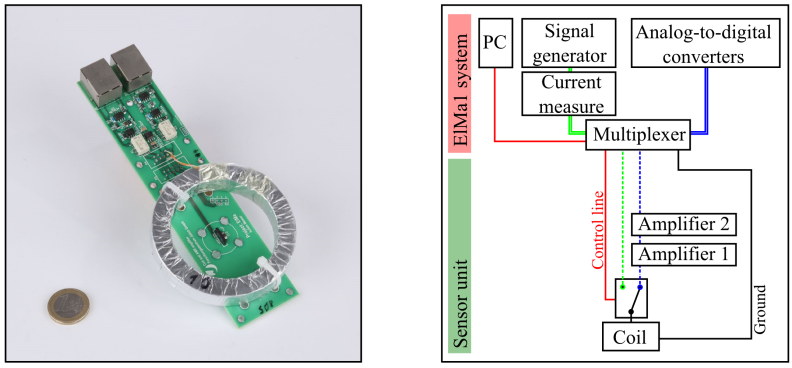

(a) (b)

Figure A.10.: Picture of (a) a sensor board (V2) and (b) a block chart of the system circuit.

Sensor V2 (for ElMa1)

The second version of the sensor board is a remake of the first version but with a second amplification circuit in series to the previous one and some minor changes regarding the circuit layout and in particular the ground plane (figure A.10). Note that in this version, a common ground is used for the generator signal and the voltage measurement.

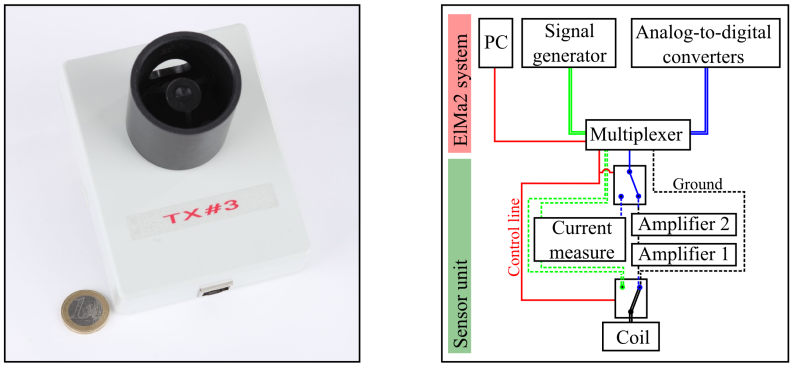

(a) (b)

Figure A.11.: Picture of (a) a sensor board (V3) and (b) a block chart of the system circuit.

Sensor V3 (for ElMa2)

The third version of the sensor board is developed for the ElMa2 system and includes an independent current measurement circuit that is optimized for each sensor unit (figure A.11). Technically, the sensor unit is still compatible with the ElMa1 system, though the signal output channel is now either used to transfer the magnetic field signal or the current signal. Furthermore, the rearrangement of the circuit components allowed to decrease the size of the sensor. In addition, the second amplification circuit ('amplifier 2' in figure A.11b) is now adjustable by four included resistances that can be switched into the circuit manually.

A.5. MOTU System

For measuring the ambient magnetic noise level and the electromagnetic noise of the ElMa systems, an audio recorder system (*UltraLite-mk3 Hybrid*[1]) was used. The setup for such a measurement is shown in figure A.12. Table A.5 gives a brief overview of the specifications of the MOTU-system.

For the magnetic noise measurement, a single sensor unit was attached to one of the six analogue input channels of the MOTU device, which is connected to a laptop computer. The system ships with drivers and software for Microsoft Windows 7 (CueMix FX) that allow to view the magnetic noise spectrum from the sensor board. Since both devices do

[1] from Mark of the Unicorn (MOTU), Inc., Cambridge, MA, USA.

Figure A.12.: Picture of the required equipment for noise measurements (from left to right): A sensor unit (V3) with its power supply unit (in front of it), the MOTU UltraLite-mk3 Hybrid (middle), and a laptop PC.

Table A.5.: Selection of specified properties of the MOTU UltraLite-mk3 Hybrid device. More information can be found by the manufacturer, e.g. `http://www.motu.com`.

sampling rate	192 kHz (S/PDIF: 96 kHz)
analog input channels	6
digital input channels	2 (S/PDIF)
analog output channels	10
digital output channels	2 (S/PDIF)
interface	USB 2.0, Firewire A
included drivers	ASIO, WDM, GSIF, MIDI
power supply	8-18 V, 12 W
Spcification of the included analog-to-digital converter:	
name	Cirrus Logic CS5368
type	24-bit Delta-Sigma
dynamic range	-105 dB (THD+N)
maximum sampling rate	216 kHz
number of input channels	8

not require much power, they can easily be supplied by batteries, making the system mobile and only a minor source of electromagnetic noise, compared to the ElMa systems. In order to locate noise sources, the ElMa1 system was powered on step-by-step while looking at the noise spectrum using the MOTU setup. Unsuitable transformers were replaced by less noisy onces. Furthermore, the system was used to study the ambient magnetic noise level at various locations on the campus to ensure noise conditions which are similar to usual field-site conditions before setting up the larger ElMa1 system.

A.6. Commercial EMI Instruments

Within this thesis, three commercial EMI instruments were used which are briefly described in the following list. Note that the receiver orientation is given in relation to the transmitter orientation using the common abbreviations: HCP (horizontal coplanar loops), VCP (vertical coplanar loops), and PRP (perpendicular loops).

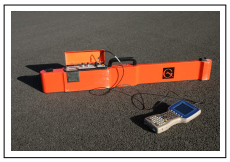

EM38-MK2
Manufacturer: Geonics Limited, Mississauga, ON, Canada
Tx-Rx separation: 0.5 and 1.0 m
Coil orientation: HCP or VCP
Measurement frequency: 14.6 kHz

CMD-MiniExplorer
Manufacturer: GF Instruments s.r.o., Brno, Czech Republic
Tx-Rx separation: 0.3, 0.7, and 1.2 m
Coil orientation: HCP or VCP
Measurement frequency: 30 kHz

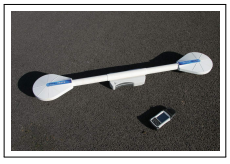

Profiler EMP-400
Manufacturer: Geophysical Survey Systems, Inc. (GSSI), Salem, NH, USA
Tx-Rx separation: 1.2 m
Coil orientation: HCP or VCP
Measurement frequency: 1, 2, . . . , 16 kHz (three per run)

List of Figures

List of Tables

Bibliography

Abdu, H., D. A. Robinson, M. Seyfried, and S. B. Jones (2008). Geophysical imaging of watershed subsurface patterns and prediction of soil texture and water holding capacity. *Water Resour. Res.* **44**. DOI: 10.1029/2008WR007043.

Anderson, W. L. (1979). Numerical integration of related hankel transforms of orders 0 and 1 by adaptive digital filtering. *Geophysics* **44**(7), 1287–1305. DOI: 10.1190/1.1441007.

Archie, G. E. (1942). The electrical resistivity log as an aid in determining some reservoir characteristics. *Trans. Am. Inst. Min. Metall. Pet. Eng.* **146**(1), 54–62. DOI: 10.2118/942054-G.

Auken, E. and A. V. Christiansen (2004). Layered and laterally constrained 2D inversion of resistivity data. *Geophysics* **69**(3), 752–761. DOI: 10.1190/1.1759461.

Boll, R. and K. J. Overshott, eds. (1989). *Magnetic Sensors*. 1st ed. Vol. 5. Sensors. Weinheim: VCH. ISBN: 3527267719.

Bonsall, J., R. Fry, C. Gaffney, I. Armit, A. Beck, and V. Gaffney (2013). Assessment of the CMD Mini-Explorer, a new low-frequency multi-coil electromagnetic device, for archaeological investigations. *Archaeol. Prospect.* **20**(3), 219–231. DOI: 10.1002/arp.1458.

Bornemann, L., G. Welp, and W. Amelung (2010). Particulate organic matter at the field scale: rapid acquisition using mid-infrared spectroscopy. *Soil Sci. Soc. Am. J.* **74**(4), 1147–1156. DOI: 10.2136/sssaj2009.0195.

Bosnar, M. (2006). Terrain conductivity meter for geological mapping, corrects temperature of received signal, based on temperature adjustment value selected from table stored in memory with respect to detected temperature of receiver coil. Pat. (US2003184301-A1; CA2424250-A1; US6710599-B2; CA2424250-C).

— (2010). Electromagnetic ground conductivity meter for use in site survey, has transmitter and receiver coils positioned at preset distance above ground when conductivity readings are determined by logging computer to calculate correction factor. Pat. (US2009201024-A1; CA2652719-A1; US7759941-B2).

Bosnar, M., J. McNeill, and G. Black (1978). Direct reading terra in conductivity meter - has transmitter coil and receiver coil mounted on opposite ends of horizontal boom. Pat. (US4070612-A; SE7612997-A; CA1036221-A).

Busch, S. (2013). Full-waveform inversion of surface ground penetrating radar data and coupled hydrogeophysical inversion for soil hydraulic property estimation. Diss. Jülich: RWTH Aachen University, Forschungszentrum Jülich GmbH (publ.)

Corwin, D. L. and S. M. Lesch (2003). Application of soil electrical conductivity to precision agriculture. *Agron. J.* **95**(3), 455–471.

Corwin, D. and S. Lesch (2005). Apparent soil electrical conductivity measurements in agriculture. *Comput. Electron. Agr.* **46**(1-3), 11–43. DOI: 10.1016/j.compag.2004.10.005.

Fuellekrug, M. and A. C. Fraser-Smith (2011). The Earth's electromagnetic environment. *Geophys. Res. Lett.* **38**, L21807. DOI: 10.1029/2011GL049572.

Guérin, R., Y. Méhéni, G. Rakotondrasoa, and A. Tabbagh (1996). Interpretation of slingram conductivity mapping in near-surface geophysics: using a single parameter fitting with 1d model. *Geophys. Prospect.* **44**(2), 233–249. DOI: 10.1111/j.1365-2478.1996.tb00148.x.

Hendrickx, J. M. H., B. Borchers, D. L. Corwin, S. M. Lesch, A. C. Hilgendorf, and J. Schlue (2002). Inversion of soil conductivity profiles from electromagnetic induction measurements: Theory and experimental verification. *Soil Sci. Soc. Am. J.* **66**(3), 673–685.

Hoekstra, P., R. Lahti, J. Hild, C. Bates, and D. Phillips (1992). Case-histories of shallow time domain electromagnetics in environmental site assessment. *Ground Water Monit. R.* **12**(4), 110–117. DOI: 10.1111/j.1745-6592.1992.tb00069.x.

Jadoon, K. Z., S. Lambot, B. Scharnagl, J. van der Kruk, E. Slob, and H. Vereecken (2010). Quantifying field-scale surface soil water content from proximal GPR signal inversion in the time domain. *Near Surf. Geophys.* **8**(6), 483–491. DOI: 10.3997/1873-0604.2010036.

Kachanoski, R., E. Gregorich, and I. Vanwesenbeeck (1988). Estimating spatial variations of soil-water content using noncontacting electromagnetic inductive methods. *Can. J. Soil Sci.* **68**(4), 715–722.

Kaufman, A. and G. V. Keller (1983). *Frequency and transient soundings.* Vol. 16. Methods in Geochemistry and Geophysics. Amsterdam, Oxford, New York: Elsevier Science Publishing Company Inc. ISBN: 0444420320.

Keller, G. V. (1988). 2. Rock and Mineral Properties. In: *Electromagnetic Methods in Applied Geophysics - Theory.* **1**. Investigations in Geophysics (3). Tulsa: Society of Exploration Geophysicists, 12–51. ISBN: 0931830516.

Lagarias, J. C., J. A. Reeds, M. H. Wright, and P. E. Wright (1998). Convergence properties of the nelder-mead simplex algorithm in low dimensions. *SIAM J. Optimiz.* **9**, 112–147.

Lavoue, F., J. van der Kruk, J. Rings, F. Andre, D. Moghadas, J. Huisman, S. Lambot, L. Weihermüller, J. van der Borght, and H. Vereecken (2010). Electromagnetic induction calibration using apparent electrical conductivity modelling based on electrical resistivity tomography. *Near Surf. Geophys.* **8**(6), 553–561. DOI: 10.3997/1873-0604.2010037.

Lesch, S. M., D. J. Strauss, and J. D. Rhoades (1995). Spatial prediction of soil salinity using electromagnetic induction techniques: 2. An efficient spatial sampling algorithm suitable for multiple linear regression model identification and estimation. *Water Resour. Res.* **31**(2), 387–398. DOI: 10.1029/94WR02180.

Lück, E., R. Gebbers, J. Ruehlmann, and U. Spangenberg (2009). Electrical conductivity mapping for precision farming. *Near Surf. Geophys.* **7**, 15–25. DOI: 10.3997/1873-0604.2008031.

McNeill, J. (1980). *Electromagnetic terrain conductivity measurement at low induction numbers. Tech note TN-6, Geonics Ltd.* Tech. rep.

Mester, A., E. Zimmermann, J. van der Kruk, H. Vereecken, and S. van Waasen (2014). Development and drift-analysis of a modular electromagnetic induction system for shallow ground conductivity measurements. *Meas. Sci. Technol.* **25**(5), 055801. DOI: 10.1088/0957-0233/25/5/055801.

Mester, A., J. van der Kruk, E. Zimmermann, and H. Vereecken (2011). Quantitative two-layer conductivity inversion of multi-configuration electromagnetic induction measurements. *Vadose Zone J.* **10**(4), 1319 –1330. DOI: 10.2136/vzj2011.0035.

Mester, A., E. Zimmermann, C. von Hebel, J. van der Kruk, H. Vereecken, and S. van Waasen (in prep.). Field-optimization and validation of a novel multi-channel electromagnetic induction system.

Minsley, B. J., B. D. Smith, R. Hammack, J. I. Sams, and G. Veloski (2012). Calibration and filtering strategies for frequency domain electromagnetic data. *J. Appl. Geophys.* **80**, 56–66. DOI: 10.1016/j.jappgeo.2012.01.008.

Moghadas, D., F. Andre, J. H. Bradford, J. van der Kruk, H. Vereecken, and S. Lambot (2012). Electromagnetic induction antenna modelling using a linear system of complex antenna transfer functions. *Near Surf. Geophys.* **10**(3), 237–247. DOI: 10.3997/1873-0604.2012002.

Monteiro Santos, F. A., J. Triantafilis, R. S. Taylor, S. Holladay, and K. E. Bruzgulis (2010a). Inversion of conductivity profiles from EM using full solution and a 1-D laterally constrained algorithm. *J. Environ. Eng. Geoph.* **15**(3), 163–174.

Monteiro Santos, F. A., J. Triantafilis, K. E. Bruzgulis, and J. A. E. Roe (2010b). Inversion of multiconfiguration electromagnetic (DUALEM-421) profiling data using a one-dimensional laterally constrained algorithm. *Vadose Zone J.* **9**(1), 117–125. DOI: http://dx.doi.org/10.2136/vzj2009.0088.

Monteiro Santos, F. A. (2004). 1-D laterally constrained inversion of EM34 profiling data. *J. Appl. Geophys.* **56**(2), 123–134. DOI: http://dx.doi.org/10.1016/j.jappgeo.2004.04.005.

Monteiro Santos, F. A., J. Triantafilis, and K. Bruzgulis (2011). A spatially constrained 1D inversion algorithm for quasi-3D conductivity imaging: Application to DUALEM-421 data collected in a riverine plain. *Geophysics* **76**(2), B43–B53. DOI: 10.1190/1.3537834.

Nielsen, D., J. Biggar, and K. Erh (1973). Spatial variability of field-measured soil-water properties. [*object object*] **42**(7), 215–259.

Nüsch, A.-K., P. Dietrich, U. Werban, and T. Behrens (2010). Acquisition and reliability of geophysical data in soil science. [*object object*].

Pellerin, L and P. Wannamaker (2005). Multi-dimensional electromagnetic modeling and inversion with application to near-surface earth investigations. *Comput. Electron. Agr.* **46**(1-3), 71–102. DOI: 10.1016/j.compag.2004.11.017.

Piessens, R., E. de Doncker-Kapenga, C. W. Überhuber, and D. K. Kahaner (1983). *Quadpack: A Subroutine Package for Automatic Integration*. 1st ed. Vol. 1. Springer Series in Computational Mathematics. Berlin Heidelberg: Springer. ISBN: 0387125531.

Reedy, R. C. and B. R. Scanlon (2003). Soil water content monitoring using electromagnetic induction. *J. Geotech. Geoenviron.* **129**(11), 1028–1039. DOI: 10.1061/(ASCE)1090-0241(2003)129:11(1028).

Revil, A., L. M. Cathles, S. Losh, and J. A. Nunn (1998). Electrical conductivity in shaly sands with geophysical applications. *J. Geophys. Res.* **103**(B10), 23925–23936. DOI: 10.1029/98JB02125.

Rhoades, J. D. (1993). Electrical conductivity methods for measuring and mapping soil salinity. In: *Advances in Agronomy*. Ed. by D. L. Sparks. **49**. San Diego: Academic Press, 201–251. ISBN: 978-0-12-000749-3.

Robinson, D. A., I. Lebron, S. M. Lesch, and P. Shouse (2004). Minimizing drift in electrical conductivity measurements in high temperature environments using the EM-38. *Soil Sci. Soc. Am. J.* **68**(2), 339–345.

Robinson, D. et al. (2008). Advancing process-based watershed hydrological research using near-surface geophysics: a vision for, and review of, electrical and magnetic geophysical methods. *Hydrol. Process.* **22**(18), 3604–3635. DOI: 10.1002/hyp.6963.

Rubin, Y. and S. S. Hubbard, eds. (2005). *Hydrogeophysics*. Water Science and Technology Library. Berlin, Heidelberg, New York: Springer. ISBN: 978-1-4020-3102-1.

Saey, T., D. Simpson, H. Vermeersch, L. Cockx, and M. van Meirvenne (2009). Comparing the EM38DD and DUALEM-21S sensors for depth-to-clay mapping. *Soil Sci. Soc. Am. J.* **73**(1), 7–12. DOI: 10.2136/sssaj2008.0079.

Saey, T., M. van Meirvenne, P. de Smedt, L. Cockx, E. Meerschman, M. M. Islam, and F. Meeuws (2011). Mapping depth-to-clay using fitted multiple depth response curves of a proximal EMI sensor. *Geoderma*. DOI: 10.1016/j.geoderma.2011.01.015.

Saey, T., P. de Smedt, M. M. Islam, E. Meerschman, E. van de Vijver, A. Lehouck, and M. van Meirvenne (2012). Depth slicing of multi-receiver EMI measurements to enhance the delineation of contrasting subsoil features. *Geoderma* **189–190**, 514–521. DOI: 10.1016/j.geoderma.2012.06.010.

Sherlock, M. D. and J. J. McDonnell (2003). A new tool for hillslope hydrologists: spatially distributed groundwater level and soilwater content measured using electromagnetic induction. *Hydrol. Process.* **17**(10), 1965–1977. DOI: 10.1002/hyp.1221.

Siemon, B., A. V. Christiansen, and E. Auken (2009). A review of helicopter-borne electromagnetic methods for groundwater exploration. *Near Surf. Geophys.* **7**(5-6), 629–646. DOI: 10.3997/1873-0604.2009043.

Simpson, D., M. van Meirvenne, T. Saey, H. Vermeersch, J. Bourgeois, A. Lehouck, L. Cockx, and U. W. A. Vitharana (2009). Evaluating the multiple coil configurations of the EM38DD and DUALEM-21S sensors to detect archaeological anomalies. *Archaeol. Prospect.* **16**(2), 91–102. DOI: 10.1002/arp.349.

Slob, E. and J. Fokkema (2002). Coupling effects of two electric dipoles on an interface. *Radio Sci.* **37**(5), 1073–1082. DOI: 200210.1029/2001RS002529.

Strassacker, G. and P. Strassacker (1993). *Analytische und numerische Methoden der Feldberechnung*. Stuttgart: B.G. Teubner. ISBN: 3519061686.

Sudduth, K. A., S. T. Drummond, and N. R. Kitchen (2001). Accuracy issues in electromagnetic induction sensing of soil electrical conductivity for precision agriculture. *Comput. Electron. Agr.* **31**(3), 239–264. DOI: 10.1016/S0168-1699(00)00185-X.

Tezkan, B. (1999). A review of environmental applications of quasi-stationary electromagnetic techniques. *Surv. Geophys.* **20**(3-4), 279–308. DOI: 10.1023/A:1006669218545.

Triantafilis, J. and S. M. Lesch (2005). Mapping clay content variation using electromagnetic induction techniques. *Comput. Electron. Agr.* **46**(1-3), 203–237. DOI: 10.1016/j.compag.2004.11.006.

Triantafilis, J. and F. A. Monteiro Santos (2010). Resolving the spatial distribution of the true electrical conductivity with depth using EM38 and EM31 signal data and a laterally constrained inversion model. *Aust. J. Soil Res.* **48**(5), 434–446. DOI: 10.1071/SR09149.

Triantafilis, J. and F. A. Monteiro Santos (2011). Hydrostratigraphic analysis of the Darling River valley (Australia) using electromagnetic induction data and a spatially constrained algorithm for quasi-three-dimensional electrical conductivity imaging. *Hydrogeol. J.* **19**(5), 1053–1063. DOI: 10.1007/s10040-011-0739-9.

Urdanoz, V., E. Amezketa, I. Clavería, V. Ochoa, and R. Aragüés (2008). Mobile and georeferenced electromagnetic sensors and applications for salinity assessment. *Span. J. Agric. Res.* **6**(3), 469–478.

van der Kruk, J. (1995). The determination of the apparent resistivity of the Earth from electromagnetic sounding with magnetic dipoles. Master's thesis. Delft: Delft University of Technology.

van der Kruk, J., J. Meekes, P. van den Berg, and J. Fokkema (2000). An apparent-resistivity concept for low-frequency electromagnetic sounding techniques. *Geophys. Prospect.* **48**(6), 1033–1052. DOI: 10.1046/j.1365-2478.2000.00229.x.

von Hebel, C., S. Rudolph, A. Mester, J. A. Huisman, P. Kumbhar, H. Vereecken, and J. van der Kruk (2014). Three-dimensional imaging of subsurface structural patterns using quantitative large-scale multiconfiguration electromagnetic induction data. *Water Resour. Res.* **50**(3), 2732–2748. DOI: 10.1002/2013WR014864.

Wait, J. R. (1982). *Geo-Electromagnetism*. New York, London, Paris: Academic Press Inc. ISBN: 0127308806.

Ward, S. H. and G. W. Hohmann (1988). 4. Electromagnetic Theory for Geophysical Applications. In: *Electromagnetic Methods in Applied Geophysics - Theory*. **1**. Investigations in Geophysics (3). Tulsa: Society of Exploration Geophysicists. ISBN: 0931830516.

Weihermüller, L., J. A. Huisman, S. Lambot, M. Herbst, and H. Vereecken (2007). Mapping the spatial variation of soil water content at the field scale with different ground penetrating radar techniques. *J. Hydrol.* **340**(3-4), 205–216. DOI: 10.1016/j.jhydrol.2007.03.013.

Zimmermann, E., A. Verweerd, W. Glaas, A. Tillmann, and A. Kemna (2005). An AMR sensor-based measurement system for magnetoelectrical resistivity tomography. *IEEE Sens. J.* **5**(2), 233–241. DOI: 10.1109/JSEN.2005.843889.

Zimmermann, E., A. Kemna, J. Berwix, W. Glaas, and H. Vereecken (2008). EIT measurement system with high phase accuracy for the imaging of spectral induced polarization properties of soils and sediments. *Meas. Sci. Technol.* **19**(9), 094010. DOI: 10.1088/0957-0233/19/9/094010.

Glossary

CMD-MiniExplorer: a commercial EMI-device from GF Instruments → chapter A.6.

dynamic range: the quotient of the largest and smallest signals, which can be acquired simultaneously with a data acquisition system.

electromagnetic forward model: the full solution electromagnetic forward model described by van der Kruk 1995.

ElMa1: the new EMI measurement system, version 1: prototype for stationary use.

ElMa2: the new EMI measurement system, version 2: prototype for field use.

EM38-MK2: a commercial EMI-device from Geonics Limited → chapter A.6.

fast sequential waveform: labeling for a special signal shape used here. The corresponding signal is a fast/often switched sequence of sinusoidal signals.

field-scale: classifies the size of an area. The term "field" refers to the typical size of agricultural used plots, which is here in the order of up to a few hectare (1 ha = 100 m × 100 m).

half-space: is a term from mathematical modeling. The solution of a model is simplified by neglecting half of the space (e.g. the upper half-space) that is surrounding a sensor. Here, it is assumed that no induction currents are induced in the air above the sensors.

instrumental σ_a-accuracy: assuming that the device is used under conditions as described by McNeill (1980), where $|\mu_r| = 1$ and the instrument elevation is zero, and that the ambient magnetic noise level (B_{noise}) is 10^{-13} T/$\sqrt{\text{Hz}}$ or the equivalent of the measured induced voltage noise (U_{n}) of ≤ 30 nV.

local-sensitivity forward model: the frequency-independent model described by McNeill 1980.

lock-in technique: method to extract the in-phase and out-of-phase component of a known frequency out of a measurement signal.

multiplexer: switch-box for automatically switching input/output channel).

Profiler EMP-400: a commercial EMI-device from Geophysical Survey Systems (GSSI) → chapter A.6.

PXI bus: "PCI eXtensions for Instrumentation BUS" (by National Instruments), a communication system for transferring data.

quantitative EMI data: emphasizes that the referred apparent conductivity data are quantitatively correct, which is typically ensured by calibrating it to reference data, obtained for example from ERT or soil samples.

signal-to-noise ratio: the ratio between the signal amplitude and the noise level.

slow sequential signal: labeling for a special signal shape used here. The corresponding signal is a slowly switched sequence of sinusoidal signals.

super-positioned waveform: labeling for a special signal shape used here. The corresponding signal is a super-position of sinusoidal signals with multiple frequencies.

Acronyms

1D: one-dimensional

2D: two-dimensional

3D: three-dimensional

ADC: analog-to-digital converter

ATV: all-terrain vehicle

CMD: CMD-MiniExplorer (→ glossary)

DAQ: data acquisition

EIT: electrical impedance tomography

EM: electromagnetic

EM model: electromagnetic forward model (→ glossary)

EM38: EM38-MK2 (→ glossary)

EMI: electromagnetic induction

ERT: electrical resistivity tomography

GPR: ground penetrating radar

GPS: global positioning system

HCP: horizontal coplanar loops

HMD: horizontal magnetic dipole

LIN: low-induction number

LS model: local-sensitivity forward model (→ glossary)

PC: personal computer

Profiler: Profiler EMP-400 (→ glossary)

PRP: perpendicular loops

RDR: required dynamic range

Rx: receiver

SPICE: "Simulation Program with Integrated Circuit Emphasis"

SQUID: superconducting quantum interference device

STD: standard deviation

Tx: transmitter

USB: universal serial bus

VCP: vertical coplanar loops

VMD: vertical magnetic dipole

Vp: peak voltage

Symbols

* _____ **complex** / (–),
indicates the complex character of the corresponding variable.

$\Delta\sigma$ ____ **model misfit** / (–).

$\Delta\tilde{H}$ ___ **data misfit** / (–).

β _____ **induction number** / (–),
$\sqrt{\frac{\omega\mu_0\sigma}{2}}s$.

σ _____ **electrical conductivity** / (S/m),
actual specific conductivity of a soil.

σ_1 _____ **electrical conductivity of the first layer** / (S/m).

σ_2 _____ **electrical conductivity of the second layer** / (S/m).

σ_n _____ **electrical conductivity of the n-th layer** / (S/m).

σ_a _____ **apparent conductivity** / (S/m),
half-space electrical conductivity → McNeill 1980.

$\overline{\sigma_\mathrm{a}}$ _____ **mean apparent electrical conductivity** / (S/m).

$\sigma^{\mathrm{inv.}}$ ___ **inverted electrical conductivity** / (S/m).

$\sigma^{\mathrm{mod.}}$ __ **electrical conductivity of a modeled soil** / (S/m),
e.g. the chosen values for a model.

ε _____ **electrical permittivity** / (F/m = $\frac{\mathrm{A}^2\cdot\mathrm{s}^4}{\mathrm{kg}^1\cdot\mathrm{m}^3}$),
the electrical permittivity is the product of the vacuum permittivity ε_0 and the relative permittivity of a medium ε_r.

ε_0 _____ **electrical vacuum permittivity** / (F/m = $\frac{\mathrm{A}^2\cdot\mathrm{s}^4}{\mathrm{kg}^1\cdot\mathrm{m}^3}$),
$\varepsilon_0 = 8.854... \cdot 10^{-12}$ F/m.

μ _____ **magnetic permeability** / (H/m = $\frac{\mathrm{kg}\cdot\mathrm{m}}{\mathrm{A}^2\cdot\mathrm{s}^2}$),
$\mu = \mu_r\mu_0$ H/m, with μ_r being the relative magnetic permeability of a material.

μ_0 **magnetic vacuum permeability** / ($\mathrm{H/m} = \frac{\mathrm{kg \cdot m}}{\mathrm{A^2 \cdot s^2}}$),
$\mu_0 = 4\pi \cdot 10^{-7}$ H/m.

ω **angular frequency** / (rad/s),
$\omega = 2\pi f$.

φ **phase** / (rad).

φ_0 **reference phase** / (rad).

γ^* **propagation constant** / ($\mathrm{m^{-1}}$),
$\sqrt{\omega\mu_0(i\sigma_\mathrm{n} - \omega\varepsilon_0)}$.

γ^*_n **propagation constant for the n-th layer** / ($\mathrm{m^{-1}}$),
$\sqrt{\omega\mu_0(i\sigma_\mathrm{n} - \omega\varepsilon_0)}$.

ρ **specific electrical resistance** / (Ω/m).

A **coil area** / ($\mathrm{m^2}$).

A_Rx **Rx-coil area** / ($\mathrm{m^2}$).

A_Tx **Tx-coil area** / ($\mathrm{m^2}$).

B **magnetic flux** / (T).

B_noise **ambient magnetic noise level** / ($\mathrm{T}/\sqrt{\mathrm{Hz}}$).

C **capacitance** / (F).

C_Rx **receiver capacitance** / (F).

C_Tx **transmitter capacitance** / (F).

CR **cumulative response** / (–),
the cumulative response from the earth for a specific depth region and system configuration.

GCD **greatest common divisor** / (–).

H^* **magnetic field strength** / (A/m).

H^*_p **primary magnetic field strength** / (A/m).

H^*_s **secondary magnetic field strength** / (A/m).

$\tilde{H}$ **normalized magnetic field response** / (–),
$\tilde{H} = |H^*_\mathrm{s}|/|H^*_\mathrm{p}|$.

$\tilde{H}^{\text{mea.}}$ **measured magnetic field** / (A/m).

$\tilde{H}^{\text{mod.}}$ **modeled magnetic field** / (A/m).

I_{na} **input current noise of the amplifier** / ($\text{A}/\sqrt{\text{Hz}}$).

I^{*}_{Tx} **transmitter current** / (A).

J_0 **Bessel function of zeroth order** / (–).

J_1 **Bessel function of first order** / (–).

L **inductance** / (H).

L_{Rx} **receiver inductance** / (H).

L_{Tx} **transmitter inductance** / (H).

M **mutual inductance** / (–).

D **number of device configurations** / (–).

N **number of coil windings** / (–).

N_{Rx} **Rx-coil windings** / (–).

N_{Tx} **Tx-coil windings** / (–).

R **resistance** / (Ω).

RC **reflection coefficient** / (–),
reflection coefficient from the transition from one layer to the next.

R_{Rx} **receiver resistance** / ($\Omega = \frac{\text{kg}\cdot\text{m}^2}{\text{A}^2\cdot\text{s}^3}$).

R_{s} **shunt resistor** / (Ω).

R_{Tx} **transmitter resistance** / (Ω).

S **coil sensitivity** / (V/T).

T **temperature** / (K).

T_{Tx} **coil temperature of the transmitter** / (°C).

U_0 **generator voltage** / (V).

$U_{I,\,\mathrm{na}}$ **current noise voltage** / $(\mathrm{V}/\sqrt{\mathrm{Hz}})$,
the voltage that has its origin in the input current noise of the amplifier in combination with the connected impedance.

$U_{\mathrm{ind.}}$ **induced voltage** / (V).

U_{n} **voltage noise** / $(\mathrm{V}/\sqrt{\mathrm{Hz}})$.

U_{na} **input voltage noise of the amplifier** / $(\mathrm{V}/\sqrt{\mathrm{Hz}})$.

U_{nt} **thermal noise voltage** / (V).

U_p^* **complex peak voltage** / (V).

U_{Rx}^* **receiver voltage** / (V).

U_{Tx}^* **transmitter voltage** / (V).

Z^* **transfer impedance** / (Ω).

Z_0^* **reference transfer impedance** / (Ω).

Z_{Rx} **receiver coil impedance** / (Ω).

d_w **wire diameter** / (m).

f **measurement frequency** / (Hz).

h **radial coil height** / (m).

h_1 **thickness of the first layer** / (m).

h_2 **thickness of the second layer** / (m).

i **imaginary unit** / (–),
$i = \sqrt{-1}$.

k **coupling coefficient** / (–).

k_{B} **Boltzmann constant** / (J/K),
$1.3806488{\cdot}10^{-23}$ J/K.

l **coil length** / (m).

m **magnetic moment** / $(\mathrm{A}\cdot\mathrm{m}^2)$.

o **coil orientation** / (–),
orientation of the sensor coils such as, for example, HCP, VCP or PRP.

$\vec{p}$ **medium parameter** / (–),
$\vec{p} = (\sigma_1, \sigma_2, h_1)$.

r **coil radius** / (m).

s **Tx–Rx separation** / (m),
separation between a transmitter unit and the corresponding receiver unit.

t_0 **measurement time** / (s).

z **depth** / (m).

Danksagungen

Diese Dissertation habe ich am Zentralinstitut für Engineering, Elektronik und Analytik (ZEA-2), Systeme der Elektronik, in enger Zusammenarbeit mit dem Institut für Bio- und Geowissenschaften (IBG-3), Agrosphäre, des Forschungszentrums Jülich angefertigt. Aus diesem Grund möchte ich mich bei allen Kollegen aus diesen beiden Instituten bedanken, die mich bei den verschiedenen Teilarbeiten unterstützt haben.

Insbesondere danke ich meinem Betreuer, Egon Zimmermann, der wärend der Anfertigung dieser Arbeit immer für inhaltliche, technische und strategische Fragen ansprechbar und offen für meine eigenen Ansätze war, und außerdem ein sehr inspirierender und motivierender Kollege ist.

Ebenso danke ich meinem Doktorvater, Jan van der Kruk, der mich immer unterstützt hat und der seine ganze Erfahrung im wissenschaftlichen Arbeiten eingebracht hat und auch dafür gesorgt hat, dass diese Arbeit nach dem Abschluss meiner Aufgaben weitergeführt wurde.

Ich danke den Kollegen aus meiner Arbeitsgruppe am ZEA-2 für die freundliche Unterstützung und Zusammenarbeit. Insbesondere die Hilfsbereitschaft und Kompetenz von Walter Glaas, Joachim Berwix und Bernd Wolters sind in diese Arbeit eingeflossen und auch die Unterstützung der Kollegen Heinrich Meier und Yulong Zhao hat zu dem Erfolg meiner Arbeit beigetragen.

Neben den genannten Personen gibt es noch viele weitere, die mein Projekt durch ihre Unterstützung begleitet und gefördert haben. Darunter möchte ich den Institutsleiter des IBG-3, Harry Vereecken, hervornehmen, der sich auf beeindruckende Weise für die Doktoranden einsetzt und der durch Diskussionen bei regelmässigen Treffen und im Rahmen des von ihm begleiteten Doktorandenprogrammes diese Arbeit strategisch und inhaltlich begleitet und positiv beeinflusst hat. Desweiteren danke ich den Kollegen des IBG-3 und insbesondere Sebastian Rudolf, Christian von Hebel, Sebastian Busch und Daniel Altdorff, die mich durch Diskussionen und bei Feldmessungen unterstützt haben.

Außerdem danke ich Andreas Kemna von der Universität Bonn für die Anfertigung des Zweitgutachtens über diese Arbeit und Prof. Dr. Christoph Clauser von der RWTH Aachen für die Übernahme des Prüfungsvorsitzes und für seine interessante Vorlesung während meines Studiums, mit der er mein Interesse für die professionelle Geophysik geweckt hat.

Zu guter Letzt danke ich meiner Freundin Leonie und meinen Eltern Dorothee und Günther für ihre Unterstützung.

Publications (continuation)

2012 **Mester, A.**, E. Zimmermann, J. van der Kruk, W. Glaas, J. Berwix and B. Wolters, *Elektromagnetisches Leitfähigkeitsmesssystem mit verbesserter Driftkorrektur* (German), patent application, 102012008194.4

2011 **Mester, A.**, J. van der Kruk, E. Zimmermann and H. Vereecken, *Quantitative Two-Layer Conductivity Inversion of Multi-Configuration Electromagnetic Induction Measurements*, Vadose Zone Journal, 10 (4), 1319–1330, DOI: 10.2136/vzj2011.0035

2004 **Mester, A.**, *Entwicklung eines Spektralapparates zur Beobachtung und Analyse von Sternspektren* (German), VdS-Journal für Astronomie, 15, 97–99

in prep. **Mester, A.**, E. Zimmermann, C. von Hebel, J. van der Kruk, H. Vereecken and S. van Waasen, *Field-optimization and validation of a novel multi-channel electromagnetic induction system*

Conferences (selection)

05/2014 The 16th Biennial IEEE Conference on Electromagnetic Field Computation (CEFC), Annecy, France, *Model-based drift correction for an electromagnetic induction sensor using SPICE and numerical field calculation*, poster presentation

03/2014 74th Annual Meeting of the Deutsche Geophysikalische Gesellschaft (DGG), Karlsruhe, Germany, *First experience with a newly developed modular electromagnetic induction system for ground conductivity measurements*, oral presentation

03/2013 73th Annual Meeting of the Deutsche Geophysikalische Gesellschaft (DGG), Leipzig, Germany, *Verbesserung und Bewertung der Datenqualität von Elektromagnetischen Induktionsmessungen* (German), poster presentation

07/2012 The 8th IEEE International Symposium on Instrumentation and Control Technology (ISICT), London, UK, *New Electromagnetic Induction System for Soil Conductivity Measurement with Improved Drift Correction*, oral presentation

03/2012 72th Annual Meeting of the Deutsche Geophysikalische Gesellschaft (DGG), Hamburg, Germany, *Optimierung eines elektromagnetischen Induktionsmessgerätes für bodennahe und tiefenabhängige Leitfähigkeitsmessungen* (German), oral presentation

12/2011 American Geophysical Union (AGU) Fall Meeting, San Francisco, USA, *Two-layer inversion of multi-orientation, multi-offset, and multi-frequency electromagnetic induction measurements*, poster presentation

09/2011 European Association of Geoscientists & Engineers (EAGE) Near Surface 2011, Leicester, UK, *Two-layer inversion of post-calibrated multi-configuration electromagnetic induction data*, poster presentation

02/2011 71th Annual Meeting of the Deutsche Geophysikalische Gesellschaft (DGG), Köln, Germany, *Joint quantitative inversion of multi-configuration electromagnetic induction data*, oral presentation

03/2010 70th Annual Meeting of the Deutsche Geophysikalische Gesellschaft (DGG), Bochum, Germany, *Entwicklung einer Zeitbereichselektrometrie-Sonde für das "Direct Push"-Verfahren* (German), oral presenation

05/2009 International Conference on Novel Methods for Subsurface Characterization and Monitoring: From Theory to Practice, NovCare 2009, Leipzig, Germany, *Development of a 'Direct Push' TDR/TDT-Probe*, poster presentation

11/2003 Bochumer Herbsttagung (BoHeTa), Bochum, Germany, *Entwicklung eines Spektralapparates zur Beobachtung und Analyse von Sternspektren* (German), oral presentation

Awards

07/2012 **Best Presentation Award - 2nd Place**, The 8th IEEE International Symposium on Instrumentation and Control Technology (ISICT), London, UK

06/2004 **Samuel-Thomas-von-Soemmerring-Preis** for astronomical studies, *Entwicklung eines Spektralapparates zur Beobachtung und Analyse von Sternspektren* (German), Physikalischer Verein, Frankfurt a.M., Germany

Band / Volume 236
Keramische Membranen für die H_2-Abtrennung in CO-Shift-Reaktoren
D. van Holt (2014), IV, 169 pp
ISBN: 978-3-95806-007-4

Band / Volume 237
Entwicklung von porösen Silica-Membranen zur CO_2-Abtrennung aus dem Rauchgas fossil befeuerter Kraftwerke
J. S. Eiberger (2014), II, 163 pp
ISBN: 978-3-95806-008-1

Band / Volume 238
Development of a highly sensitive and versatile mass spectrometer system for laboratory and atmospheric measurements
S. Albrecht (2014), iv, 171 pp
ISBN: 978-3-95806-009-8

Band / Volume 239
High Temperature Corrosion of Alloys and Coatings in Gas-Turbines Fired with Hydrogen-Rich Syngas Fuels
W. Nowak (2014), 201 pp
ISBN: 978-3-95806-012-8

Band / Volume 240
Einfluss neuer Membranmaterialien auf Herstellung und Betrieb von Direktmethanol-Brennstoffzellen
S. Hürter (2014), V, 164 pp
ISBN: 978-3-95806-013-5

Band / Volume 241
Spannungsinduziertes Versagen in Hochtemperaturschichtsystemen
C. Nordhorn (2014), v, 118 pp
ISBN: 978-3-95806-016-6

Band / Volume 242
Änderungsdetektion digitaler Fernerkundungsdaten mittels objekt-basierter Bildanalyse
C. Listner (2014), 176 pp
ISBN: 978-3-95806-017-3

Band / Volume 243
Räumlich hoch aufgelöste Modellierung des Spaltproduktverhaltens in einem HTR-Core mit kugelförmigen oder prismatischen Brennelementen
A. Xhonneux (2014), viii, 239 pp
ISBN: 978-3-95806-020-3

Band / Volume 244
Effects of Cercospora leaf spot disease on sugar beet genotypes with contrasting disease susceptibility
S. Schmittgen (2015), 121 pp
ISBN: 978-3-95806-021-0

Band / Volume 245
Light scattering and trapping in thin film silicon solar cells with an n-i-p configuration
W. Böttler (2015), 132 pp
ISBN: 978-3-95806-023-4

Band / Volume 246
Nanostructured Si-alloys for silicon solar cells
K. Ding (2015), 210 pp
ISBN: 978-3-95806-024-1

Band / Volume 247
Electrochemical Texturing and Deposition of Transparent Conductive Oxide Layers for the Application in Silicon Thin-Film Solar Cells
J.-P. Becker (2015), ix, 156, XXIV pp
ISBN: 978-3-95806-027-2

Band / Volume 248
Stoffliche Charakterisierung radioaktiver Abfallprodukte durch ein Multi-Element-Analyseverfahren basierend auf der instrumentellen Neutronen-Aktivierungs-Analyse – MEDINA –
A. W. Havenith (2015), 311 pp
ISBN: 978-3-95806-033-3

Band / Volume 249
Quantitative Two-Layer Inversion and Customizable Sensor-Array Instrument for Electromagnetic Induction based Soil Conductivity Estimation
A. Mester (2015), viii, 119 pp
ISBN: 978-3-95806-035-7

Energie & Umwelt /
Energy & Environment
Band / Volume 249
ISBN 978-3-95806-035-7